Current Topics in
Environmental Health and Preventive Medicine

Hiroki Takada
Kiyoko Yokoyama *Editors*

Bio-information for Hygiene

Springer

Current Topics in Environmental Health and Preventive Medicine

Series Editor

Hidekuni Inadera
Department of Public Health
University of Toyama
Toyama, Japan

Current Topics in Environmental Health and Preventive Medicine, published in partnership with the Japanese Society of Hygiene, is designed to deliver well written volumes authored by experts from around the globe, covering the prevention and environmental health related to medical, biological, molecular biological, genetic, physical, psychosocial, chemical, and other environmental factors. The series will be a valuable resource to both new and established researchers, as well as students who are seeking comprehensive information on environmental health and health promotion.

More information about this series at http://www.springer.com/series/13556

Hiroki Takada • Kiyoko Yokoyama
Editors

Bio-information for Hygiene

Springer

Editors
Hiroki Takada
Graduate School of Engineering
University of Fukui
Bunkyo
Fukui
Japan

Kiyoko Yokoyama
Graduate School of Design and Architecture
Nagoya City University
Nagoya
Aichi
Japan

ISSN 2364-8333 ISSN 2364-8341 (electronic)
Current Topics in Environmental Health and Preventive Medicine
ISBN 978-981-15-2159-1 ISBN 978-981-15-2160-7 (eBook)
https://doi.org/10.1007/978-981-15-2160-7

This Springer imprint is published by the registered company Springer Nature Singapore Pte Ltd.
The registered company address is: 152 Beach Road, #21-01/04 Gateway East, Singapore 189721, Singapore

Preface

Hygiene has two important components: preventive medicine and environmental medicine. From the viewpoint of preventive medicine, it is important to prevent and diagnose any undiagnosed disease or abnormality in its initial stage, based on scientific evidence such as the bio-signals measured by a wearable device in daily life. According to one theory, sleep debt is a cause of many complaints. Brain science, as detailed in Chaps. 1 and 6, has received much attention in recent years due to its development in understanding the human control system and human beings themselves. In addition, mindfulness meditation is now attractive as a countermeasure to many complaints, including mental instability and diseases. Mental health is an untapped field, as discussed in the last chapter. Brain science and associated bio-signals might be useful tools in developing the field. This book clarifies that meditation is not similar to sleep.

In both components of the hygiene mentioned above, research has been based on the data associated with body activity, including the endocrine system (Chap. 2) and electro-activity in humans. For instance, it is important to evaluate the autonomic nervous system (Chaps. 3 and 4) to elucidate general malaise, motion sickness during transportation, and space medicine (Chaps. 5 and 9). Electrophysiology is an important part of this field. In addition, bio-information is one of the targets in several research fields that have developed rapidly in recent years; it is expected that the bio-signals will be widely used in the future. Bio-signals can be measured by mobile and universal devices, especially in the welfare/nursing care of the elderly and patients (Chaps. 6, 7, 8). Above all, aging population is increasing, mainly in developed countries. Therefore, it is useful for us to use the bio-signals to extend the healthy life span with reduced disease burden.

This book provides an outline of the principle and display methods of virtual reality (VR) and the biological effects of advanced technology such as VR, augmented reality (AR), mixed reality (MR), and robotics (Chaps. 5, 9, 11). In addition, the realization of high image quality 4K/8K broadcasts is underway, led mainly by the Ministry of Internal Affairs and Communications and broadcasters. In addition, the progression of TV to high image quality will facilitate the sale of high-definition glassless 3D TV, which has been a venture whose market share and growth has not

been tremendous; however, further development may increase the opportunities for stereoscopic viewing in various fields, not limited to amusement and medical use. Therefore, there is an urgent need to clarify the problems related to stereoscopic viewing of the human body and reduce them as an important health topic. This progress can be applied to assist rehabilitation in clinical care to some degree (Chap. 11). This book also introduces technology/innovation for preventive medicine and medical care.

By measuring and analyzing the biological signals over a long duration, the diagnostic accuracy can be dramatically improved, and the medical effects of the treatment can be enhanced. In Chaps. 4 and 12, we describe their clinical significance in addition to the future prospects of these technologies and artificial intelligence. This will be required in telemedicine on isolated islands. In addition, we should stress on how to make good use of bio-information in the field of hygiene. Moreover, one can apply this information for economical pursuits as well as providing healthcare service or even a combination of both. In addition, this book is designed for data scientists and/or researchers of big data on bio-signals.

Contents in this book can be applied not only to the field of care and welfare but also to various fields such as robot operation interface and emotion analysis using biological signals. Creators and technical staff working in the field of data science/data-based science are interested in this project. They are good at collecting data involved in body activities, including electrical activity in the human body, human behavior (Chap. 10), and other bio-information; however, no one seems to have figured out a method to apply these data practically for application in human services. It is important to have a hygienic viewpoint. In addition, these are valuable resources for both new and established researchers as well as students seeking comprehensive information on environmental/occupational health and health promotion.

Mar/3/2021
Bunkyo, Japan Hiroki Takada

Contents

Chapter 1
Brain Measures

Masumi Takada, Hiroki Takada, and Akihiro Sugiura

Abstract In this chapter, we refer to three contents under the theme of brain measures. The first outlines the anatomical and functional characteristics of the brain, and some past studies on the elucidation of information process mechanisms in the brain are shown. The second explains each principle and introduces each major measurement method based on the classification of the configuration and the function measurements. The configuration measures present computed tomography and magnetic resonance imaging (MRI), and the function measurements are positron emission tomography, functional MRI, and functional near-infrared spectroscopy (fNIRS). Finally, one of our actual studies on function measurements by fNIRS while playing a video game with a handheld game console with a two-dimensional (2D)/three-dimensional (3D) display as an example of fNIRS study is presented. A total of eight subjects sat on a chair and played the game. They first played TETRiS® for 60 s using the 2D display and continued the game for 60 s using the 3D display. The display was then returned to 2D, and the game was continued for 30 s. Regarding this as one set, fNIRS was measured while they continuously played five sets. Changes in oxyhemoglobin values over the three periods in the above five trials were recorded at 12 channels on the frontal, occipital, and bilateral temporal lobes at 7.7 Hz. Therefore, we concluded that sensory areas, such as the visual area, may have been activated when playing the game with 3D display compared to activation by 2D.

Keywords Brain · Configuration · Function · Neurovascular coupling
Video game

M. Takada
School of Nursing, Yokkaichi Nursing and Medical Care University, Yokkaichi, Mie, Japan

H. Takada
Graduate School of Engineering, University of Fukui, Fukui, Japan

A. Sugiura (✉)
Department of Radiological Technology, Gifu University of Medical Science, Seki, Gifu, Japan
e-mail: asugiura@u-gifu-ms.ac.jp

H. Takada, K. Yokoyama (eds.), *Bio-information for Hygiene*, Current Topics in Environmental Health and Preventive Medicine,
https://doi.org/10.1007/978-981-15-2160-7_1

1.1 Introduction

The brain is an essential organ for mental function, and along with the medulla oblongata constitutes the central nervous system. These have information processing for the mind and physical body. For example, the brain inputs information from the five senses. Following this, it analyzes, memorizes, thinks, and orders the body as output from the input information. The structure of the brain can be anatomically separated into four parts: the cerebrum, diencephalon, cerebellum, and brainstem. Although each part handles different functions, processing is performed systematically in cooperation.

For the details of each part, the brainstem directly controls vital autonomic functions, such as respiration, circulation, and adjustment of sleep and awareness. The occurrence of irreparable damage in the brainstem is one of the criteria for judging brain death [1]. The cerebellum assumes balance function, postural control, adjustment of blood pressure and circulation, controlling voluntary movement, and movement cognition. Damage to the cerebellum evokes functional abnormalities in motility and balance control. It thus causes difficulty in gait and postural maintenance. The diencephalon includes the hypothalamus and the thalamus. The hypothalamus functions as the center of the automatic nerve and endocrine system maintaining homeostasis through the automatic nerve and sensory information from the whole body. In addition, there are also centers of appetite, aphrodisia, aching pain, and thirst in the hypothalamus. The thalamus is the transfer point of the sensory nerve between the cerebral cortex and periphery. All nerves except for the olfactory sense run to the cerebral cortex through the thalamus. The cerebrum is separated into the cerebral cortex and the limbic cortex. The cerebral cortex handles high intelligence function and autokinesis: esthesia, memorization, intellection, language, judgment, and recognition. The limbic cortex is a classical function common to animals, such as life maintenance, affect, and instinct. The brain consists of many areas separated according to differences in cell configuration. In addition, a unique function is located in each area, and this basic concept between function and anatomic locations of the brain is known as the functional localization [2, 3]. Previous studies on finding brain functions in medicine, physiology, and psychology have been based on functional localization. Therefore, to elucidate information process mechanisms in the brain, verifying the relationship between injured area and loss of function [4, 5], and measuring the brain activity under task load conditions [6–8], or under external or internal stimuli have been performed. In addition, during an awake craniotomy, the surgeons located the motor and speech regions by electric stimulation or real communication before tumor removal, to avoid these sensitive areas with high accuracy during surgery [9].

1.2 Types of Brain Measures and Their Principles

The brain measures are divided into two groups: configuration and function measurement. Table 1.1 shows the characteristics of the brain measures. The details of the method for measurement are presented in the next section. Chapter 6 describes the details of an electroencephalogram (EEG).

1.2.1 Configuration Measurements

The typical techniques for configuration measurements include computed tomography (CT) and magnetic resonance imaging (MRI). The characteristics of these techniques are simultaneously measuring both head shape and changes in the condition of the cerebral tissue. An X-ray CT scanner, which has an X-ray tube (source) and an X-ray detector across a subject (head), measures the X-ray attenuation in each degree of the CT detector (projection angle) during rotation of the CT scanner. Further, the measured attenuation information is processed by a computer to obtain a CT image constituting the X-ray absorption value in each pixel. Figure 1.1 shows an example of a clinical CT image. This image has characteristic findings of subarachnoid hemorrhage; this image shows a high-density area, following cisterna, due to hemorrhage. Subarachnoid hemorrhage is a dangerous disorder because of severe symptoms, such as sensation disturbance and higher brain dysfunction, due to a rapid increase in intracranial pressure.

Table 1.1 List of brain measurer type

Type	Technique	Source	Method	Area	Invasiveness
Configuration	X-ray CT	X-rays	Active	Whole	+ (radiation)
	MRI	NMR signal	Active	Whole	–
Function	EEG/MEG	Action potential/ magnetic field	Passive	Superficial	–
	Nuclear medicine (PET, SPECT)	Radioisotope	Active	Whole	+ (radiation)
	Functional-MRI	BOLD signal (NMR signal)	Active	Whole	–
	Functional-NIRS	NIR light	Active	Superficial	–

CT Computed tomography, *MRI* Magnetic resonance imaging, *EEG* Electroencephalogram, *MEG* Magnetoencephalography, *PET* Positron emission tomography, *SPECT* Single-photon emission tomography, *NIRS* Near-infrared spectroscopy, *NMR* Nuclear magnetic resonance, *BOLD* Blood oxygen level dependent, *NIR* Near-infrared

Fig. 1.1 Example of a CT image (subarachnoid hemorrhage). This image shows high-density area following cisterna

MRI makes images of water molecules in the body by applying nuclear magnetic resonance (NMR). For more details on the principle of MRI, the molecule in the static magnetic field induces NMR by exposure to electromagnetic rays with a specific frequency. NMR is in the excited state; further, during returning to the ground state, the molecule radiates electromagnetic rays as signals, which are utilized in MRI. MRI can obtain various contrast types of images according to the scan method because the type of signals changes with the scan method. Comparing CT with MRI, MRI has higher configuration detectability than CT (especially changes in the tissues). In contrast, although CT scan indicates a high radiation dose, there are some advantages, such as short study time and high readiness crises. Moreover, a CT scan can obtain images that have clear findings of the hemorrhage from the early stage, compared with MRI. Hence, the best test is currently available according to the advantage of each equipment to avail diagnostic imaging.

1.2.2 Function Measurements

As for the function measurements, there are some measurement methods attributed to differences in the principle of measurement based on physiology. An EEG and magnetoencephalography (MEG) are aimed at the activity of nerve cells (neurons and synapses). In EEG, some electrodes are set at regular intervals on the scalp, and the integrated action potential of nerve cells grouped by each brain function just

below the electrode is recorded (see more detail in Chap. 6). In contrast, unlike the EEG measurement method, the MEG can detect both the intensity and precise position of the neural activity by small changes in the magnetic field with electric current (potential) with the neural activity from many detectors set around the head because the magnetic field does not reduce or distort by the skull or skin.

Evaluation of brain function by cerebral blood circulation is premised on the establishment of neurovascular coupling [10, 11], representing a direct relationship between neural activity and local blood flow. When the brain cells become active, local blood flow increases depending on the degree of activity. For more information, the neural cells have to use adenosine triphosphate (ATP), which manages bioenergy during electrical activity. To produce ATP, oxygen and glucose are required. However, neural cells do not store both and receive both through the blood flow. In this way, by measuring changes in local blood flow, we can archive the localization of neural activity. The three typical measurement techniques based on neurovascular coupling are shown below.

The first is nuclear medicine, in particular, positron emission tomography (PET) and single-photon emission computed tomography (SPECT). PET can create images of local blood volume, oxygen metabolism, glycometabolism, and distribution of neural receptors by using radioactive tracer (medicine) labeled by positron-emitting radionuclides that decay and release the positron (β^+-ray). This positron emits two gamma rays in opposite directions because the positron collides with the surrounding electrons. Because the annihilation gamma-ray goes straight, coincidence detection of the annihilation gamma rays can correctly determine the annihilation position of the positron in the body. Finally, determining the annihilation position from all directions, such as X-ray CT, can obtain tomographic images. In contrast, SPECT obtains tomographic images by using tracer-labeled γ-ray emitting radionuclides, such as ^{99m}Tc and ^{123}I. SPECT is weaker in quantitativeness than PET. However, SPECT is easier to access to radioisotopes as an advantage.

The second is functional MRI (fMRI), which utilizes redox reactions of hemoglobin (Hb). As mentioned above, much activity of the neural cells require much oxygen. Hb combines oxygen in the lung and changes into oxygenated Hb (oxy-Hb). Transporting oxygen to the tissue, oxy-Hb changes into deoxygenated Hb (deoxy-Hb) due to the reduction reaction. One of the features of deoxy-Hb (paramagnet) is the ease of magnetization, comparable to oxy-Hb (negligible diamagnet). The NMR signal of deoxy-Hb is different from that of oxy-Hb in short-time imaging. Hence, local brain activity decreases the local magnetic field according to the decrease in deoxy-Hb concentration in the local brain blood capillary because of an increase in the local oxy-Hb concentration. This phenomenon is called the blood oxygenation level-dependent effect [12, 13], which is utilized in fMRI. Figure 1.2 shows local brain activity images under the motion task as an example of an experimental fMRI study. These images represent brain activity while the subject did left finger tapping continuously. The activation of the motor area is shown in Fig. 1.2.

The third is functional-near-infrared spectroscopy (fNILS), measuring the relative amount of local blood through the use of absorption of near-infrared light by Hb. fNIRS can measure changes in blood volume (local neural activity) at 2–3 cm

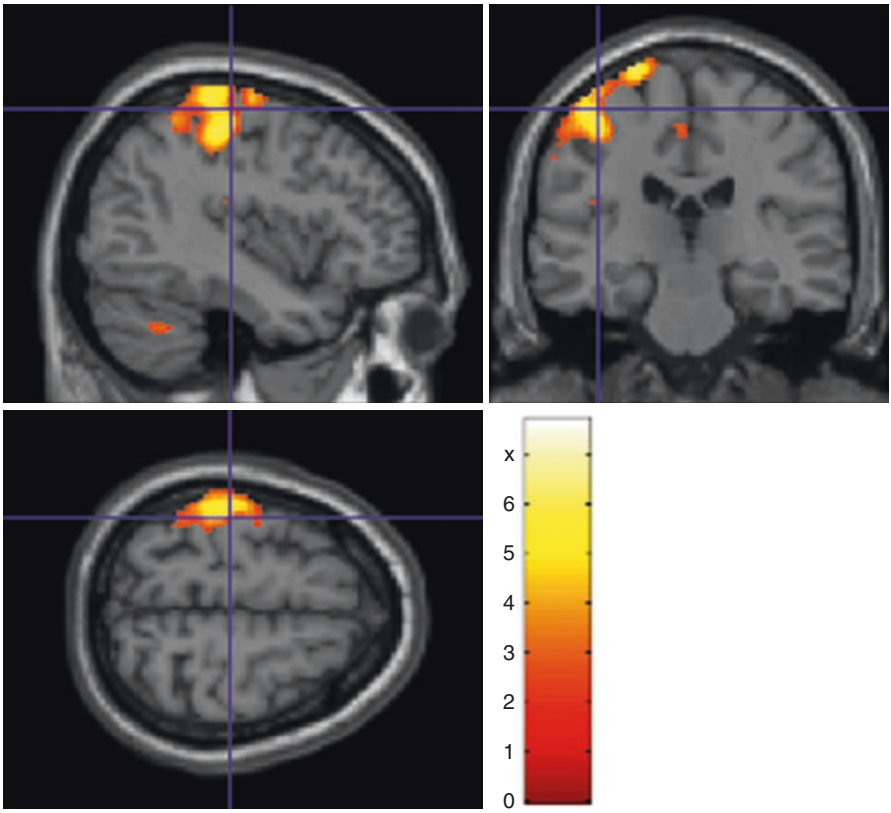

Fig. 1.2 Local brain activity images while a subject did left finger tapping continuously

below the head surface where it positions the cerebral cortex. The near-infrared ray at 700–1000 nm utilized in fNIRS indicates permeability for body tissue, such as bone and skin. In contrast, they are specifically absorbed by Hb. Each oxy-Hb, deoxy-Hb, and total Hb concentration is obtained by applying a difference in Hb absorbance index related to oxygenation state and wavelength of near-infrared light. This is done according to the continuous wave method [14], in which the amount of attenuation is calculated from the incident and detection light for two or more different wavelengths. Actual measurement values obtained from the fNIRS equipment do not reflect the absolute values of Hb concentration because the measurement values are expressed as a product of Hb concentration and light path. However, by equalizing all the distances from the light-receiving probe to the light-transmitting probe, each relative Hb concentration value is attainable because it can be assumed that light passes across a constant distance. fNIRS measurements are acquired by positioning the photo-transmitter probe and the photo-receiver probe on the scalp at regular intervals. Near-infrared light irradiated from the photo-transmitter is

scattered and reflected in the cerebral cortex and then detected from the photoreceiver probe at a constant distance.

1.3 Actual Case of Functional Measurement

This section shows one of our studies on the evaluation of local brain function by using fNIRS while playing a video game with a handheld game console that has a two-dimensional (2D)/three-dimensional (3D) switchable display.

1.3.1 Background

The number of elderly people with dementia in Japan is estimated to reach approximately 7 million by 2025, indicating that a fifth of those aged 65 years and more would have dementia. Dementia is now a disease that is close to home affecting anyone. Based on the comprehensive strategy to accelerate dementia measures, the Health, Labor, and Welfare Ministry of Japan (called the New Orange Plan) aimed toward friendly community planning for the elderly with dementia, enabling people to live a life the way they want to until the end by prevention; thus, early diagnosis of/response to dementia is required.

Although daily life activities, such as having meals, exercising, pursuing hobbies, and relationships with others, are effective for the prevention of dementia, brain activity training is particularly gaining attention. Additionally, in the USA, regarding the relationship between vision and cognitive decline, such as Alzheimer's disease, it was revealed that those who have better vision have a 63% lower risk of dementia [15]. Visuospatial disorder is relatively common in Alzheimer's dementia, and a strong relationship exists between cognition disorder and decreased vision performance. Until now, researchers have shown that vision performance training using virtual reality information media content could increase the tension and relaxation effect of the ciliary muscle group [16, 17]. Inhibition and alleviation of decreased vision in aged adults is expected to be a strategy for the prevention of dementia. Furthermore, to prevent dementia, various establishments have put forth efforts to encourage exercise and the pursuit of hobbies. However, there are only a few reports on dementia prevention training using brain training. This might be due to the fact that exercises can be evaluated by an objective indicator, whereas brain training only with a special device used to measure brain activity.

In this study, we report the changes in brain activity when study subjects played a game related to vision and short-term memory involving 3D images.

1.3.2 Methods and Task Design

The subjects were eight healthy young persons (22.8 ± 0.9 years [mean ± standard]) with no past medical history of diseases of the ear or nervous system. The experiment was sufficiently explained to the subjects and prior written consent was obtained.

For fNIRS, a FOIRE-3000 (SHIMADZU, Kyoto) was used. Channels were arranged as follows: 1–12 ch on the frontal lobe, 13–24 ch on the left temporal lobe, 25–36 ch on the right temporal lobe, and 37–48 ch on the occipital lobe (Fig. 1.3). The probe caps to fix the channels were set to the bilateral preauricular points, plane α covering the nasion (the root of the nose) and plane β parallel to the plane α. The distance between planes α and β was 3 cm, and plane β was vertically upward of plane α. The occipital lobe was fixed so as to set the center of the probe cap to the inion in the occipital region (external occipital protuberance).

For the 3D handheld game console, NINTENDO 3DS (Nintendo, Kyoto) was used. NINTENDO 3DS adopted the parallax barrier method, and the liquid crystal display was 3.53-inch (76.8 mm width × 46.08 mm length). For the game software, TETRiS® (BANDAI NAMCO GAMES, Tokyo), which is relatively simple to operate, was selected from general games.

The subjects sat on a chair and played the game in a comfortable position. They first played TETRiS® for 60 s using the 2D display (early 2D) and continued the game for 60 s using the 3D display (3D). The display was then returned to 2D, and the game was continued for 30 s (late 2D). Regarding this procedure as one set, fNIRS was measured while they continuously played five sets. Changes in oxy-Hb values over the early 2D, 3D, and late 2D periods in the above five trials were recorded at 12 channels on the frontal, occipital, and bilateral temporal lobes at 7.7 Hz. The oxy-Hb value on fNIRS was compared between early 2D and 3D and

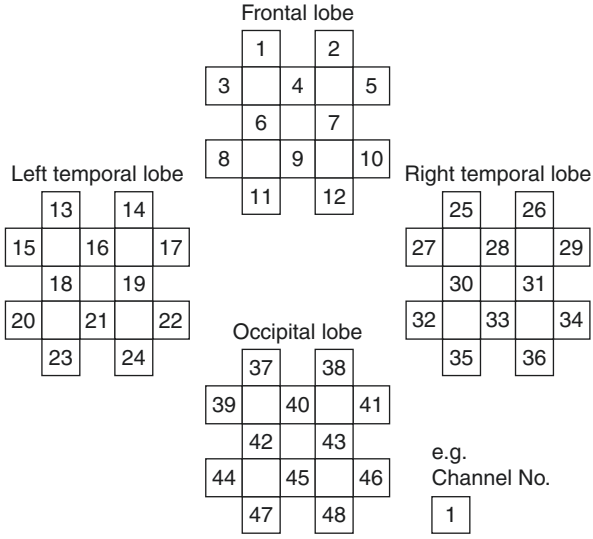

Fig. 1.3 Channel arrangement

between 3D and late 2D (doubled because of 30 s recording time) using the Wilcoxon signed-rank sum test setting the significance level at $p < 0.05$.

1.3.3 Results and Discussion

The value at each channel was compared between early 2D and 3D and between 3D and late 2D using the Wilcoxon signed-rank sum test. Channels at which significant changes were observed were recorded.

Figure 1.4 shows the results of the statistical test comparing early 2D and 3D. On comparison, in the frontal lobe, the 3D integrated value was significantly greater in early 2D at ch7 and ch12, while in the left temporal lobe, it was significantly greater at ch13, ch18–ch21, and ch24. In the right temporal lobe, the integrated value was significantly greater in 3D at ch27, while in the occipital lobe, it was significantly greater at ch42–ch44. Figure 1.5 shows the results of the statistical test comparing 3D and late 2D. On comparison, the integrated value was significantly greater in late 2D at ch2, ch5, ch7, ch8, and ch10 in the frontal lobe. In the left and right temporal lobes, the integrated value was significantly greater in late 2D at ch13 and ch27. However, no significant difference was noted in the occipital lobe.

An increase in local cerebral blood flow from early 2D to 3D and from 3D to late 2D was noted (values at ch3 were not presented due to measurement failure). Local cerebral blood flow increased from early 2D to 3D in many channels. The increase in the local cerebral blood flow from 3D to late 2D was greater than that from early 2D to 3D; however, a sharp reduction in the local brain blood flow was also observed in several channels.

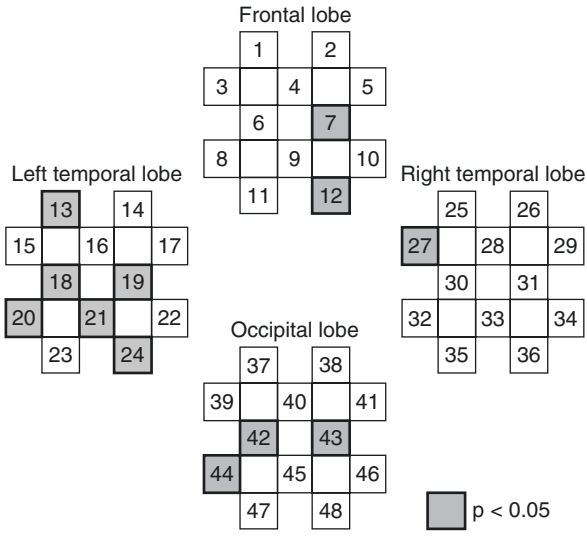

Fig. 1.4 Channels at which significant changes were observed between early 2D and 3D

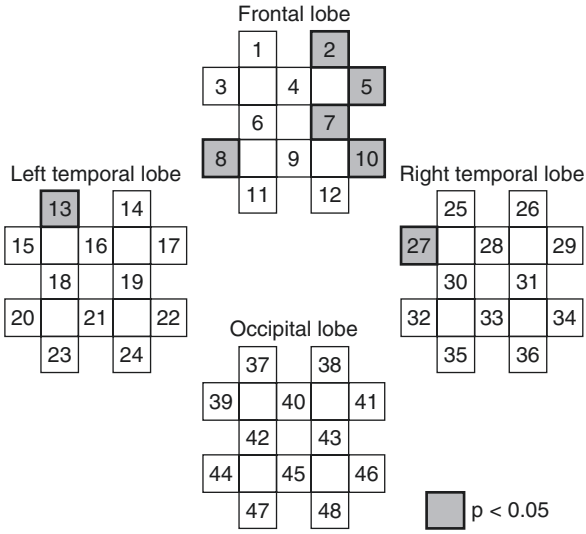

Fig. 1.5 Channels at which significant changes were observed between 3D and late 2D

A marked increase in local brain blood flow was noted in the frontal, occipital, and left temporal lobes. In the frontal lobe, brain blood flow consistently increased from early 2D to late 2D in many channels. Because the frontal lobe controls psychogenesis, such as emotion, attention, thinking, and voluntary movement, brain blood flow may have continued to increase due to thinking and concentration on the game operation. In the occipital and left temporal lobes, the brain blood flow increased from early 2D to 3D, and no significant difference was noted between 3D and late 2D. Various sensory areas are present in the left temporal lobe. In contrast to the right temporal lobe, which memorizes sounds and shapes, the left temporal lobe memorizes and understands speech [18, 19]. Because TETRiS® is a game that requires thinking, 3D images may have a large influence on the left temporal lobe.

Changes in brain blood flow while playing the game were compared between playing using the 2D and 3D displays by measuring fNIRS. Because the visual area responsible for vision is located in the occipital lobe [18, 19], it may have been strongly influenced when 2D was switched to 3D. In conclusion, the visual area responsible for vision is present in the occipital lobe, and various sensory areas are present in the left temporal lobe. Thus, sensory areas, such as the visual area, may have been activated when playing the game with 3D images compared to the activation by 2D.

1.4 Conclusion

This chapter treated three contents under the theme of brain measures. First, we outlined the anatomical and functional characteristics of the brain. Second, each principle was explained and each major measurement method was introduced based

on the distinction between the configuration and the function measurements. Finally, one of our actual studies on function measurement by fNIRS while playing a video game with a handheld game console having a 3D display as an example of fNIRS studies. The brain measurement technology has been advancing to determine brain function by the particular application in the medical field.

References

1. Machado C. Diagnosis of brain death. Neurol Int. 2010;2:e2. https://doi.org/10.4081/ni.2010.e2.
2. Folzenlogen Z, Ormond DR. A brief history of cortical functional localization and its relevance to neurosurgery. Neurosurg Focus. 2019;47:E2. https://doi.org/10.3171/2019.6.FOCUS19326.
3. Jacobson S, Marcus EM. Cerebral cortex functional localization. In: Neuroanatomy for the neuroscientist. Boston: Springer US; 2008. p. 189–217. https://doi.org/10.1007/978-0-387-70,971-0_8.
4. Milner AD. How do the two visual streams interact with each other? Exp Brain Res. 2017;235:1297–308. https://doi.org/10.1007/s00221-017-4917-4.
5. Catani M, Jones DK, Ffytche DH. Perisylvian language networks of the human brain. Ann Neurol. 2005;57:8–16. https://doi.org/10.1002/ana.20319.
6. Sato H, Yahata N, Funane T, Takizawa R, Katura T, Atsumori H, et al. A NIRS-fMRI investigation of prefrontal cortex activity during a working memory task. NeuroImage. 2013;83:158–73. https://doi.org/10.1016/j.neuroimage.2013.06.043.
7. Fischer E, Bülthoff HH, Logothetis NK, Bartels A. Visual motion responses in the posterior cingulate sulcus: a comparison to V5/MT and MST. Cereb Cortex. 2012;22:865–76. https://doi.org/10.1093/cercor/bhr154.
8. Aghajani H, Garbey M, Omurtag A. Measuring mental workload with EEG + fNIRS. Front Hum Neurosci. 2017;11:359. https://doi.org/10.3389/fnhum.2017.00359.
9. Hervey-Jumper SL, Li J, Lau D, Molinaro AM, Perry DW, Meng L, et al. Awake craniotomy to maximize glioma resection: methods and technical nuances over a 27-year period. J Neurosurg. 2015;123:325–39. https://doi.org/10.3171/2014.10.JNS141520.
10. Haydon PG, Carmignoto G. Astrocyte control of synaptic transmission and neurovascular coupling. Physiol Rev. 2006;86:1009–31. https://doi.org/10.1152/physrev.00049.2005.
11. Buxton RB, Uludağ K, Dubowitz DJ, Liu TT, Uludağ K, Dubowitz DJ, et al. Modeling the hemodynamic response to brain activation. NeuroImage. 2004;23(Suppl 1):S220–33. https://doi.org/10.1016/j.neuroimage.2004.07.013.
12. Ogawa S, Lee TM, Nayak AS, Glynn P. Oxygenation-sensitive contrast in magnetic resonance image of rodent brain at high magnetic fields. Magn Reson Med. 1990;14:68–78. https://doi.org/10.1002/mrm.1910140108.
13. Ogawa S, Lee TM, Kay AR, Tank DW. Brain magnetic resonance imaging with contrast dependent on blood oxygenation. Proc Natl Acad Sci U S A. 1990;87:9868–72. https://doi.org/10.1073/pnas.87.24.9868.
14. Scholkmann F, Kleiser S, Metz AJ, Zimmermann R, Mata Pavia J, Wolf U, et al. A review on continuous wave functional near-infrared spectroscopy and imaging instrumentation and methodology. Neuroimage. 2014;85(Pt 1):6–27. https://doi.org/10.1016/j.neuroimage.2013.05.004.
15. Rogers MAM, Langa KM. Untreated poor vision: a contributing factor to late-life dementia. Am J Epidemiol. 2010;171:728–35. https://doi.org/10.1093/aje/kwp453.
16. Sugiura A, Miyao M, Yamamoto T, Takada H. Effect of strategic accommodation training by wide stereoscopic movie presentation on myopic young people of visual acuity and asthenopia. Displays. 2011;32:219–24. https://doi.org/10.1016/j.displa.2011.04.001.

17. Takada M, Miyao M, Sato M, Yoshikawa K, Matsuura Y, Takada H. Effect of accommodation training on visual function of visual inspection workers and middle-aged people. J Sports Med Doping Stud. 2012;02:2–5. https://doi.org/10.4172/2161-0673.1000112.
18. Sugihara I. Audition and equilibrium. In: Sakai T, Kawahara K, editors. Normal structure and function of human body, Nervous system 2, vol. 9. Tokyo: Nihon-Ijishinpo; 2005. p. 66–77.
19. Netter FH. Netter atlas of human anatomy. 6th ed. Philadelphia: Saunders Elsevier; 2014.

Chapter 2
Endocrine System

Dominika Kanikowska

Abstract This chapter describes the essential principles of endocrinology—simplified and explained. The section provides the organisation of the endocrine system, as well the general concept of hormone production and a brief description of the hormone function. The information presented is also meant to understand the physiological mechanism involved in the endocrine regulation of organ function. Understanding the mechanism underlying normal endocrine physiology is essential to understand the pathophysiology—transition from health to disease.

Keywords Endocrine system · Hormone · Biological rhythms · Hypothalamus Pituitary gland · Adrenal gland · Thyroid gland · Parathyroid gland · Pancreas

2.1 General Information

Homeostasis is a dynamic process by which an organism maintains and controls its internal environment. The endocrine system regulates the homeostasis of the body using *hormones*, i.e. chemical mediators released into the blood by specialised organs, the so-called endocrine *glands*.

The effect of the hormone is elicited depending on where it was released:

1. Endocrine (biologic effect on target cells in distant organs)
2. Paracrine (biologic effect on target cells in neighbouring organ/tissue)
3. Autocrine (biologic effect on the same cell that releases it)
4. Intracrine (intracellular biologic effect on the same cell that releases it)

The figures and tables are my own ones.

D. Kanikowska (✉)
Department of Pathophysiology, Poznań University of Medical Sciences, Poznań, Poland
e-mail: dkanikowska@ump.edu.pl

H. Takada, K. Yokoyama (eds.), *Bio-information for Hygiene*, Current Topics in Environmental Health and Preventive Medicine,
https://doi.org/10.1007/978-981-15-2160-7_2

Based on their *chemical structure*, hormones can be classified into: protein or peptide (e.g. insulin), steroid (e.g. cortisol) and amino-acid derived (e.g. epinephrine).

Hormones act selectively on those tissues and organs that express *hormone-specific receptors*. Based on their *cellular localisation*, hormone-specific receptors can be classified into:

1. Cell membrane (binding of, i.e. protein or peptide hormones, catecholamines)
2. Intracellular (binding of, i.e. steroid hormones, steroid derivative vitamin D_3, thyroid hormones)

Based on their *mechanism of action*, hormones can be classified into: trophic (hormones that affect the secretion of other endocrine glands) and non-trophic (hormones that are secreted by endocrine glands) (Fig. 2.1).

The principle of *negative feedback* is crucial both for the functioning of the endocrine system and for the diagnosis of endocrine disorders. According to this principle, trophic hormones stimulate the secretion of non-trophic hormones, and these also suppress the secretion of trophic hormones. This allows for maintaining the optimal concentration of specific hormones in the blood. Three levels of feedback can be recognised: long, short and ultrashort loops.

Hormonal homeostasis exhibits *periodic fluctuations*. Several hormones were shown to have *pulsatory oscillations* (i.e. gonadotropin hormones, growth hormone), daily oscillations (i.e. melatonin, cortisol) (Fig. 2.2) or even seasonal rhythms (i.e. melatonin, cortisol).

Diseases of the endocrine system resulting from the alteration in the circulating level of hormones are classified as either (1) overproduction (hyperfunction) or (2) undersecretion (hypofunction).

Hyperfunction is associated usually with:

1. Dysfunction of the endocrine gland (primary hyperfunction)
2. Stimulation of a target endocrine organ by excessive trophic hormone synthesis and secretion (secondary hyperfunction)

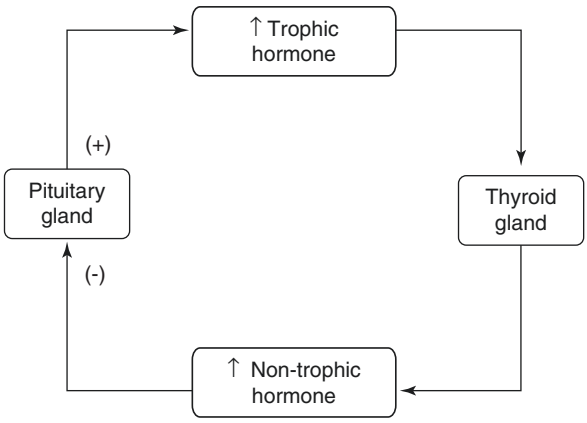

Fig. 2.1 Hormonal control of hormone release. Hormone synthesises by pituitary gland induce production of hormone from thyroid gland. Non-thropic hormone inhibits synthesis of thropic hormone

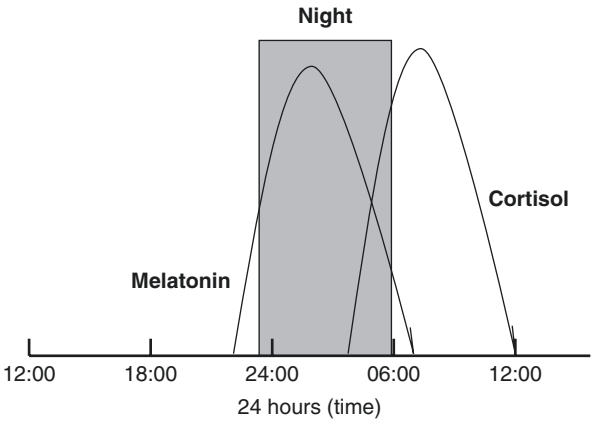

Fig. 2.2 Circadian rhythm of cortisol and melatonin

3. Endocrine hyperactivity secondary to disease of other organs (e.g. hypersecretion of humoral "hormone-like" factors by non-endocrine tumours)

Hypofunction is associated usually with:

1. Lesion of the endocrine gland (primary hypofunction)
2. A decrease in a trophic stimulus of hormone production in a target endocrine gland (secondary hypofunction)
3. Endocrine dysfunction resulting from the failure of receptor response, so that despite the presence of the hormone in the correct concentration, the target organ is unable to respond to its action

To known whether the hormonal disorder is primary or secondary, the level of the target, non-trophic hormone and the concentration of the appropriate tropic hormone should be evaluated.

Increased trophic hormone levels with low non-trophic hormone levels indicate *primary hyperfunction*, mainly due to the failure of a gland (e.g. hypertrophy or tumour), which causes an increase in the amount of trophic hormone and a decrease in the secretion of the target hormone. Increased trophic hormone levels with increased target gland hormone levels indicate *secondary hyperfunction* (autonomous secretion of trophic hormone or inability of target gland hormone to suppress trophic hormone release). Increased trophic hormone levels with low target hormone levels indicate primary failure of the target endocrine organ (*primary hypofunction*) (e.g. due to inflammation, autoantibody). The secretion of the tropic hormone is elevated but does not cause the expected increase in a non-trophic hormone. Low trophic hormone levels with low non-trophic hormone (target gland hormone) levels indicate a trophic hormone deficiency (*secondary hypofunction*), as seen with pituitary failure (e.g. due to injury, excessive blood loss).

2.2 The Hypothalamus and Pituitary Gland

The hypothalamus is the region of the central nervous system and is regulated by the higher centres of the brain, and involved in maintaining homeostasis. The hypothalamus contains centres for the regulation of appetite, thirst, body temperature, sleep and wakefulness. It also regulates *biological rhythms* (*the* "*body clock*"), and these rhythms, as well as the cycle of sleep and wakefulness, are correlated with the secretion of melatonin (Fig. 2.3). The primary pacemaker of the circadian system in mammals (the "body clock") consists of two clusters of neurons, the *suprachiasmatic nuclei* (*SCN*), in the hypothalamus. The SCN is the "body clock" that controls behavioural, metabolic and physiological rhythms and can also synchronise peripheral oscillators that are found in cells, tissues and organs throughout the body (Fig. 2.3).

Melatonin is a derivative of tryptophan and is produced by *the pineal gland*. Melatonin secretion is regulated by the light-dark cycle and shown circadian rhythm with the highest concentration around midnight (Fig. 2.2).

The hypothalamus controls the secretion of *the pituitary hormones* via:

1. A neural pathway for the two neurohormones, oxytocin and vasopressin, released by the posterior pituitary
2. A humoral pathways and the pituitary portal system (involving releasing hormones and statins) to the anterior pituitary

Oxytocin (*OT*) physiological effects are lactating breast (milk ejection) and the uterus during pregnancy (uterine contraction during parturition).

Vasopressin (*AVP*) physiological effects are to increase water reabsorption in the kidneys (antidiuretic effect) and is a potent vasoconstrictor (vasopressin effect). It is released in response to the increased osmolality of the plasma, which stimulates osmoreceptors in the anterior hypothalamus.

The humoral factors which stimulate the *secretion of pituitary hormones* include growth hormone-releasing hormone (GHRH), thyrotropin-releasing hormone

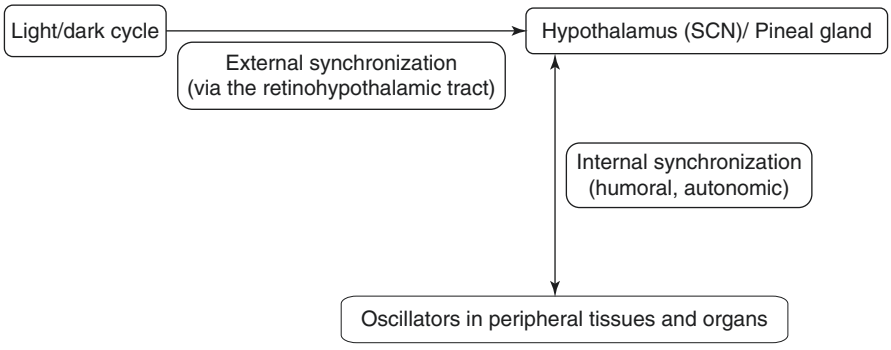

Fig. 2.3 Some interactions between the "body clock" (SCN), pineal gland, peripheral oscillators and the environment (light/dark cycle)

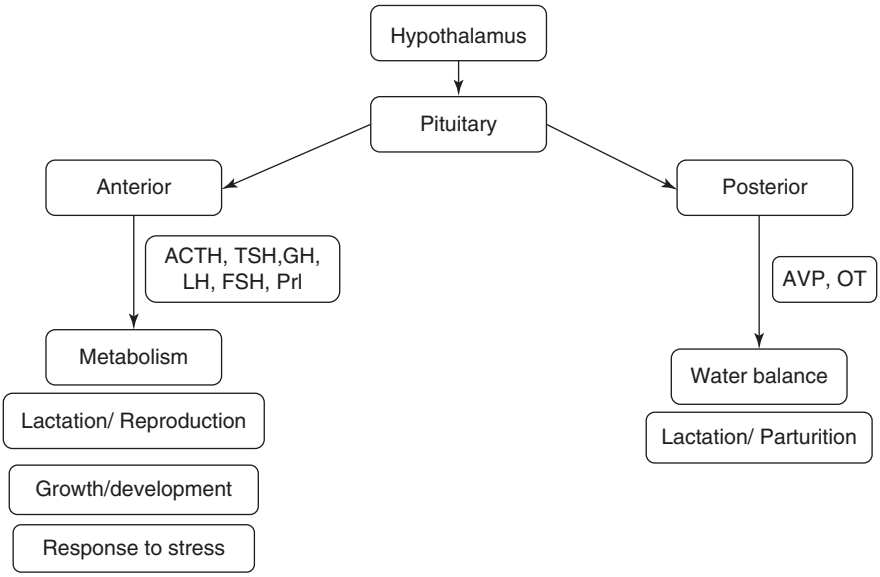

Fig. 2.4 A functional relationship between the hypothalamus and the pituitary gland. *GH* growth hormone, *TSH* thyrotropin, *ACTH* corticotropin, *LH* luteinising hormone, *FSH* follicle-stimulating hormone, *Prl* prolactin, *AVP* arginine vasopressin, *OT* oxytocin

(TRH), corticotropin-releasing hormone (CRH) and gonadotropin-releasing hormone (GnRH). The statins released are somatostatin and dopamine (Fig. 2.4).

The pituitary gland takes a central role in the regulation of the endocrine system, closely connected to the hypothalamus and affecting the function of other endocrine glands through the production and release of trophic hormones. The pituitary gland consists of two parts:

1. The anterior part (adenohypophysis)
2. The posterior part (neurohypophysis)

The posterior part (the neurohypophysis) consists of nerve endings that originate from nuclei of the hypothalamus and is the place of the storage and release of oxytocin and vasopressin.

The anterior part (the adenohypophysis) communicates with the hypothalamus via the pituitary portal system and produces hormones that control the trophic activity of peripheral endocrine glands. These trophic hormones and their secretions are:

1. Somatotrophic cells, producing growth hormone (GH)
2. Lactotrophic cells, secreting prolactin (Prl)
3. Thyrotrophic cells secreting a thyroid-stimulating hormone (TSH)
4. Gonadotrophic cells, secreting the gonadotrophins (LH and FSH)
5. Adrenocorticotrophic cells, secreting an adrenocorticotrophic hormone (ACTH)

2.3 Thyroid Gland

The thyroid gland is located at the anterior side of the neck. It is composed of two lobes connected by an isthmus. The thyroid gland synthesises two sets of hormones:

1. Follicular epithelial cells, secreting tyrosine-derived *thyroid hormones*: tetraiodothyronine (T_4) and triiodothyronine (T_3); these hormones are regarded as essential in thyroid physiology and pathology.
2. C cells (parafollicular cells), secreting *calcitonin*, a polypeptide hormone involved in the metabolism of calcium

The secretion of thyroid hormones is under the control of pituitary thyroid-stimulating hormone (TSH) which, in turn, is controlled by the hypothalamic secretion of thyrotropin-releasing hormone (TRH). Thyroid hormones provide negative feedback inhibition to the hypothalamus and pituitary gland, inhibiting the secretion of TRH and TSH.

TSH concentration is critical for the distinction between primary and secondary thyroid dysfunction.

The synthesis of thyroid hormones requires iodine, which is taken up by the follicular cells. Iodine required to maintain thyroid hormone synthesis; absorbed from dietary sources (iodised salt, seafood, plants).

In the circulation, thyroid hormones circulate predominantly (99%) bound to carrier proteins. Free T_4 and T_3 account for less than 1% of the total amount of thyroid hormone in the blood and represents the active form of both. The basic processes regulated by thyroid hormones (Table 2.1).

2.4 The Parathyroid Glands

The parathyroid glands are located on the posterior side of the thyroid.

Table 2.1 Physiologic effects of thyroid hormones

A target on	The effect of thyroid hormones
Metabolism	Acceleration of metabolic rate, oxygen consumption Energy and heat production
Cardiovascular system	Cardiac inotropic and chronotropic effects An increase in cardiac output and blood volume, a decrease in systemic vascular resistance
Digestive system	Increased intestinal peristalsis
Endocrine system	Supports the secretion and action of other hormones
Nervous system	Essential for brain development and maturation
Fat tissue/muscles	Catabolism
Bone	Proper skeletal development and bone renewal

Parathyroid chief cells synthesise and secrete *parathyroid hormone* (*PTH*) that is important for the regulation of *calcium homeostasis*. A rise in serum calcium concentration inhibits the synthesis of PTH, but the production is restarted as soon as the concentration of serum calcium drops. The concentration of plasma calcium (Ca^{2+}) is under the control of mainly:

1. Parathyroid hormone (PTH)
2. Calcitonin
3. Vitamin D_3 (1.25 dihydroxycholecalciferol [1.25 $(OH)_2D_3$])

But several other hormones, most notably thyroxin, cortisol and growth hormone, also contribute. PTH is related to the metabolism of *vitamin D*, the two of them working together to regulate calcium levels and its metabolism.

The main functions of PTH can be summarised as follows:

1. Stimulation of bone resorption by osteoclasts, leading to a release of calcium and phosphate into the blood
2. Stimulation of calcium reabsorption in the renal tubules
3. Inhibition of phosphate reabsorption in the renal tubules
4. Stimulation of renal production of 1,25 dihydroxy vitamin D_3 (calcitriol)

Precursors of vitamin D, derived from food or formed in the skin, are hydroxylated in the liver and then again in the kidneys to produce the biologically active form of vitamin D; ($1,25(OH)_2D_3$ [calcitriol]). PTH and phosphate depletion act independently on the kidney to promote it to form calcitriol. Low serum calcium stimulates the production of PTH, which stimulates the hydroxylation of vitamin D in the kidney.

Vitamin D_3 regulates:

1. In the kidney reabsorption of calcium
2. Intestinal absorption of calcium and phosphorus
3. In the bones deposition of calcium and phosphorus

Calcitonin is secreted by C cells of the thyroid gland and is involved in the metabolism of calcium homeostasis. It is secreted in response to an increase in the concentration of ionised calcium in the blood and regulates:

1. Transport and incorporation of calcium into bones
2. Increase excretion of calcium in the kidney

2.5 Adrenal Glands

The adrenal glands are two retroperitoneal organs located on the upper poles of the kidneys and consist of:

1. Core (an inner part)
2. Cortex (an outer part)

The adrenal cortex consists of three layers:

1. Zona glomerulosa, in where are produced mineralocorticoids
2. Zona fasciculate, in where are produced corticosteroids
3. Zona reticularis, in where are produced androgens

In the adrenal core (medulla), the *catecholamines* are synthesised. The effects provoked by catecholamine are:

1. Increase in the rate of the heartbeat and stronger myocyte contraction
2. Vasoconstriction of blood vessels, but also vasodilation in muscle and liver vasculatures at low concentrations
3. Stimulation of renin release
4. Promote glycogenolysis in the liver
5. Lipolysis of fat tissue
6. Inhibition of intestine peristalsis
7. Activation of sweating

The secretion of *glucocorticoids and androgens* is regulated by the hypothalamus and pituitary gland.

The hypothalamus produces the neuro-hormone corticotropin-releasing hormone (CRH), which stimulates the secretion of corticotropin (ACTH) by the pituitary cells. ACTH stimulates hormone receptors in the cortex of the adrenal gland.

Regulation of the hypothalamic–pituitary–adrenal axis takes place by negative feedback mechanisms.

The synthesis of *mineralocorticoids* is controlled by the renin–angiotensin–aldosterone axis. The most important factors in triggering the secretion of aldosterone are angiotensin 2 and potassium ions.

Mineralocorticoids are necessary to maintain the correct concentrations of sodium and potassium, and the correct volume of extracellular fluid.

Aldosterone controls the reabsorption of sodium ions and excretion of potassium and hydrogen ions by the distal nephron. Excessive production of aldosterone leads to sodium and water retention and increased excretion of potassium and magnesium ions.

Cortisol is an important catabolic hormone, which regulates many metabolic processes that provide homeostasis and allows adaptation to stressful situations (Table 2.2).

Cortisol circadian rhythm shows a maximum concentration in the morning and a minimum around midnight (Fig. 2.2). The rhythm is regulated by the suprachiasmatic nucleus (SCN) which is located in the hypothalamus (Fig. 2.3).

2.6 Endocrine Pancreas

The pancreas gland consisted of endocrine and exocrine cells. The products of the pancreatic endocrine cells are mainly *insulin* and *glucagon.*

Table 2.2 Physiologic effects of glucocorticoids

A target on	The effect of glucocorticoids
Carbohydrates	Induce insulin resistance Stimulation of gluconeogenesis in the liver
Proteins	Stimulation of protein breakdown in muscles and protein synthesis in the liver
Lipids	Stimulation of lipids breakdown
Appetite	Increase of food intake
Water and electrolytes	Absorption of sodium and water by the kidneys
Immune system	Inhibition of leukocyte migration and of proliferation of lymphocytes Inhibition of pro-inflammatory cytokines synthesis

The pancreatic endocrine mass constitutes of two endocrine cell types (beta and alpha). *Insulin* is the product of the beta cells. *Glucagon* is the product of the alpha cells. A small number of delta cells secrete somatostatin, and an even lower number of cells secrete pancreatic polypeptide.

Glucose is the principal stimulus for insulin release from the pancreatic beta cells. After a meal, insulin secretion is a multioscillatory process with ultradian oscillation of 50–120 min with secretory pulses intervales of about 10 min.

Insulin and glucagon release is regulated by glucose concentration and also by different hormones and metabolites, as well as hormones (glucagon-like peptide 1) and neurotransmitters (acetylcholine).

Insulin and glucagon have opposite metabolic effects. Insulin has a stimulating effect on the energy storage process, that is, *anabolism* and glucagon stimulated energy consumption, that is the *catabolism*.

Insulin has an anabolic effect on the liver, skeletal muscle and adipose tissue, and glucagon has a catabolic effect on the liver. Insulin secretion is reduced during fasting and as a result of stress or injury.

Together, insulin and glucagon coordinate the metabolism of carbohydrates, lipids and proteins.

Insulin has several functions:

1. Supports fat synthesis and storage in adipose tissue
2. Inhibits the release of fatty acids from the adipose tissue
3. Promotes glucose transport into adipocytes
4. Causes storage of fatty acids in fat cells

Chapter 3
Electrocardiogram (ECG)

Kiyoko Yokoyama

Abstract The autonomic nervous system controls the fluctuation of the heartbeat interval. The autonomic nervous system consists of the sympathetic nervous system and the parasympathetic nervous system, and the sympathetic nervous system increases the activity of the whole body and increases heart rate and blood pressure. The parasympathetic nervous system stores energy, promotes gastrointestinal motility, and decreases heart rate and blood pressure. Since the autonomic nervous system regulates internal organs, blood vessels, glands, etc., regardless of volition, and the heartbeat interval fluctuates under the control of the autonomic nervous system, heart rate variability, which quantifies the characteristics of the fluctuation of the heartbeat interval, has been studied as an evaluation indicator for the mental and physical condition.

In this chapter, the representative indicators of heart rate variability are introduced in Sect. 3.2, maintaining and improving arousal by cardiorespiratory phase synchronization in Sect. 3.3, and examples of comparison between the indicators of heart rate variability obtained from wearable terminals whose use frequency is increasing in recent years and the indicators of heart rate variability calculated from the conventional R–R intervals are shown in Sect. 3.4.

Keywords Heart rate variability · Autonomic nervous system · Mental and physical condition · Cardiorespiratory phase synchronization · Wristwatch-type heartbeat monitor

K. Yokoyama (✉)
Graduate School of Design and Architecture, Nagoya City University, Nagoya, Aichi, Japan
e-mail: yokoyama@sda.nagoya-cu.ac.jp

H. Takada, K. Yokoyama (eds.), *Bio-information for Hygiene*, Current Topics in Environmental Health and Preventive Medicine,
https://doi.org/10.1007/978-981-15-2160-7_3

3.1 Introduction

The autonomic nervous system controls the fluctuation of the heartbeat interval. The autonomic nervous system consists of the sympathetic nervous system and the parasympathetic nervous system, and the sympathetic nervous system increases the activity of the whole body and increases heart rate and blood pressure. The parasympathetic nervous system stores energy, promotes gastrointestinal motility, and decreases heart rate and blood pressure. Since the autonomic nervous system regulates internal organs, blood vessels, glands, etc., regardless of volition, and the heartbeat interval fluctuates under the control of the autonomic nervous system, heart rate variability, which quantifies the characteristics of the fluctuation of the heartbeat interval, has been studied as an evaluation indicator for the mental and physical condition [1].

Thayer et al. reported in their review article that autonomic imbalance is one of the risk factors for cardiovascular disease, and heart rate variability decreases [2]. Singh et al. reported that heart rate variability decreases in patients with hypertension compared with healthy subjects, and that heart rate variability may be used to assess risk [3]. Schroeder et al. clarified through cohort study that heart rate variability decreases in diabetes and metabolic syndrome patients [4]. Taelman et al. described that mental stress affects heart rate and heart rate variability [5]. Yamamoto et al. reported the effectiveness of heart rate variability as an evaluation indicator of chronic fatigue [6]. Park et al. use heart rate variability as a relaxation evaluation index [7]. As you can see, heart rate variability is used as an index for evaluating the mental and physical conditions in various situations.

3.2 Heart Rate Variability Indicator

The time series of heart rate variability generally uses the time interval between the R waves of an electrocardiogram. When the autonomic nervous system activity index is calculated from the heart rate variability time series, it is desirable that the sampling frequency of the electrocardiogram be 200 Hz or higher [1]. The use of pulse waves is sufficient for the calculation of a heart rate time series at intervals of several seconds, and the pulse waves can be measured from the fingertip or the wrist by a photoelectric conversion sensor. Pulse waves are used in heart rate measurements by smartwatches and smartphones. Section 3.2 outlines typical heart rate variability indices derived from ECGs. Figure 3.1 shows an example of (a) ECG and (b) R–R interval time series. The part marked R in (a) is called the R wave and corresponds to ventricular excitation. The time intervals between adjacent R waves are called R–R intervals, and an example of this time series is shown

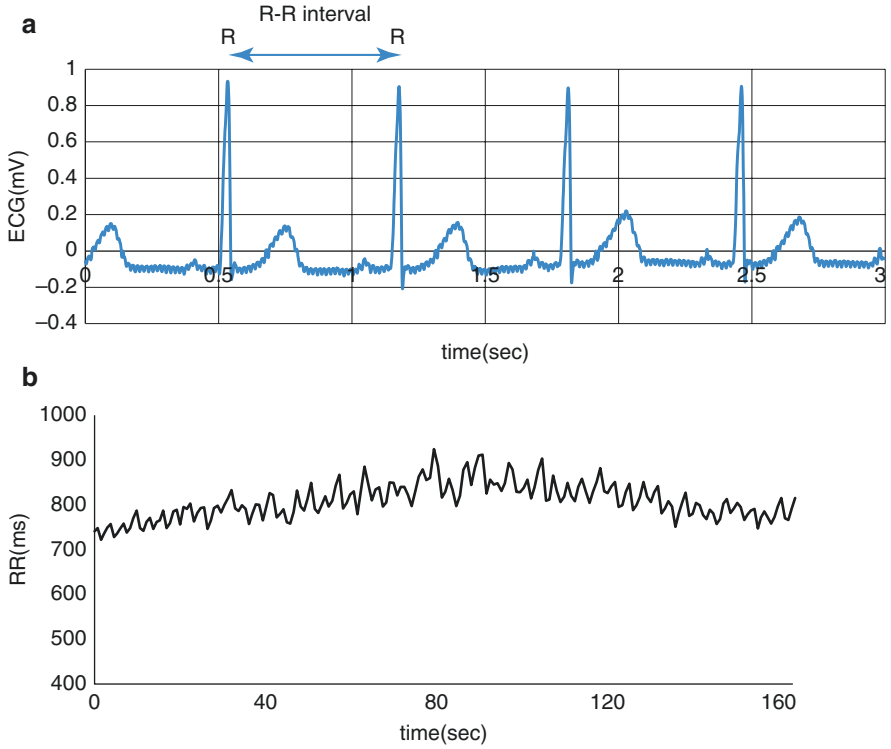

Fig. 3.1 (**a**) ECG (**b**) R–R interval time series

in (b). The following indicators are often calculated over a time window of 2–5 min.

1. R–R mean value: In many cases, the value corresponding to heart rate is obtained by dividing 1 min by this mean value.
2. Coefficient of variance (CVrr): The standard deviation of the R–R interval of 100 beats divided by the mean, or the standard deviation of the R–R interval within a time window divided by the mean. It has been reported that CVrr was negatively correlated with PaCO2 and indicates respiratory insufficiency in patients with Duchenne muscular dystrophy [8].
3. RMSSD: An index expressed by Eq. (3.1), which increases when parasympathetic nervous system activity accelerates.

$$\mathrm{RMSSD} = \sqrt{\sum_{t=2}^{n} \left(\mathrm{RR}(t) - \mathrm{RR}(t-1)\right)^2 / (n-1)} \tag{3.1}$$

4. ARV: The ratio of the variance of the residual $Z(t)$ to the variance of the time series shown in Eq. (3.3) by fitting the autoregressive model to the time series in Eq. (3.2)

$$\mathrm{RR}(t) = \sum_{j=1}^{p} a(j)\,\mathrm{RR}(t-j) + Z(t) \tag{3.2}$$

$$\mathrm{ARV} = S_z^2 / S_R^2 \tag{3.3}$$

where RR(t) of Eq. (3.2) is the R–R interval time series, a (j) is the linear prediction coefficient of the autoregressive model, p is the order of the model, and $Z(t)$ is the residual time series of the model. The ARV represented by Eq. (3.2) is a value obtained by dividing the variance (S_Z^2) of the residual $Z(t)$ by the variance (S_R^2) of the RR(t), and it is 1 for a white noise time series and 0 for a regular time series, indicating the irregularity of time series.

5. LF, HF, and LF/HF: We will calculate the frequency power spectrum from an R–R interval time series. Let LF be the area of the power spectrum between 0.04 and 0.15 Hz and HF be the area of the power spectrum between 0.15 and 0.4 Hz. HF increases as parasympathetic activity accelerates, and LF/HF is widely used as an index related to sympathetic activity [9]. HF and RMSSD are highly correlated indices. For the calculation of the power spectrum, Fourier transformation, AR method, Maximum Entropy Method (MEM), and the like are used. The area of the power spectrum represents the variance of the fluctuation, and a value corresponding to the amplitude of the fluctuation can be calculated by taking the square root of this value.

3.3 Maintaining and Improvement Arousal by Cardiorespiratory Phase Synchronization [10]

The heart rate variability index has generally been utilized for the evaluation of mental and physical conditions. In Sect. 3.3, we introduce a case in which heartbeat respiration phase synchronization is induced by consciously or unconsciously controlling respiration, and as a result, maintenance and improvement effects of arousal are observed. Cardiorespiratory phase synchronization indicates that the phase of the timing of the heartbeat in one cycle of respiration becomes substantially constant every breath [11]. Figure 3.2a shows a case in which cardiorespiratory phase synchronization occurs, and Fig. 3.2b shows a case in which phase synchronization does not occur. The figure shows a respiratory curve, an ECG, and a synchrogram. The synchrogram shows the phase of one cycle of respiration from 0 to 1 on the vertical axis. The horizontal axis represents time, and a point is plotted corresponding to the heartbeat by using the time when the heartbeat occurs as the x-coordinate and the phase of respiration at that time as the y-coordinate. When the heartbeat occurs at the same phase of each breath as in (a), the dots are arranged in stripes.

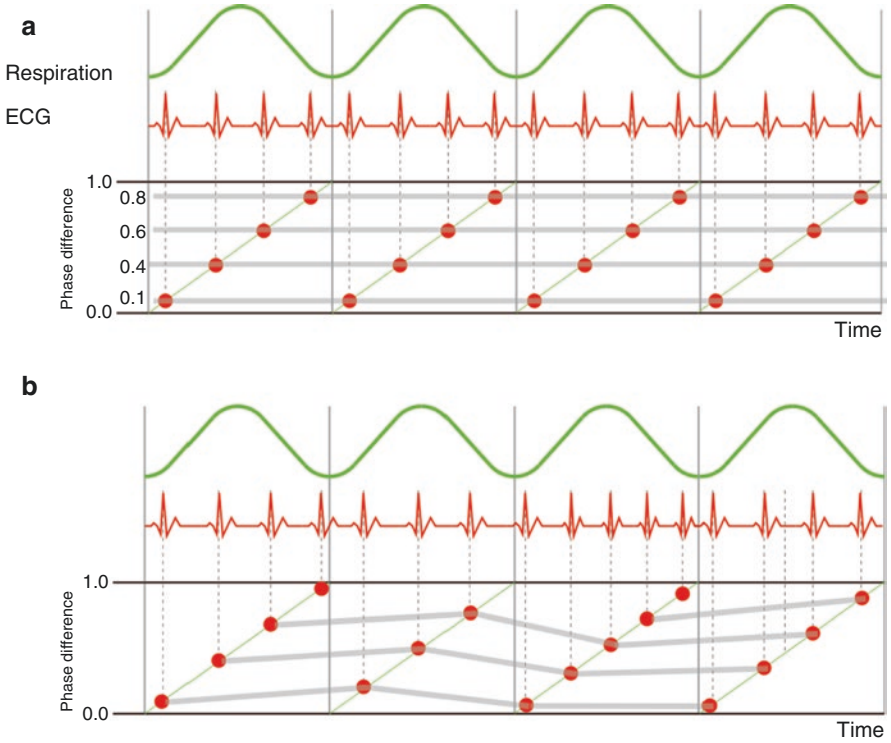

Fig. 3.2 Schematic diagram of the respiratory curve, ECG, and Synchrogram. Synchronization (**a**) Synchronization. (**b**) Asynchronization

Table 3.1 Increase in SpO2 during resting during respiratory control

Respiratory control	SpO2 increased rate comp. rest (%)
1 Hz	0.68 ± 0.8
Random	0.33 ± 0.7
Heartbeat	1.01 ± 0.6, $p < 0.01$ (comp. rest)

When the phase synchronization shown in (b) does not occur, the *y*-coordinate of the plotted point becomes random. It has been reported that blood oxygen saturation increases due to the occurrence of cardiorespiratory phase synchronization [12]. It has also been reported that when the high blood oxygen saturation increases, the arousal level is high [13].

First, for a basic experiment, 16 male university students participated for 15 min. They rested for 5 min. Then, following sounds for 5 min, they engaged in respiratory control with inspiration for 2 sounds and expiration for 2 sounds. Finally, they had 5 min of electrocardiogram and respiration. Three types of rhythm were compared: 1 s intervals, random intervals of 1 s on average, and heartbeat interval. Compared to the rest before and after, for each, cardiorespiratory phase

Table 3.2 Relationship between the timing of heartbeat synchronization sound for respiration and SpO2

Respiration timing	SpO2 increased rate comp. rest (%)
1: 1	0.80 ± 0.9
2: 2	1.01 ± 0.6, $p < 0.01$ (comp. rest)
3: 3	0.68 ± 1.0

synchronization was significant only when synchronized with heartbeat interval. For changes in blood oxygen saturation, Table 3.1 shows the increase in blood oxygen saturation relative to rest during the three types of respiratory control described above. As a result of a corresponding *t*-test for oxygen saturation at rest and during respiratory control, oxygen saturation increased significantly at $p < 0.01$ only during respiratory control with the sound synchronized with heartbeat. Table 3.2 shows the amount of increase in oxygen saturation during respiratory control relative to rest, with respect to the three types of respiration rates: repeated exhalation and inspiration for every 1 sound (1:1), repeated exhalation and inspiration for 2 sounds (2:2), and repeated exhalation and inspiration for 3 sounds (3:3). The paired *t*-test showed a significant increase in oxygen saturation during respiratory control than at rest only at 2:2, $p < 0.01$. From these, it has been confirmed that phase synchronization of the heartbeat respiration occurs by 2 heartbeats of respiration and 2 of expiration, and that blood oxygen saturation increases.

Next, during a 1-h driving operation using the driving simulator, at the time points of 30 min and 45 min after starting the driving, vibration stimulation was applied from the seat back for 1 min at timing synchronized with the heartbeat. The vibration was applied for 65 ms from the time point when the electrocardiogram R wave was observed. Sixteen male and female university students participated in the experiment. For the 32 cases (2 times each for 16 experimental participants, at 30 min and 45 min point of time), the intensity and oxygen saturation of the cardiorespiratory phase synchronization for 1 min immediately before the stimulation, 1 min during the stimulation and 1 min after the stimulation showed a significant fluctuation in the one-way ANOVA. In the multiple tests, cardiorespiratory phase synchronization was significantly generated at the time of the stimulation compared to just before the stimulation, and the oxygen saturation significantly increased for 1 min after the stimulation. In addition, subjective evaluation values for sleepiness significantly increased for 1 min before and 1 min after application of the stimulus, and sleepiness was significantly eliminated in objective evaluation based on facial expression. From the above, it was possible to attain the possibility of increasing the degree of oxygen saturation in the blood by applying vibratory stimulation at intervals synchronized with the heartbeat. In this case, the instruction to intentionally perform the respiratory control was not given, and it is plausible that the vibration stimulation unconsciously controlled the respiration and generated the cardiorespiratory phase synchronization. Therefore, biofeedback of heartbeat rhythm has the potential to be used as a method for maintaining and improving arousal to realize individual adaptation without making people feel stress during work and driving, which require concentration.

3.4 Heart Rate Variability Measured by Wearable Devices

Heart rate information measured by smartphones and smartwatches is generally based on pulse waves. Compared with the R wave of the electrocardiogram, the pulse wave has a smoother waveform and the calculation accuracy of the beat interval is lower. In addition, compared with an electrocardiogram in which an electrode is attached to bare skin for measurement, a pulse wave does not require electrodes to be attached and is easy to measure, but on the other hand, noise reduction and data loss occur because the measurement position is not fixed. However, the ease of measurement and the ability to collect big data in the cloud make it very useful from the viewpoint of health management and preventive medicine.

Here, we describe the comparison results of heart rate variability indices measured from the electrocardiogram and the smartwatch, taking as an example the data obtained by simultaneously measuring the heart rate time series at 1-s intervals using an electrocardiogram and a smartwatch. Figure 3.3 is a graph showing the electrocardiogram R–R interval time series and the time series obtained by converting the heart rate at 1-s intervals measured simultaneously with a smartwatch into a value corresponding to the heartbeat interval. The time series measured with the smartwatch shown in blue versus the R–R interval shown in orange is a smoothed shape. The correlation coefficient between R–R interval and smartwatch measured data was calculated for each 19 samples, and it was distributed between 0.75 and 0.41.

The mean values of mean heart rate, standard deviation, coefficient of variance, RMSSD, HF, LF, and LF/HF of 126 cases calculated at 2-min intervals from the ECG and smartwatch measurement data of 19 participants who were cooking for between 10 and 15 min in a standing position are shown in Table 3.3. The error rate is expressed as a percentage by dividing the absolute value of the difference between

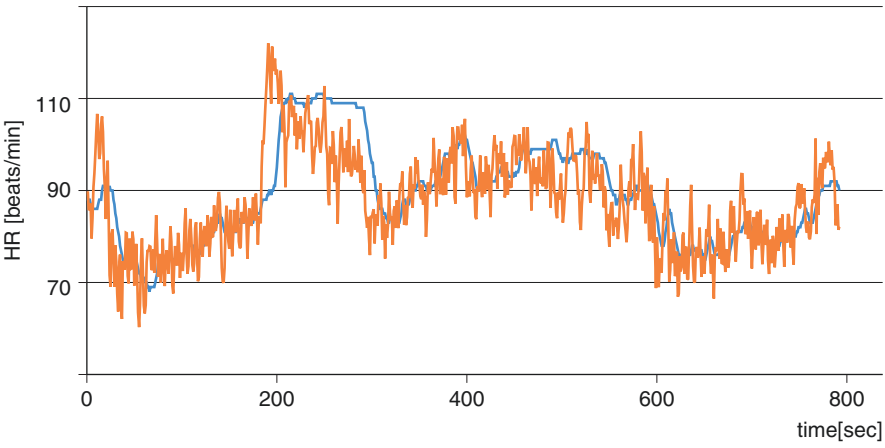

Fig. 3.3 Instantaneous heart rate measured from ECG (orange line) and smartwatch (blue line)

Table 3.3 Error rate and correlation coefficient of ECG and smartwatch

	HR	SD	CV	rM SSD	LF	HF	LF/HF
Error rate (%)	1.92	36.82	36.6	81.37	64.13	77.34	80.92
Correlation	0.98	0.82	0.74	0.76	0.37	0.49	0.22

the value calculated by the smartwatch and the value calculated from the R–R interval by the value calculated from the R–R interval. As for the average heart rate, the correlation coefficient is 0.98 and the error rate is 1.9%, which shows that there is no problem in the data measured by the smartwatch. The standard deviation, the coefficient of variance, and the RMSSD, which are time-domain indicators, have a correlation coefficient of 0.74 or higher, which is higher than the LF, HF, and LF/HF, which are frequency-domain indicators, suggesting that it is preferable to calculate time-domain indicators when using smartwatches. The reason why the error rate is large in the RMSSD is considered to be that, as shown in Fig. 3.3, since the time series is smoothed compared with the R–R interval, the high-frequency component is attenuated, and as a result, the amplitude of the high-frequency component is reduced.

3.5 Conclusion

This chapter introduces a representative index of heart rate variability, which is an evaluation index of autonomic nervous activity balance and introduces the characteristics of the heart rate variability index measured from wearable terminals, that the maintenance improvement of arousal effect can be obtained by utilizing biofeedback. The heart rate variability index can be widely used to estimate mental and physical conditions necessary for health management and disease prevention in daily life such as relaxation evaluation in addition to stress and fatigue evaluation. In addition to estimating mental and physical conditions, heart rate variability can be used for biofeedback as an effective interaction with the body for health management and disease prevention. Furthermore, heart rate information measured with a wearable terminal can be easily measured without interfering with daily life, and big data can be easily collected. Therefore, by developing a new autonomic activity balance evaluation index that is different from those previously calculated from electrocardiograms, we believe we can greatly contribute to health management and disease prevention.

References

1. Camm AJ, Malik M, Bigger JT, et al. Heart rate variability: standards of measurement, physiological interpretation and clinical use. Task Force of the European Society of Cardiology and the North American Society of Pacing and Electrophysiology. Circulation. 1996;93–5:1043–65.

2. Thayer JF, Yamamoto SS, Brosschotc JF. The relationship of autonomic imbalance, heart rate variability and cardiovascular disease risk factors. Int J Cardiol. 2010;141(2):122–31.
3. Singh JP, Larson MG, Tsuji H, Evans JC, O'Donnell CJ, Levy D. Reduced heart rate variability and new-onset hypertension. Hypertension. 1998;32(2):293–7.
4. Schroeder EB, Chambless LE, Liao D, Prineas RJ, Evans GW, Rosamond D, Heiss G. Diabetes, glucose, insulin, and heart rate variability -the atherosclerosis risk in communities (ARIC) study. Diabetes Care. 2005;28(3):668–74.
5. Taelman J, Vandeput S, Spaepen A, Van Huffel S. Influence of mental stress on heart rate and heart rate variability. In: 4th European Conference of the International Federation for Medical and Biological Engineering. 2009. p. 1366–9.
6. Yamamoto Y, Lamanca JJ, Benjamin HA. Measure of heart rate variability is sensitive to orthostatic challenge in women with chronic fatigue syndrome. Exp Biol Med. 2003;228(2):167–74. https://doi.org/10.1177/153537020322800206.
7. Park SA, Song C, Oh YA, Miyazaki Y, Son KC. Comparison of physiological and psychological relaxation using measurements of heart rate variability, prefrontal cortex activity, and subjective indexes after completing tasks with and without foliage plants. IJERPH. 2017;14(9):1087. https://doi.org/10.3390/ijerph14091087.
8. Mochizuki H, Okahashi S, Ugawa Y, Tamura T, Suzuki M, Miyatake S, Shigeyama T, Ogata K, Kawai M. Heart rate variability and hypercapnia in Duchenne muscular dystrophy. Pediatr Cardiol. 2008;47(21):1893–7.
9. Task Force of the European Society of Cardiology the North American Society of Pacing Electro-physiology. Heart rate variability—standards of measurement, physiological interpretation, and clinical use. Circulation. 1996;93(5):1043–65.
10. Takahashi I, Takaishi T, Yokoyama K. Overcoming drowsiness by inducing cardiorespiratory phase synchronization. IEEE Trans Intell Trans Syst. 2014;15(3):982–91.
11. Bucher K, Bucher KE. Cardio-respiratory synchronisms: synchrony with artificial circulation. Res Exp Med. 1977;170(2):101–8.
12. Galletly DC, Larsen PD. Cardioventilatory coupling during anaesthesia. Br J Anaesth. 1997;79(1):35–40.
13. Sung EJ, et al. Effects of oxygen concentrations on driver fatigue during simulated driving. Appl Ergon. 2005;36(1):25–31.

Chapter 4
Electrogastrography

Kohki Nakane, Keita Ichikawa, Rentaro Ono, and Yasuyuki Matsuura

Abstract Electrogastrography (EGG) is a noninvasive method of measuring gastric electrical activity via cutaneous electrodes placed on the abdomen. Compared to other gastrointestinal motility measurement methods, such as the gastric-emptying and internal pressure measurement techniques, the EGG is noninvasive and allows measurement with minimum restriction, thereby allowing prolonged measurements. In addition, since the EGG measures gastrointestinal electric activity, which cannot be quantified by other methods, it can be used to evaluate the state of the body and any pathological conditions, which might provide new insights into the prevention of gastrointestinal dysfunctions associated with various disorders. Assessment of the abnormal gastrointestinal activities in EGGs is particularly useful for preventing disorders, such as functional dyspepsia and gastrointestinal motility disorder. Thus, the EGG has importance in public health, although its range of applications is still limited. Also, some novel methods such as nonlinear analysis and artificial intelligence (AI) are applied to the analysis of the EGGs.

Keywords Electrogastrogram (EGG) · Noninvasive measurement · Gastrointestinal motility · Artificial intelligence (AI) · Deep-learning

K. Nakane · K. Ichikawa · R. Ono
University of Fukui, Fukui, Japan

Y. Matsuura (✉)
University of Fukui, Fukui, Japan

Gifu City Women's College, Gifu, Japan
e-mail: matsuura@gifu-cwc.ac.jp

H. Takada, K. Yokoyama (eds.), *Bio-information for Hygiene*, Current Topics in Environmental Health and Preventive Medicine,
https://doi.org/10.1007/978-981-15-2160-7_4

4.1 Introduction

Electrogastrography (EGG) can help evaluate gastrointestinal (GI) motor function via measured electrical activities of the GI system as biological signals. The EGG is a method of measuring the electrical activities that control the movements of the digestive tract without restraining the subject. In 1921, Alvarez first attempted to record the electrical activity of the human stomach from the surface of the body [1]; this record was named the electrogastrogram. However, the EGG requires special equipment and is likely to be affected by the electromyogram (EMG) owing to the respiratory movements associated with the diaphragm and electrocardiogram (ECG); because the evoked potentials of the GI system detected on the abdominal walls are weak, research and development in this field has been long hampered. Recently, however, recording the electrical activity of the GI system has been facilitated by the development of new measurement devices and digital circuit technologies, leading to a notable increase in clinical research. In addition, the electrogastrogram designed exclusively for the EGG and electrogastroenterogram (EGEG), i.e., measurement of the motor functions of the stomach, small intestine, and colon, have been proposed as extensions of the EGG (intestinal movements have also been discussed as EGG).

Moreover, diseases associated with abnormal GI activities, such as constipation and functional dyspepsia (FD), have emerged as critical issues, which may cause lifestyle-related diseases. In particular, constipation is considered as a common complaint among patients with latent FD and elderly individuals, and this topic is also of interest with respect to hygiene.

Since the EGG can be performed noninvasively and without restrictions, compared with other tests of the GI motor function, such as gastric-emptying and internal pressure measurement methods, measurements obtained in a state close to the physiological condition or over long durations of time are possible. In this chapter, therefore, the methods for the measurement and analyses of EGG are outlined. Further, the latest research trends in the EGG evaluations using artificial intelligence (AI) are described, and the future prospects are discussed.

4.2 Mechanism

4.2.1 Physiological Mechanism of EGG

EGG involves percutaneous recording of the electrical activities of the stomach using electrodes attached to the abdominal surface on the body. Therefore, the EGG can be performed noninvasively without placing any restrictions on the subject, and the motor functions and autonomic activities of the upper digestive tract can be objectively evaluated by analyzing the obtained graphs.

Rhythmic electrical activity consisting of alternating depolarizations and repolarizations are observed in the stomach and small intestine, similar to that in the

heart. The pacemaker of the electrical activity of the stomach is located on the greater curvature side of the upper third of the body of the stomach and discharges impulses at the rate of 3 times per minute (3 cycles per minute, cpm) toward the pylorus. This pacemaker is controlled by parasympathetic activities but spontaneously discharges periodically owing to a network of cells called the interstitial cells of Cajal (ICCs) [2, 3]. The ICCs were identified only recently as the pacemaker cells responsible for the movements of the digestive tract.

In 1998, the ICCs were directly observed to express rhythmic changes in electrical currents and induce spontaneous contractions, which were used to confirm their role as the pacemaker cells of the digestive tract [4, 5]. Although the ICCs were shown to be involved in the spontaneous activities of the digestive tract and neural regulation of its movements, questions regarding the mechanism by which they generate rhythms and the cell structures that constitute the pacemaker remain unanswered, motivating research on these problems [6]. Electrophysiologically speaking, the ICCs are present in the muscle layer of the digestive tract, which discharges rhythmic action potentials and contracts spontaneously; these determine the intensity and frequency of the electrical activity of the stomach under the influence of neural and humoral factors [7, 8].

In the electrical activity of the stomach, periodic vibrations are generated in the excitation conducting network of smooth muscle cells, with modifications by the ICCs and nerve activities. However, peristaltic activities are not generated by the electric impulses discharged by the ICCs alone. Action potentials are generated when the electrical activities surpass the contraction thresholds during depolarization and produce peristaltic activities. There are two types of these electrical activities, namely electrical control activity (ECA) and electrical response activity (ERA). The ECA is characterized by regularly recurring electrical potentials from the ICCs. Further, the ECA is not associated with contractions of the stomach unless coupled with action potentials, which is then referred to as the ERA [9]. EGG is used to measure both the ECA and ERA but cannot distinguish between them; hence, it does not directly record the peristaltic activities [9, 10].

To determine whether EGG truly reflects the electrical activity of the stomach, Pezzolla and Homma performed EGG studies before and after a total gastrectomy in patients with stomach cancer. They observed the complete disappearance of the periodic activity post-surgery at 3 cpm, which is characteristic of the stomach [11, 12]. This work established that the EGG could truly be a record of the electrical activity of the stomach.

In the small intestine, the ECA is known to be transmitted from the duodenal pacemaker toward the anus by gradual reduction of the frequency from 10 to 12 cpm in the duodenum to 8–10 cpm in the ileum [13, 14]. There have been reports that these intestinal electrical activities could be detected as signals with frequencies in the range of 8–12 cpm from the body surface, and using the EGEG; recording of the electrical activities of the stomach and small intestine by spectral analysis has been proposed, but the unlike the EGG, this method has not garnered wide support [13]. In addition, the frequency of potential changes due to respiration-induced abdominal wall movements is close to that of the electrical activity of the small intestine, and the frequency components based on respiration may be difficult to isolate.

Intestinal activities have been studied by some research groups; however, reports on these works are insufficient to establish their clinical utility.

4.2.2 Methods of EGG

EGG is used to measure the electrical activities associated with GI movements as evoked potentials on the abdominal surface [15]. Therefore, the measurements are obtained by attaching electrodes to the abdominal surface near the stomach and intestine. These electrodes may be unipolar or bipolar, but the measurements obtained using unipolar electrodes are more common; three to five such electrodes are commonly attached to the abdomen, and an indifferent electrode is placed either on the abdomen or the back of the subject. With regard to bipolar electrodes, a pair of electrodes is attached to the abdomen, and an indifferent electrode is placed on the abdomen, back, or dorsum of the hand. Bipolar electrodes are generally placed near the gastric pacemaker. In their experiments, Okuno et al. and Imai et al. attached five electrodes to the abdomen and performed EGG using unipolar electrodes first before employing bipolar electrodes during analyses [16, 17].

The positions of the unipolar and bipolar electrodes are not fixed [18], but a few typical examples are presented herein. In the EGG using unipolar electrodes, four electrodes are attached to the abdomen for the Nipro Electrogastrograph EG [19], but Okuno et al. placed five electrodes in the abdominal region [16]. For the EGG using bipolar electrodes, the Handbook of Electrogastrography describes a method using three electrodes on the abdominal surface [20], and Kaneoke et al. placed two electrodes near the gastric pacemaker [13, 21].

EGG is more sensitive to changes in the DC (Direct Current) due to electrode resistance and depolarization because of the markedly lower frequencies of signals than the EEG or ECG. It is necessary to use electrodes with less potential changes and reduce the inter-electrode resistance by carefully wiping the skin using an alcohol disinfectant or skin pretreatment agent [22, 23].

EGG is usually performed in the supine position to avoid artifacts due to body movements; however, the seated position is also tolerated for certain measurements, such as those with meal loading. Since the amplitudes of the signals recorded by the EGG are of the order of 100–500 μV, they are likely to be affected by the abdominal muscle EMG and ECG, whose amplitudes are of the order of several millivolts, or even show baseline instabilities due to body movements. The stability of the acquired signals must be secured by eliminating the effects of sudden noise due to the simultaneous occurrence of these artifacts. A smoothing filter using a moving average scheme, followed by elimination of the abnormal values, is necessary to cope with the sudden noise due to interference by EMG.

The pulse variation in the measurements is 1 Hz, respiratory variation is 0.25 Hz, blood pressure variation is 0.1 Hz, and body fluid volume variation is 0.17 Hz. Here, as the frequencies of the pulse variations and body fluid volume variations differ from those of the EGG signals, and as the effects of the blood pressure variations are weak despite the presence of blood vessels at the electrode placement sites, no

problems are observed. Respiratory variations are then eliminated using a low-pass filter whose frequency is close to that of the intestinal electrical activity. In particular, during measurement in the supine position, the respiratory rate is likely to slow to 0.15–0.2 Hz. Therefore, the respiratory components must be eliminated by respiration control or using low-pass filters. Generally, interferences from the ECG and respiration are prevented using a high-pass filter with a DC content of 0.032 Hz and a low-pass filter having a passband of 0.05–0.2 Hz for EGG.

4.3 Methodology to Evaluate EGG Data

4.3.1 Advantages and Limitations of EGG

Since the EGG is a noninvasive method and requires no restraint to be placed on the subject, there are no reported contraindications to its broad application; further, it can also be performed safely on children, disabled adults, and elderly people. EGG also causes very little additional stress before or after execution, such as prolonged fasting before endoscopy and the use of a laxative after barium radiography. The clinical applications of EGG are not broad, compared with those of the ECG and EEG, because the spectral analyses of the frequency and amplitude, by which EGG data are generally analyzed, do not yield much information. This restricts its applications as compared with the ECG and EEG.

Spectral analysis methods, including the fast Fourier transform (FFT), are usually employed to analyze EGG records [20], and instances using other complex analytical methods have been rarely reported. Using spectral analyses, evaluations can be obtained from measurements of length approximately 5 min because of the high temporal resolution [20]. However, while spectral analysis is useful for the evaluation of the characteristics of the electrical activity of the stomach, spectral analysis alone is presently considered insufficient, unlike spectral analysis of heart rate variations. Furthermore, in consideration of the complexities of biological activities, evaluations using complex systems analysis techniques, including chaos and nonlinear analyses, are considered indispensable. Finally, tests of linearity a previously proposed the surrogate method indicated that EGG may be nonlinear [24, 25].

4.3.2 Analytical Methods for EGG

4.3.2.1 Linear Analysis

EGG is known to reflect the transmissions of the electrical activity of the stomach and its rhythmic changes corresponding to the pacemaker frequency of the stomach, which is about 3 cpm. Therefore, time-series analysis of EGG is generally performed using numerical data sampled from the frequency range of 0.5–2.0 Hz.

Further, the duration of the time window for time-series analysis of EGG is usually 1–15 min.

Time-series analysis of the EGG data is primarily accomplished by spectral analysis, which is commonly performed using the Fourier transform or Wavelet analysis. Spectral analysis of the EGG data is performed to analyze the temporal changes in the frequency and amplitude of the EGG waves. Analysis using FFT is performed every 256 or 512 s as the temporal resolution at this level is generally sufficient for clinical assessments; however, wavelet analysis is more suited for closer analysis of the temporal changes [26]. Moreover, in the spectral analysis of EGG, the spectra are segmented at fixed durations, and the segmented spectra are superimposed to visually evaluate changes in electrical activity of the stomach; this is an often-employed method called the running spectrum analysis (RSA) [20, 27].

Other examples of spectral analyses include methods using autoregressive (AR) models [28] and the EGG analysis system using the minimum root-raised cosine spectral method [29]. At the research level, these attempts include extraction of only the EGG data using independent component analysis (ICA) [30].

4.3.2.2 Nonlinear Analysis

Attractors can be reconstructed using dynamic equation systems, such as the Duffing equation, Henon map, and Lorenz differential equation. The attractor is constructed by means of embedding the time series data proposed by Takens in phase space [31]. It is therefore interesting to note that the structure of an attractor derived from time-series data obtained via EGG can also be represented in the phase space (embedding space). The form of the attractor is regarded as a subject of mathematical interest and can be measured using Wayland [32] and Rosenstein's algorithm [33, 34].

The Lyapunov exponent is a quantity that indicates the mean divergence of two points on an attractor with time lapse and represents the widening behavioral deviation derived from a very small divergence in the initial state [35, 36]. The maximum Lyapunov exponent (MLE) is denoted as λ; if this is positive, the time series may be chaotic, oscillation waveform may be more irregular, and trajectory may be more complex, owing to a larger value [37]. However, nonlinear analysis methods show poor temporal resolution compared to spectral analyses, and further developments, such as evaluation of the analytical techniques and proposal of indices using mathematical models, are awaited [38].

4.3.2.3 Mathematical Model

While the precision of the EGG has been gradually improved, as noted above, it has been applied to the evaluations of various diseases in experiments that are mostly aimed at future clinical use. Creating precise models of normal EGG in healthy individuals may assist in the quantitative differentiation of EGG abnormalities

associated with GI disorders. This increases the possibility of diagnosing asymptomatic GI disorders, such as nonulcerative dyspepsia, by EGG and automatic EGG application to screening such disorders. EGG is therefore expected to contribute to the early detection and prevention of GI disorders associated with various diseases.

Nelsen and Sarna et al. described the electrical activity of the canine stomach using the Van der Pol equation, which explains self-oscillatory systems [39, 40]. However, the Van der Pol equation is a deterministic differential equation. In addition, other analyses using the Wayland algorithm showed that the actual EGG records were not necessarily composed of deterministic mathematical models [25]. Therefore, attempts are underway to describe such activity using stochastic differential equations [25, 38].

4.4 EGG Analysis Using AI

In recent years, the technological developments in artificial intelligence (AI) have achieved remarkable progress, and deep learning has attracted substantial attention as it is particularly good for classifications of complex data. In this section, an example of the application for an autoencoder (AE) [41], which is one of the deep-learning models, is demonstrated for classifying the EGG states. An AE is a type of artificial neural network that is used to learn efficient data coding in an unsupervised manner; it is one of the deep-learning models that specializes in dimensional compression of data and comprises an encoder to compresses the input data and a decoder to restore the compressed data to their original forms [41].

The subjects were seven healthy males aged between 21 and 24 years (mean ± standard deviation: 22.71 ± 0.70 years) without arrhythmic or GI diseases or symptoms. They were instructed to avoid caffeine, spices, oily food, alcohol, smoking, and strenuous exercise on the day before the measurements. The subjects were fully briefed on the experiment in advance, and their written consent was obtained. The study protocols and procedures were approved by the Ethics Committee of the University of Fukui Graduate School of Engineering.

The experiments were conducted in a soundproofed laboratory, and the room temperature was set at 22–24 °C. The EGG data were measured for 90 min for each subject before and after lunch. The subjects ingested some balanced nutrition food (solid type) and water at lunch. After attaching the disposable electrodes to their chest and abdomen, the subjects were moved to a bed and the EGG data were recorded in the supine position excluding when they were eating. EGGs were obtained at 10 Hz by amplifying using a bio-amplifier (Inter cross, Japan) and recording with a recorder (LX-110; TEAC, Japan). The same measurements were obtained after lunch, at 0:30 pm. A high-pass filter with a treble cutoff frequency of 0.05 Hz and a low-pass filter with a cutoff frequency of 0.15 Hz were applied to the obtained data to remove noise from the EMG and electronic devices.

In this experiment, five disposable electrodes (Vitrode M; Nihon Kohden Inc., Japan) were affixed to ch1–ch2 and “e,” as shown in Fig. 4.1. The electrode affixed

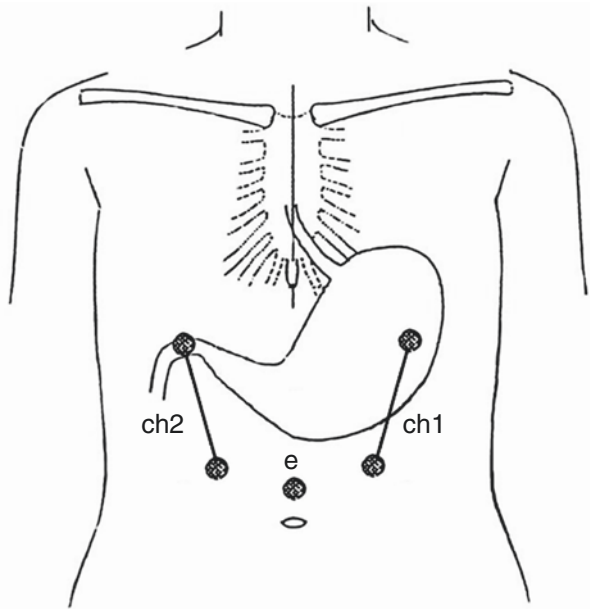

Fig. 4.1 Pasting position of EGG electrodes

to "e" was the reference electrode. We used AE to classify the EGGs before and after lunch for data of 90 min durations. The training of the AE required two channels of the EGG data recorded in the experiments and a 14-channel noise signal. The purpose of using noise signals was to extract the EGGs from the noise contaminating the actual data and to investigate whether the EGGs could be classified as pre- or post-meal records using AI. These time-series data were segmented into sequences of length 256 points and used as training and teacher data, respectively. In addition, we added the condition that the input time series should be a pre-meal or post-meal series to the teacher data, so that the number of neurons on the input side of the AE is 16×256, and the number of neurons on the output side is $16 \times 256 + 1$. Further, the latent variable dimension was set to two dimensions (Fig. 4.2).

We trained the AE 100 times and assessed the distributions of the groups with the pre-meal and post-meal time series in the latent variable space. Thereafter, the unknown data that were not used for training were evaluated in the same manner, and we checked whether these were distributed in the latent variable space. At this point, the distribution of the unknown data was classified according to its proximity to the previously identified pre-meal or post-meal distributions to assess its similarity to the previously identified distribution. From the experimental results, it was suggested that the AE could be used to classify pre- and post-prandial EGG (Fig. 4.3).

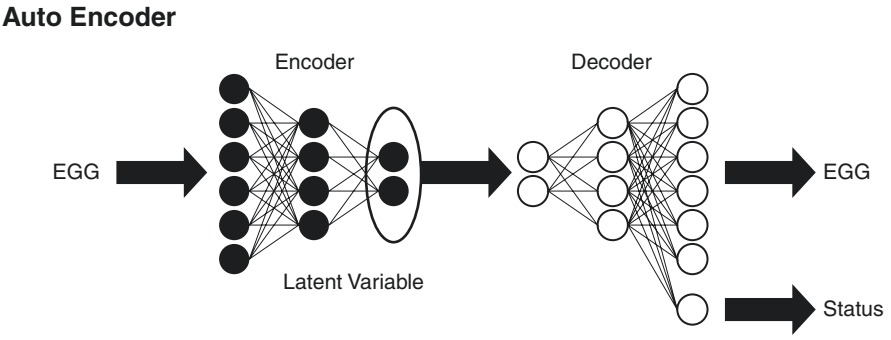

Fig. 4.2 Schematic diagram of AE

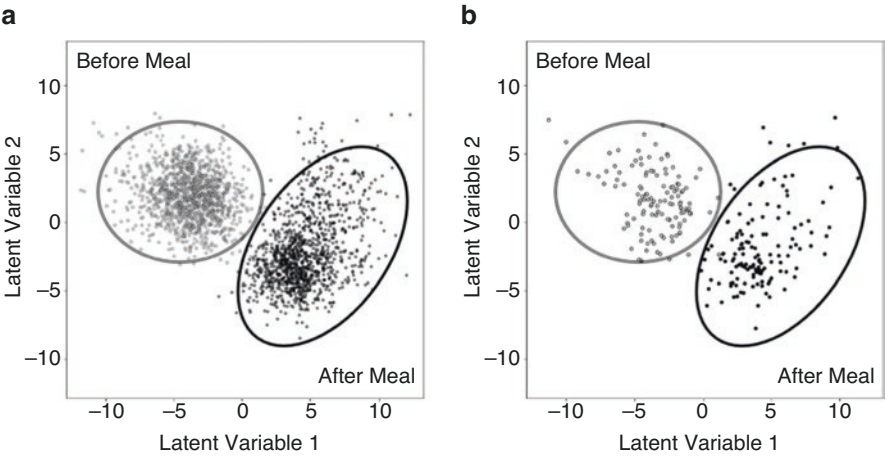

Fig. 4.3 Scatter diagram of Latent variables in Fig. 4.2; EGG Data used for machine learning (**a**), EGG Data excluding data in (**a**, **b**)

References

1. Alvarez WC. The electrogastrogram and what is shows. J Am Med Assoc. 1922;78:1116–9.
2. Cajal SR. Histologie du systeme nerveux de l'homme et des vertèbres. Paris: Maloine; 1911. (in French) (reprinted in English, Cajal SR, Swanson N, Swanson LW. Histology of the nervous system of man and vertebrates. Oxford: Oxford University Press. 1995).
3. Homma S. Isopower mapping of the electrogastogram (EGG). J Auton Nerv Syst. 1997;62:163–6.
4. Thomsen L, Robinson TL, Lee JCF, Farraway L, Hughes MJG, Andrews DW, Huizinga JD. Interstitial cells of Cajal generate a rhythmic pacemaker current. Nat Med. 1998;4:848–51.
5. Hirota S, Isozaki K, Moriyama Y, Hashimoto K, Nishida T, Ishiguro S, Kawano K, Hanada M, Kurata A, Takeda M, Muhammad TG, Matsuzawa Y, Kanakura Y, Shinomura Y, Kitamura Y. Gain-of-function mutations of c-kit in human gastrointestinal stromal tumors. Science. 1998;279(5350):577–80.

6. Nakamura E, Kito Y, Fukuta H, Yauchi Y, Hashitani H, Yamamoto Y, Suzuki H. Cellular mechanism of the generation of spontaneous activity in gastric muscle. Folia Phamacol Jpn. 2002;123(3):141–8.
7. Torihashi S. Structure and function of interstitial cells of Cajal. Pediatr Surg. 2005;37(4):467–72. (in Japanese)
8. Takayama I, Horiguchi K, Daigo Y, Mine T, Fujino MA, Ohno S. The interstitial cells of Cajal and a gastroenteric pacemaker system. Arch Histol Cytol. 2002;65(1):1–26.
9. Smout AJ, Van Der Schee EJ, Grashuis JL. What is measured in electrogastrography? Dig Dis Sci. 1980;25(3):179–87.
10. Chen JDZ, Mccallum RW. Electrogastrography: principles and applications. New York: Raven Press; 1994.
11. Pezzolla F, Riezzo G, Maselli MA, Giorgio I. Electrical activity recorded from abdominal surface after gastrectomy or colectomy in humans. Gastroenterology. 1989;97:313–20.
12. Homma S, Yagi M, Uchiyama M, Watanabe N, Iwabuchi A. Topographic of Short bowel syndrome or power electrogastroenterography. J Smooth Muscle Res. 1998;2(1):J-54. (in Japanese)
13. Kaneoke Y, Koike Y, Sakurai N, Washimi Y, Hirayama M, Hoshiyama M, Takahashi A. Electrogastroenterography. I. Analysis of methodology. Auton Nerv Syst. 1992;29:29–37. (in Japanese)
14. Ozawa S, Fukuda Y. Medical physiology. 7th ed. Tokyo: Igaku-Shoin; 2009. (in Japanese)
15. Cheung B, Vaitkus P. Perspectives of electrogastrography and motion sickness. Brain Res Bull. 1998;47(5):421–31.
16. Okuno Y, Hongo M, Ujiie H. Percutaneous recording of gastric electrical activity (electrogastrography): its technique and analysis. J Smooth Muscle Res. 1988;24(6):392–4. (in Japanese)
17. Imai K, Ishimaru K, Iwa M, Sasaki S, Sakita M. Inhibition of abdomainal acupuncture stimulation on electrogastrographic (EGG) study. Auton Nerv Syst. 1996;33(2):134–9. (in Japanese)
18. Chen JDZ, Mccallum RW. Clinical applications of electrogastrography. Am J Gastroenterol. 1993;88:1324–36.
19. Yoneda H, Ishizaki N, Imai K, Ono K, Yano T, Yamamura Y. Influence of water road test on electrogastrograms of diabetes mellitus patients. Auton Nerv Syst. 2002;39(1):80–6. (in Japanese)
20. Kenneth LK, Robert M. Handbook of electrogastrography. Oxford: Oxford University Press; 2004.
21. Sagami Y, Hongo M. Electrogastrogram. In: Clinical examination of the autonomic nervous system. 4th ed. Tokyo: Bunkodo; 2007. (in Japanese).
22. Shen H, Ichimaru Y, Kobayashi M. Development of electrogastrographic (EGG) analysis system and its application for nutritional physiology. Jpn J Physiol Anthropol. 2003;8(1):9–16. (in Japanese)
23. Naruse T, Inoue H, Inomata H. Power spectral–time analysis of electrogastrography. Proc Soc Instrum Control Eng Tohoku Chapter. 2000;189(1):1–9. (in Japanese)
24. Matsuura Y. Quantitative evaluation of electrogastrography based on nonlinear stochastic model. Doctoral dissertation, Nagoya City University, Graduate School of Natural Sciences. 2009. (in Japanese).
25. Matsuura Y, Miyao M, Takada H. Stochastic resonance as a mathematical model of an electrogastrogram. J Phys Sci Appl. 2012;2(6):186–94.
26. Tokmakçi M. Analysis of the electrogastrogram using discrete wavelet transform and statistical methods to detect gastric dysrhythmia. J Med Syst. 2007;31(4):295–302.
27. Van Der Schee EJ, Grashuis JL. Running spectrum analysis as an aid in the representation and interpretation of electrogastrographic signals. Med Biol Eng Comput. 1987;25:57–62.
28. Matsuura Y, Yokoyama K, Takada H, Iwase S, Shimada K. Frequency analysis of electrogastrography of healthy women during sleep. Trans Jpn Soc Med Biol Eng. 2007;44(4):560–6. (in Japanese)

29. Kim DW, Ryu CY, Lee SI. Usefulness of a developed four-channel EGG system with running spectrum analysis. Yonsei Med J. 2000;41(2):230–6.
30. Zhishum W, Zhenya H, Chen JZ. Blind EGG separation using ICA neural networks. In: Proceedings of the 19th Annual International Conference of the IEEE Engineering in Medicine and Biology Society, Institute of Electrical and Electronics Engineers, Piscataway. 1997. p. 1351–4.
31. Takens F. Detecting strange attractors in turbulence. Lect Notes Math. 1981;898:366–81.
32. Wayland R, Bromley D, Pickett D, Passamante A. Recognizing determinism in a time series. Phys Rev Lett. 1993;70:580–2.
33. Rosenstein MT, Collins JJ, De Luca CJ. A practical method for calculating largest Lyapunov exponents from small data sets. Physica D. 1993;65:117–34.
34. Sato S, Sano M, Sawada Y. Practical methods of measuring the generalized dimension and the largest Lyapunov exponent in high dimensional chaotic systems. Prog Theor Phys. 1987;77:1–5.
35. Lyapunov AM. The general problem of the stability of motion. Comm Soc Math: Kharkow; 1892. (in Russian) (reprinted in English, Lyapunov AM. The general problem of the stability of motion. Int J Control 1992;55:531–4).
36. Eckmann JP, Kamphorst SO, Ruelle D, Ciliberto S. Liapunov exponents from time series. Phys Rev A. 1986;34(6):4971–9.
37. Sato C. Nonlinear oscillation theory. Tokyo: Asakura Publishing; 1970. (in Japanese)
38. Matsuura Y, Takada H, Yokoyama K, Shimada K. Proposal for a new diagram to evaluate the form of the attractor reconstructed from electrogastrography. Forma. 2008;23(1):25–30.
39. Nelsen TS, Becker JC. Simulation of the electrical and mechanical gradient of the small intestine. Am J Phys. 1968;214:749–57.
40. Sarna SK, Daniel EE, Kingma YJ. Simulation of the electrical activity of the stomach by an array of relaxation oscillators. Am J Dig Dis. 1972;17:299–310.
41. Hinton GE, Salakhutdinov RR. Reducing the dimensionality of data with neural networks. Science. 2006;313(5786):504–7.

Chapter 5
Measurements for Visual Function, Including Gaze, and Electrooculography (EOG)

Kazuhiro Fujikake

Abstract Humans obtain information from their five senses, which include vision. In recent decades, numerous displays have been developed as a result of technological advancements, and such apparatuses can be used in daily life. The development of evaluation indicators for gaze data is a very important research topic in the hygiene field. In this chapter, we outline the types of eye movements, such as the saccade, smooth pursuit eye movement, vergence eye movement, optokinetic nystagmus, vestibulo-ocular reflex, and rotational eye movement. Thereafter, we introduce several methods for measuring eye movements, including the magnetic search coil method, pupil center corneal reflection method, limbus tracking meth-od, image analysis method, and electrooculography. Based on the eye movements measured by noncontact devices, indices are developed to evaluate the severity of visually induced motion sickness.

Keywords Eye movements · Rotational eye movement · Visually induced motion sickness (VIMS) · Driving simulator (DS)

5.1 Introduction

With the development of information technology, the accuracy and performance of measurement instruments for biological signals have improved, and new analysis methods have been presented [1]. Such measurement instruments are used extensively in research and medical settings. For example, techniques such as electroencephalography, functional MRI, and near-infrared spectroscopy (NIRS) are used in the field of brain physiology [2–4]. Electrocardiograms (ECGs) and electrogastrograms (EGGs), which measure action potentials in the body, are also carried out

K. Fujikake (✉)
School of psychology, Chukyo University, Showa-ku, Nagoya, Japan
e-mail: fujikake@lets.chukyo-u.ac.jp

H. Takada, K. Yokoyama (eds.), *Bio-information for Hygiene*, Current Topics in Environmental Health and Preventive Medicine,
https://doi.org/10.1007/978-981-15-2160-7_5

using specialized equipment [5, 6]. Moreover, eye movements are an important type of biological signal data [7].

The eye perceives light energy from the outside world through the photoreceptors of the retina. The received information is transmitted through the nervous system to the brain center, where it is perceived as vision. Two types of photoreceptor cells exist in the retina: rods and cones. The rods are a function of high sensitivity to light and operate while observing objects in the dark. The cones operate in bright areas and respond selectively to different light wavelengths. The three types of human cone cells are classified as the L-cone, M-cone, and S-cone, based on the longer light wavelengths that they absorb. Furthermore, an area of concentration of cones exists, which is known as the central fossa. Therefore, for a human to obtain a clear view of an object, the object must be captured in the central fossa. Six external eye muscles, namely the external rectus, internal rectus, superior rectus, inferior rectus, inferior oblique, and superior oblique, move the eye to capture an object in the central fossa. Thus, eye movements occur based on the structure and function of the eye [8, 9].

The human gaze is controlled by the action of the external eye muscles that move the eye. In this chapter, we outline the types of eye movements. Moreover, we introduce several methods for measuring eye movements.

5.2 Types of Eye Movements

Eye movements can be categorized as saccade (saccadic eye movement), smooth pursuit eye movement, vergence (convergence and divergence) eye movement, optokinetic nystagmus (OKN), vestibulo-ocular reflex (VOR), and rotational eye movement [8, 9].

5.2.1 Saccade (Saccadic Eye Movement)

The saccade is a rapid eye movement, whereby the maximum velocity increases with the amplitude (amplitude: 0.5°–40°, speed: 30–700°/s) [10, 11]. A saccade cannot be intentionally stopped once the exercise begins. In general, the saccade stops slightly ahead of the target, and in such cases, a small saccade (corrective saccade) will eventually bring it to a halt at the target position. Furthermore, saccades require an interval of at least 200 ms if they occur consecutively, and no visual information is entered during the saccade.

5.2.2 Smooth Pursuit Eye Movement

Smooth pursuit eye movement is a smooth, gradual conjugate eye movement that captures and follows the target in the central fossa. Smooth pursuit eye movement is prominent in primates with developed fovea centralis, such as humans and monkeys. In humans, the eye can be moved smoothly up to approximately 50°/s. A visual object is constantly required for smooth pursuit eye movement to occur and the ratio (gain) of the eye velocity to the visual object velocity is 0.7–0.9 in humans. Moreover, the correction of the position is adjusted for saccades.

5.2.3 Vergence (Convergence and Divergence) Eye Movement

Convergence is a condition in which the left and right eyes move close together, as when looking at a nearby object. Convergence is a reflexive and voluntary movement. Divergence is shifting the point of the gaze from near to far. The reaction time of convergence/divergence eye movements is 160 ms and the maximum speed is 20°/s, which is slower than the other eye movements.

Convergence/divergence eye movements differ from other eye movements in that the movements of both eyes exhibit an opposite directional component. When gazing at near and distant objects, parallax occurs in both limits. The fused convergence eye movements attempt to eliminate the retinal shift of the gazing point. In contrast, another mechanism allows the retinal misalignment (parallax) outside the gaze point to be fused by processing in the brain. In general, the latter function is a major factor in stereopsis, whereas accuracy is not significantly involved in depth perception.

5.2.4 OKN

One of the eye movements that fixates a moving visual target on the retina is the OKN. VOR also has a similar function of stabilizing the moving visual object on the retina. However, OKN fine-tunes the slip, which the VOR fails to compensate. The two components of the OKN eye movement are rapid and slow responses; the tracking of a moving visual target is typically achieved by a combination of slow and rapid movements [12].

5.2.5 VOR

The VOR is an eye movement that automatically compensates for the change in the gaze direction when the head is rotated without tilting. Head and eye movements are linked to one another while observing an object, and the eyes can remain fixed on the object. The VOR also occurs while the eye is closed, but with a smaller amount of eye movement.

The VOR is controlled by a head movement sensor known as the semicircular canal in the ear and by a neural pathway known as the vestibule that controls the sense of balance. Moreover, signals from sensors that detect the stretching of muscles in the neck and other parts of the body affect eye movement. The VOR is a reflex mechanism for rotational stimuli because the reflexes associated with the rotation of the head and body occur in response to input from the semicircular canals. When the head is tilted to the left or right, rotational eye movement occurs.

5.2.6 Rotational Eye Movement

Rotational eye movement is the movement of the eye as it rotates around a gaze axis. It is generated by two types of stimuli: those from the vestibule (especially the otolithic organ) and visual stimuli.

Rotational eye movements that are generated by vestibular stimulation are referred to as vestibular counter-rolling (vestibular torsional counter-rolling). When the body (head) is tilted in either direction, the eyeball rotates in the opposite direction to that of the body (head) tilt, thereby preserving the vision [13].

Rotational eye movements are also a reflection of linear acceleration from the otolithic organ.

It has been suggested that ocular torsional counter-rolling occurs in motion sickness, whereas a postural wobble occurs as a physical symptom of motion sickness [14].

5.3 Measurement of Eye Movement

The modern scientific observation and measurement of eye movements are believed to have started with Muller [15, 16]. The two methods used at the time were the direct observation method, which allowed the naked eye to observe the iris pattern in the cornea (black eye) and the movement of capillaries on the sclera (white eye), and the after-image method, which quantitatively measured the movement of the after-image generated on the retina by projecting it onto a screen. Subsequently, Huey covered the eye up to the sclera with a plaster contact and used a technique

that mechanically magnified the movement of the bar connected to the contact by using a lever and recorded the movement on paper [17].

At present, methods used to measure eye movements include the magnetic search coil method, pupil center corneal reflection (PCCR) method, limbus tracking method, image analysis method, and electrooculography (EOG). In this section, we introduce these methods and the related research.

5.3.1 Magnetic Search Coil Method

In the magnetic search coil method, an external magnetic field is created, a contact lens-shaped coil is placed in close contact with the eye (usually the sclera), and the eye movement is measured as the potential induced by the coil [18, 19]. Therefore, it offers high accuracy and a wide measurement range. Furthermore, it exhibits the ability to measure the eye rotation motion [20, 21].

The magnetic search coil method is used in the diagnosis and measurement of pathological nystagmus owing to its high accuracy. For example, it is known that congenital nystagmus is a common cause of nystagmus in children and that the nystagmus diminishes over the natural course of time. The magnetic search coil method has been used to inspect nystagmus with high accuracy [22, 23]. In recent years, the magnetic search coil method has been used in virtual reality (VR) and augmented reality (AR) scenarios. VR and AR are used for eye tracking using wearables, headsets, and other devices. Many of these techniques rely on optical tracking, with an accuracy of approximately 0.5°–1°. In contrast, devices for VR and AR using the magnetic search coil method can estimate the orientation of the eyes with an average accuracy of 0.094° [24].

5.3.2 PCCR Method

In PCCR, a light source is shone onto the cornea to identify the light reflection point and pupil on the cornea, and the eye direction is calculated based on the light reflection point and other geometric features [7, 25, 26]. The PCCR method has been used for a long time owing to its large amount of reflected light, and it remains the most widely used method. In principle, when the cornea is irradiated by a light source, four reflection images (the first to fourth Purkinje images) appear. These images are reflected at the anterior surface of the cornea, posterior surface of the cornea, anterior surface of the lens, and posterior surface of the lens. Among these, the reflectivity of the anterior surface of the cornea is large, at approximately 2.4%, making it the brightest reflection image. Compared to the reflected image on the anterior surface of the cornea, the other reflected images are darker and therefore negligible in the measurement of eye movement. Furthermore, a “glint-free” method that does not use these Purkinje images has been proposed, but it is not yet at the practical

stage [27]. In recent years, instruments that are capable of capturing a wide range of corneal reflections have been developed to study the limiting points of corneal reflections and to derive the movement range of the camera and light source to capture the cornea [28], which is expected to expand the use of the system further.

5.3.3 Limbus Tracking Method

The limbus tracking method is a technique in which a light source is irradiated on the cornea (black eye) and sclera (white eye), and the eye movement is detected based on the difference in reflectivity between the two [7, 29].

The limbus is the boundary between the cornea and sclera. The reflectivity from the cornea and sclera is significantly greater than the reflectivity from the sclera. When infrared light is shone near the limbus, the amount of reflected light also changes as the ratio of the area covered by the cornea to that covered by the sclera changes owing to the movement of the eyeball. The eye movement is detected by the Limbus tracking method according to the amount of change.

The limbus tracking method uses infrared light instead of visible light to avoid glare for the subject. The infrared light is irradiated below the center of the cornea and the amount of reflected light is measured. Therefore, the limbus tracking method mainly focuses on horizontal eye movements, and it can also measure rapid movements such as saccades.

A study using the limbus tracking method assessed the level of arousal based on the measurement of eye movements of reading horizontal text strings [30]. The results of this study are expected to be developed for the assessment of driver arousal levels in automated driving. Research has also been conducted on security systems using eye gaze measurement technology [31].

5.3.4 Image Analysis Method

The accuracy of image analysis has improved dramatically with the development of technologies and methods relating to data science. The image analysis technique is also commonly used to measure eye movements by capturing a photograph of the eye and analyzing the image with a computer [32, 33].

The most convenient image analysis method is detecting and recording the center position of the pupil. Because the pupil area is dark, and only needs to be binarized by the thresholding and calculation of the center of gravity coordinates, it is also possible to measure the eye movements in real time. Moreover, if the center of the pupil and corneal reflection image are analyzed simultaneously, it is possible to cancel the movement of the head. Previous studies have measured the ocular rotational movements by including the pattern of photophores in the acquisition data [34].

5.3.5 EOG

EOG is a method for recording the electrical phenomena related to eye movements. The eye is positively charged on the corneal side and negatively charged on the retinal side. In EOG, the potential difference between the cornea and retina is measured by stretching electrodes around the eye [35, 36].

People with disabilities, particularly total paralysis, are often unable to use biological communication channels such as voice and gestures, resulting in the need for digital communication channels. These methods for assisting people include the acquisition of eye movement and gaze data by EOG, and communication by inputting information to information devices [37]. Certain studies have specifically addressed the real-time measurement of cancer through uvula motion and gaze data by EOG [38, 39].

5.4 Development of an Index for Evaluating VIMS Using Gaze Data

In the following sections, we introduce studies on the development of an evaluation index for visually induced motion sickness (VIMS) using eye gaze data.

VIMS is considered as a type of agitation illness that is thought to be caused by the disharmony between visual information and the vestibular system, such as the tricuspid canal. Therefore, the eye movement control system is expected to be involved. The physical symptoms of VIMS include feeling unwell, nausea (upset stomach), dizziness, and vertigo when standing up. The indices used to evaluate VIMS are the results of simulator sickness questionnaires (SSQs), which are the main evaluation method, and measurements of the gravity center sway of the participants while standing [40, 41]. It is also known that if motion sickness causes unsteadiness, rotational eye movement will occur in the direction opposite to the unsteadiness, so that the individual's eyes do not tilt the field of view [14]. This rotational eye movement can be used as a physiological index of VIMS, and evaluations have been carried out based on electromyographic data from near the eyes. Furthermore, a method for evaluating nausea based on EGG measurements is currently being studied as a new physiological index. However, studies using physiological indices have not obtained consistent results for the complex changes that occur with the progression of motion sickness. As electrodes must be attached to test participants and specialized equipment must be used to obtain electromyograms or EGGs, these options are only feasible in limited circumstances. Although SSQ-based introspective reports permit evaluations with a considerable amount of liberty, in certain cases where the symptoms of VIMS have progressed to the point of subjective assessment, such symptoms persisted for approximately a week.

5.4.1 VIMS in Driving Simulator

With the increasing number of elderly drivers on roads, the prevention of accidents involving elderly drivers has become a serious challenge. Research on elderly drivers includes studies on their visual and cognitive functions as well as their driving characteristics to help them to drive more safely. While research on elderly drivers primarily involves actual vehicles on ordinary roads, several studies using driving simulators (DSs) exist. The merits of experiments using DSs include a low risk of accidents or other operational problems, easy setting and reproduction of specific conditions and situations, and the ability to adjust the experimental conditions. In contrast, the demerits of using DSs include the occurrence of VIMS, lack of a sense of reality, and high cost. In recent years, the performance of DS hardware has improved and its cost has decreased; thus, the reality and cost problems are gradually being resolved, but an effective VIMS prevention measure has not yet been developed. Inversely, as the field of view expands, the symptoms of VIMS are intensified. Therefore, as display screens become larger, the risk of VIMS may also increase. When a DS experiment is performed, it is necessary to detect VIMS precursors promptly before the symptoms become severe.

The use of a noncontact eye-tracking system is considered a low burden method for measuring biological signals. The goal of this study was to develop a VIMS evaluation index that uses a noncontact eye-tracking system for DS experiments.

As rotational eye movement is caused by unsteadiness resulting from VIMS, the following hypotheses are presented.

Hypothesis 1: VIMS symptoms occur; the locus of the eye-tracking data lengthens.
Hypothesis 2: VIMS symptoms occur; the eye-tracking data are diffused.

The participants were nine elderly people who had visual and balance functions that did not interfere with their daily life. The gaze data were measured at rest before and after DS driving (5 min of driving, 5 trials). The resting gaze data were obtained by the participants gazing at the center of the DS screen for 1 min during the measurement. SSQs were conducted before and after the start and end of the experiment.

The instrument used for measuring the gaze data and the analysis software were the Tobii Pro X2–30 (sampling rate: 60 Hz) and Tobii Pro Studio (ver. 3.3.2), respectively. The gaze data were plotted corresponding to the resolution (640 × 480 pixels) of the scene camera (Logitech HD Webcam C270).

The participants were divided into two groups based on the SSQ results. One group experienced VIMS during the DS driving (4 people, average of 79.0 years old). The other group did not experience VIMS during the DS driving (5 people, average of 71.2 years old).

5.4.2 *Evaluation of VIMS Using Gaze Data*

Figure 5.1 presents the calculation results of the total locus length for each participant based on the eye-tracking data at rest to determine the average for each case of "no previous or previous experience" of VIMS before and after (pre-/post-) DS driving. The total locus length results indicate that, for both the pre-DS and post-DS driving, the total locus length data were longer for those with than for those without previous experience of VIMS. Furthermore, among those without previous experience, no difference was observed between the total locus lengths of the pre-DS and post-DS driving. However, among those with previous experience, the total locus length tended to be longer for the post-DS driving ($p < 0.1$).

Similar to the total locus length, the sparse density was calculated based on the eye-tracking data to obtain the average for each set of experimental conditions, as illustrated in Fig. 5.2. The sparse density is a quantification index that is represented by a scatterplot of the data on a plane, and the diffusion of the data increases its value. In the sparse density results, the post-trial value was higher than the pre-trial value for both the participants with and without experience of VIMS. Among those without any experience of VIMS, no difference was observed in the sparse density between the pre-DS and post-DS driving results. Among those with previous experience of VIMS, the sparse density value was significantly higher after the DS driving ($p < 0.05$).

The two hypotheses concerning the results of VIMS symptoms were confirmed: the loci of the eye-tracking data were lengthened and the eye-tracking data were

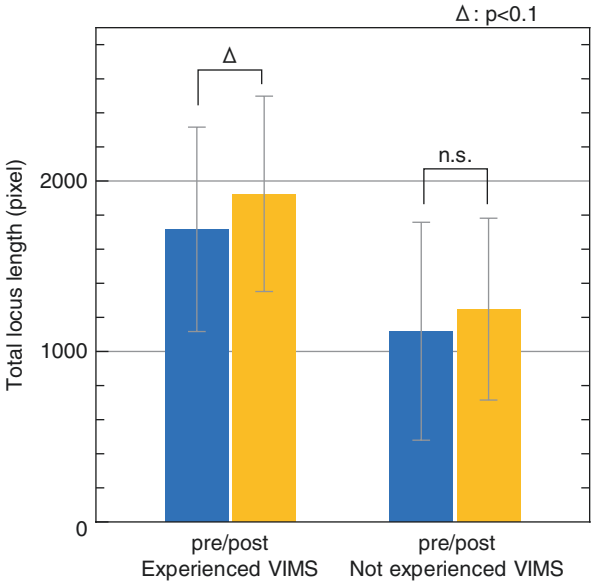

Fig. 5.1 Total locus length of gaze

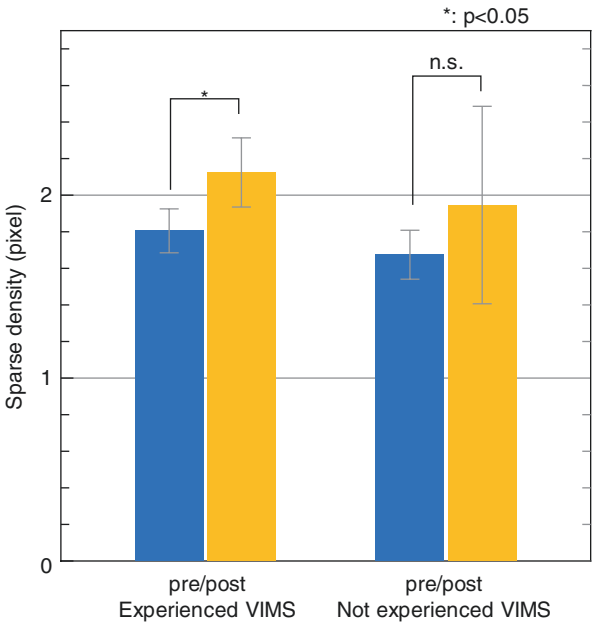

Fig. 5.2 Sparse density of gaze

diffused. Moreover, the experiments demonstrated the usefulness of sparse density as a quantification index for eye-tracking data in evaluating VIMS (Fig. 5.2).

The results of the total locus length in the eye-tracking data revealed that the locus was longer after the DS driving in the group with previous VIMS experience, suggesting that among elderly people who are susceptible to VIMS, the unsteadiness of the line of vision may have been normalized.

Regarding the application of the findings of this study, it is believed that if an eye-tracking data-based VIMS evaluation index can be used, it will be easier to detect VIMS caused by DS operations, thereby permitting detection of the symptoms while they are still at the developmental stage. Furthermore, by coding the VIMS evaluation index algorithm into a program, it will be possible to develop a real-time automatic VIMS detection system to help to reduce the load on participants after viewing stereoscopic motion images or while wearing head-mounted display devices. Moreover, the findings will not be limited to VIMS; they can also be applied to the treatment of disorders relating to rotational eye movements (nystagmus).

5.5 Conclusions

The prevention of VIMS and the treatment of nystagmus disorders are important topics in the field of hygiene. In this chapter, we have outlined the types of eye movements and have introduced several methods for measuring eye movements.

The use of gaze data is a highly effective method for acquiring biological signals. In the next step, gaze data are expected to be used for evaluating the performance of new human–machine interface devices as in VR and AR.

References

1. Tanimura T, Jono Y, Hirata T, Matsuura Y, Takada H. Trial on low-pass filter design for biosignal based on nonlinear analysis. Forma. 2019;34(1):13–20.
2. Takada H, Miyao M, Takada M, Kinoshita F, Tahara H. Development of sports vision training system using virtual reality for prevention of mild cognitive impairment. Descente Sports Sci. 2019;40:97–109. Japanese
3. Bohning DE, Shastri A, Wassermann EM, Ziemann U, Lorberbaum JP, Nahas Z, Lomarev MP, George MS. BOLD-fMRI response to single-pulse transcranial magnetic stimulation (TMS). J Magn Reson Imaging. 2000;11:569–74.
4. Tanimura T, Takada H, Sugiura A, Kinoshita F, Takada M. Effects of the low-resolution 3D video clip on cerebrum blood flow dynamics. Adv Sci Technol Eng Syst J. 2019;4(2):380–6.
5. Mincholé A, Rodriguez B. Artificial intelligence for the electrocardiogram. Nat Med. 2019;25:22–3.
6. Kinoshita F, Fujita K, Miyanaga K, Touyama H, Takada M, Takada H. Analysis of electrogastrograms during exercise loads. J Sports Med Doping Stud. 2018;8(2):285–94.
7. Young LR, Sheena D. Methods and designs: survey of eye movement recording methods. Behav Res Methods Instrum. 1975;7:397–429.
8. Leigh RJ, Zee DS. The neurology of eye movements. New York: Oxford University; 2015.
9. Klein C, Ettinger U, editors. Eye movement research. Cham: Springer; 2019.
10. Javal LE. Essai sur la physiologie de la lecture. Ann Ocul. 1878;79:97–117.
11. Landolt E. Nouvelles recherches sur la physiologie des mouvements des yeux. Arch Ophthalmol. 1891;11:385–95.
12. Berthoz A, Melvill-Jones G. Adaptive mechanisms in gaze control. Amsterdam: Elsevier; 1985.
13. Howard IP. Human visual orientation. Chichester: Wiley; 1982.
14. Hoshino K, Ono N, Tomida M, Igo N. Measurement of rotational eye movement with blue light irradiation. In: Proceedings of the 3rd International Conference on Biomedical and Bioinformatics Engineering. 2017. p. 50–4.
15. Mueller J. Zur vergleichenden physiologie des gesichtssinnes des menschen und der thiere. Leipzig: Cnobloch; 1826.
16. Mueller J. Handbuch der Physiologie des Menschen. Coblenz: Verlag von Hoelscher; 1840.
17. Huey EB. Preliminary experiments in the physiology of reading. Am J Psychol. 1898;9(4):575–86.
18. Robinson DA. A method of measuring eye movement using a scleral search coil in a magnetic field. IEEE Trans Bio-Med Electron. 1963;BME-10:137–45.
19. Fuchs AF, Robinson DA. A method for measuring horizontal and vertical eye movements chronically in the monkey. J Appl Physiol. 1966;21:1068–70.
20. Remmel RS. An inexpensive eye movement monitor using the scleral search coil technique. IEEE Trans Biomed Eng. 1984;31:388–90.
21. de Bie J. An afterimage vernier method for assessing the precision of eye movement monitors: results for the scleral coil technique. Vis Res. 1985;25:1341–3.
22. von Noorden GK, Campos EC. Binocular vision and ocular motility. 6th ed. St Louis: Mosby; 2002. p. 477–80.
23. Zahn JR. Incidence and characteristics of voluntary nystagmus. J Neurol. 1978;41:617–23.

24. Whitmire E, Trutoiu L, Cavin R, Perek D, Scally B, Phillips J, Patel S, Patel S. EyeContact: scleral coil eye tracking for virtual reality. In: Proceedings of the 2016 ACM International Symposium on Wearable Computers. 2016. p. 184–91.
25. Cornsweet TN, Crane HD. Accurate two-dimensional eye tracker using first and fourth Purkinje images. J Opt Soc Am. 1973;63:921–8.
26. Crane HD, Steele CM. An accurate three-dimensional eye tracker. Appl Opt. 1978;17:691–705.
27. Dierkes K, Kassner M, Bulling A. A novel approach to single camera, glint-free 3D eye model fitting including corneal refraction. In: Proceedings of the 2018 ACM Symposium on Eye Tracking Research & Applications (ETRA '18). 2018. Article no. 9. p. 9.
28. Yamamoto M, Matsuo R, Fukumori S, Nagamatsu S. Modeling corneal reflection for eye-tracking considering eyelid occlusion. In: Proceedings of the 2018 ACM Symposium on Eye Tracking Research & Applications (ETRA '18). 2018. Article no. 95. p. 3.
29. Wen-Chung K, Yi-Chin C. Hierarchical search of optimal limbus circle matching for gaze tracking systems. In: 2017 IEEE 7th International Conference on Consumer Electronics—Berlin (ICCE-Berlin). 2017. p. 233–234.
30. Nirmalee D, Ranathunga L. Reader text highlighter based on gaze tracking and finite state machine. In: 2018 18th International Conference on Advances in ICT for Emerging Regions (ICTer). 2018. https://doi.org/10.1109/ICTER.2018.8615520.
31. Hameed S, Ahmed IS. Security systems based on eye movement tracking methods. JQCM. 2018;10:70–8.
32. Yamanobe S, Taira S, Morizono T, Yagi T, Kamio T. Eye movement analysis system using computerized image recognition. Arch Otolaryngol Head Neck Surg. 1990;116:338–41.
33. Imai T, Sekine K, Hattori K, Takeda N, Koizuka I, Nakamura K, Miura K, Fujioka H, Kubo T. Comparing the accuracy of video-oculography and the scleral search coil system in human eye movement analysis. Auris Nasus Larynx. 2005;32:3–9.
34. Hatamian M, Anderson DJ. Design considerations for a real time ocular counter roll instrument. IEEE Trans Biomed Eng. 1983;30:278–88.
35. Marg E. Development of electro-oculography; standing potential of the eye in registration of eye movement. AMA Arch Ophthalmol. 1951;45:169–85.
36. Shackel B. Eye movement recording by electro-oculography. In: Venables PH, Martion I, editors. A manual of psychophysiological methods. Amsterdam: North-Holland; 1967. p. 300–34.
37. Ramkumar S, Kumar KS, Rajkumar TD, Ilayaraja M, Shankar K. A review-classification of electrooculogram based human computer interfaces. Biomed Res. 2018;29(6):1078–84.
38. Lee K, Chang W, Kim S, Im C. Real-time "eye-writing" recognition using electrooculogram. IEEE Trans Neural Syst Rehabil Eng. 2017;25(1):37–48.
39. Chang W, Cha H, Kim DY, Kim SH, Im C. Development of an electrooculogram-based eye-computer interface for communication of individuals with amyotrophic lateral sclerosis. J Neuroeng Rehabil. 2017;14:89.
40. Golding JF. Phasic skin conductance activity and motion sickness. Aviat Space Environ Med. 1992;63(3):165–71.
41. Wan H, Hu S, Wang J. Correlation of phasic and motion sickness-conductance responses with severity of motion sickness induced by viewing an optokinetic rotating drum. Percept Mot Skills. 2003;97(3):1051–7.

Chapter 6
Electroencephalography (EEG): EEG as a Tool to Improve QOL and Maintain Healthy Brain

Ryohei P. Hasegawa

Abstract This chapter reviews the recent progress in EEG technologies. We focused on EEG-based brain–machine/computer interfaces, especially the use of the event-related potential (ERP) as a Mind Switch for communication aid as well as cognitive assessment/training.

Keywords Brain–Machine/Computer Interface · Event-related potential Communication aid · Cognitive assessment · Cognitive training

6.1 Introduction

Recently, there has been a worldwide interest in the development of neurotechnology. One of the representative fields of study is the brain–machine/computer interface (BMI/BCI), a device that translates neuronal information into commands capable of controlling external devices. With the use of BMI, telepathy and psychokinesis are no longer science fiction at this date.

The big movement in BMI research was triggered by advancements in invasive BMI that controlled prosthetic devices such as robot arms by the signals from the multielectrode arrays inside the brain [1, 2]. Non-invasive BMIs, on the other hand, are expected to accelerate the practical implications of BMI [3]. The most typical non-invasive BMI uses scalp electroencephalography (EEG). Although EEG-based BMIs widely share the accumulated knowledge and experience from basic and clinical studies, they also import new ideas and technologies from developing fields

R. P. Hasegawa (✉)
Department of HIIRI, AIST, Tsukuba, Ibaraki 305-8560, Japan
e-mail: r-hasegawa@aist.go.jp

H. Takada, K. Yokoyama (eds.), *Bio-information for Hygiene*, Current Topics in Environmental Health and Preventive Medicine,
https://doi.org/10.1007/978-981-15-2160-7_6

such as AI, robot technologies, and IoT. Here, we discuss the effectiveness of implementing EEG-based BMIs to address current social problems.

6.2 Social Problems

One of the implementations of EEG-based BMI is a device for patients in need of communication aid. People with motor dysfunctions have difficulty not only in activities of daily living but also in conveying their thoughts through words and gestures (Fig. 6.1). Cerebrovascular diseases (Strokes), traumatic brain/neck injuries, and motor neuron diseases are the main causes of most motor disorders. If the dysfunction of the patient is severe and specific to motor function, they can be in the locked-in syndrome, or locked-in state (LS).

LS is a catastrophic condition, in which a patient is conscious but cannot communicate due to paralysis of voluntary muscles [4]. In some cases, LS patients with brainstem injury can barely communicate through eye movements and blinking, but most have no such abilities. Therefore, LS patients are often misdiagnosed as coma or vegetative.

Such an example was well described in the autobiography "Ghost Boy: The Miraculous Escape of a Misdiagnosed Boy Trapped Inside His Own Body" by Martin Pistorius. The author was diagnosed as vegetative at the age of 12, and doctors and his parents thought he was totally unconscious for years. But in fact, for 13 long years, he was in the LS; he was conscious, unable to let the outside world

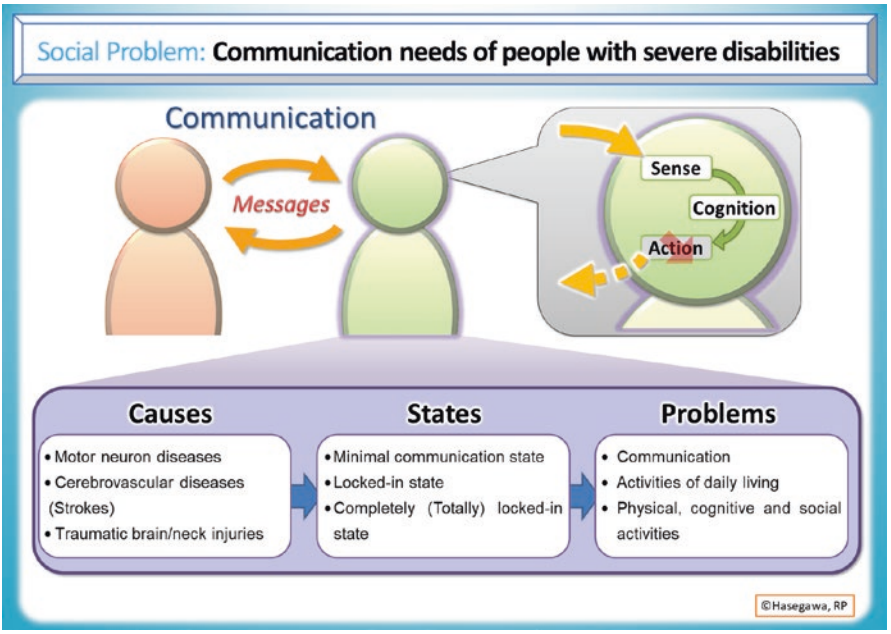

Fig. 6.1 Communication needs of people with severe disabilities

know that he was actually there. In his TED talk, he says "people abused me physically, verbally and sexually… My mother turned to me and told me that I should die." Such cases like Martin's are nothing so rare. As a matter of fact, some studies even show that up to 43% of patients diagnosed as vegetative were reassessed as having a certain level of consciousness [5]. The critical problem lies in the methodology of the current diagnosis that is dependent on the subject's motor ability.

Owen and his coworkers have been focusing on patients who have been diagnosed as vegetative or minimally conscious. They used functional magnetic resonance imaging (fMRI) to monitor the brain activity of these patients in order to examine the activity patterns of imagination [6, 7]. The patients were tested on their capability to answer yes-or-no questions by imagining playing tennis for yes, navigating the house for no. In addition, Owen's group has extended their fMRI methods to EEG, in which motor imagery was shown by reductions in the power of μ (about 7–13 Hz) or β (about 13–30 Hz) frequency bands over topographically appropriate areas of the motor cortex [8].

Motor neuron diseases, such as amyotrophic lateral sclerosis (ALS), are a group of progressive neurological disorders that selectively degenerate motor neurons in the brain and/or spinal cord. Patients of these diseases also require communication aid, as they often develop the totally locked-in state (TLS) after the minimal communication state (MCS) [9, 10].

Augmentative and alternative communication (AAC) has been implemented mainly with MCS patients for decades. A typical example of AAC is an analog communication board that consists of letters, words, phrases, and pictograms. Patients without verbal communication skills use this by physically pointing to one of the desired options on the board. On the other hand, recent computer-based communication boards allow severer patients with less motor ability to use a single button switch to satisfy the same purpose. Although these AACs offer an effective communication tool for MCS patients to socially interact with the community, they are not available for some patients. TLS patients need a totally body-free technology, where a switch can be elicited just by thinking. This is where the BMI technology we call the "Mind Switch" comes in handy.

6.3 Communication Aid by the EEG

The concept of the Mind Switch is a BMI communication tool for TLS patients. This device should allow the user to control a high-tech communication board in the auto-scanning mode, just by intention in their brain. EEG is an effective neural signal for the use in noninvasive BMI (Fig. 6.2). Although oscillatory EEG activity (basic rhythms) is widely used in clinical and academic fields, we focused on a time-locked EEG activity called event-related potential (ERP) [11] as the Mind Switch.

ERP is a small potential change in the scalp that can be recorded using EEG. This phenomenon appears aligned to the onset of an event such as a sensory stimulus or a motor act. ERPs reflect cognitive processes, especially a temporal change in

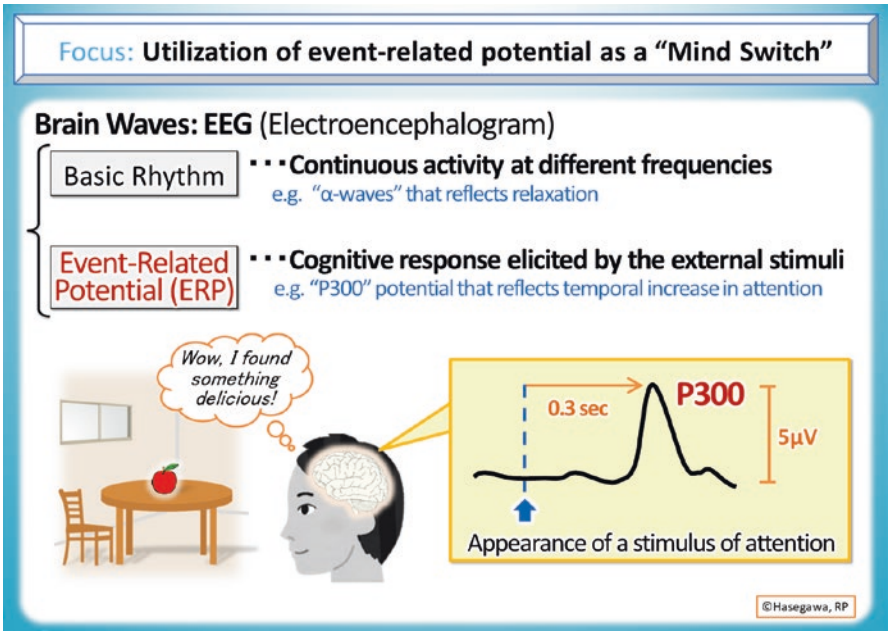

Fig. 6.2 Mind Switch enables locked-in patients to respond to others

attention. This means that the Mind Switch can be intentionally be "pushed" by using ERP to operate the AAC system.

One of the most famous examples of BMI systems using ERP is the "P300 speller" [12, 13]. The P300 speller is a virtual typewriter that uses the cognitive component of the ERP called P300 [14], derived from characters that flash randomly in a matrix of 6×6 filled with letters and commands. When the corresponding row or column with the target cell is highlighted, a P300 signal will be elicited. The original study with healthy volunteers suggested that subjects can communicate at the speed of 12.0 bits (2.3 characters per minute).

So far, many studies using a variety of experimental and analytical methods have been conducted to improve the performance of the system. Patient studies have also been conducted with ERP-based BMI [15–23]. However, it is difficult for such systems to leap out of the lab [24, 25], and the potential end-users and their families cannot benefit from the systems in their daily life.

6.4 Development of the Neurocommunicator

Recently the author and the colleagues have extended the techniques not only of the P300 speller but also our analytical methods in neurophysiology [26–28] to develop the "Neurocommunicator®" (NC), which was designated to become a practical BMI system (press released at 2010/03/29) (Fig. 6.3) [29]. The users focus on one of the

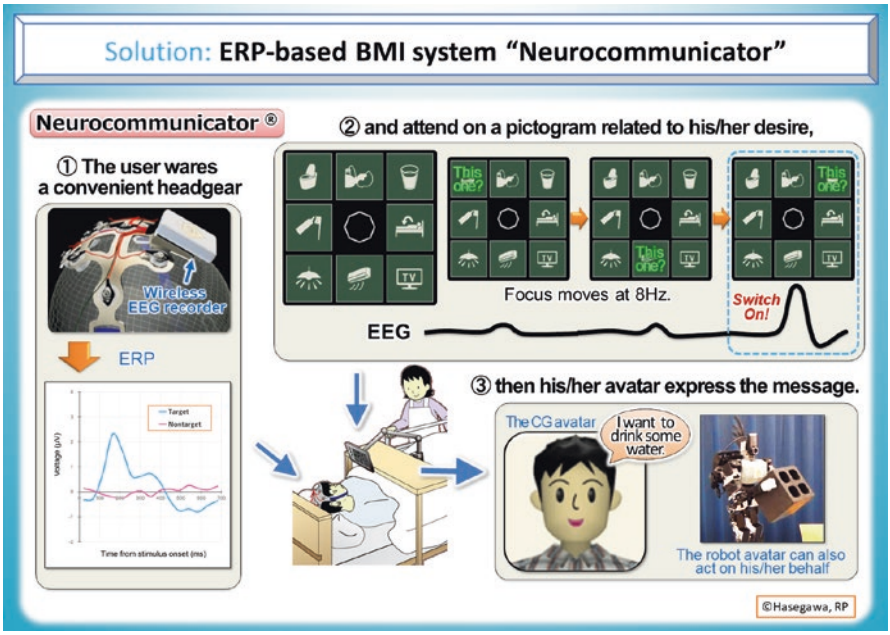

Fig. 6.3 ERP-based BMI, "Neurocommunicator" that uses Mind Switch

eight pictograms (simplified drawings of medical, nursing care, etc.) in a 3 × 3 matrices (excluding the center) on a monitor. After the system starts, each pictogram is flashed at 8 Hz, displaying four Japanese characters (e.g., "Ko-Re-Ka-Na"), which means "This one?" in English. An ERP response will be observed when the user intentionally reacts to the flashed target in their mind. After some repetitions, the target pictogram will be decoded from the EEG data.

The chosen message is friendly and clearly conveyed by the animated CG avatar, which can be selected from several types depending on the generation and the gender of the user. Although the traditional AAC system expresses the message only by artificial voice, we believe that the CG avatar has a positive effect on reminding the existence of the personality and dignity of the MCS and TLS patients. We have extended the system so that a small humanoid robot can express the message by its dynamic gesture and artificial voice [30]. The robot avatar can also work, on behalf of the users, for using tools for example.

There are three core technologies that highlight the NC: (a) "Neurorecorder", (b) "Virtual Decision Function," and (c) "Hierarchical Message Generation System." The details are as follows:

(a) *Neurorecorder* is one of the basic hardware of the NC to obtain the EEG data. The Neurorecorder consists of a custom-made plastic headgear, a small EEG amplifier attached to the headgear, the electrodes connected with the amplifier via lead cables, and the shield cover to remove electrical noise. The headgear localizes the electrode positions around the top of the head; eight signal electrodes (ID1@FC1, ID2@FC2, ID3@C3, ID4@Cz, ID5@C4, ID6@CP1,

ID7@CP2, and ID8@Pz) and one earth (ground) electrode (@CPz) were selected in the 10% (10–10) system (Refs). A common reference electrode is positioned on a neutral point (earlobe). While conductive gels are used for the eight signal electrodes (special structure patented in Japan) and the earth electrode, a disposable electrode with solid gel is used for the reference. It usually takes about 5 min to set the system to start recording, and another 5 min for calibration.

(b) *Virtual Decision Function* (VDF) is a basic analytical method of the NC for high-speed and high-accuracy decoding. The VDF was originally designed to reflect the continuous progress of binary decisions on a single trial basis of neuronal activities of the superior colliculus in the primate brain [26–28]. We have applied the VDF to the EEG signals to develop a high-speed version of the Neurocommunicator with the same level of accuracy. The VDF scores were obtained by multiplication of the success rate in the training/calibration session and the accumulative linear discriminant analysis scores in each block of the test (real-time) session. The pictogram with the VDF score that first reached the threshold is regarded as the target (user's choice). The advantage of this method is to end the session early by flashing the minimum number of pictograms.

(c) *Hierarchical Message Generation System* is an example of applications for the NC. This system enables the user to convey various messages quickly. Although the number of pictograms for the single choice is restricted to eight, the user can choose as many as 512 pictograms by three consecutive selections. First, the user selects the big categories of the messages they want to convey. Second, the user selects small categories of the messages under the selected big category. Finally, the user selects the concrete message under the selected small category. We are recently attempting to facilitate this process by introducing an AI system. By letting the AI narrow down possible choices of pictograms from the recognition of questions given by the caretakers or family members, this Hierarchical Message Generation System could become more efficient.

When conducting evaluation tests for the NC, we sometimes encountered cases where the ERP response was too weak for detection, especially when the subjects (mainly ALS patients) were either elderly or long-term bedridden. As previous tests showed that NC's accuracy on decoding the target was sufficiently high in healthy people, we suspected the involvement of a cognitive decline. In fact, the decoding accuracy was very low in patients who could not count the number of flashes ("This one?"). In the initial stage of development, we overlooked to confirm if the low decoding accuracy was a result of motor dysfunction or another disorder. It is now clear that the risk of dementia should be present in any elder patient, and that the risk of disuse syndrome should be present in any long-term bedridden patient. Therefore, the difficulty exists not only in developing the communication aid itself but also in understanding the user's cognitive ability.

6.5 Necessity of Cognitive Assessment

In developed countries that have become a super-aging society, the problem of dementia such as Alzheimer's disease is becoming more serious, affecting economic costs and societal burden. World Alzheimer Report 2015 estimated that 74.7 million people around the world will be living with dementia by the year 2030 [31]. At this stage, where the prospects for the development of definitive treatments have not yet materialized, cognitive assessment is also required for the early diagnosis of dementia from a viewpoint of its preventive intervention as soon as possible.

Mild cognitive impairment (MCI) is a clinical condition between normal cognition and dementia, causing a slight but noticeable and measurable decline in cognitive abilities. While people in MCI have an increased risk of developing dementia, some never get worse and eventually get better. Although presently available objective diagnostic resources such as volumetric magnetic resonance imaging (MRI), positron emission tomography (PET), molecular imaging (amyloid and tau PET) have been regarded as potential biomarkers for MCI, these markers are relatively insensitive, expensive, and/or invasive. Therefore, EEG analysis may be a good candidate for this purpose, at least, in terms of low cost, non-invasiveness, and widespread availability [32]. A cognitive assessment system that does not require motor response can also be useful for people with severe motor deficits because they were exempt from existing neuropsychological tests that require answers by language or physical response [33, 34]. Of a variety of EEG systems to detect cognitive decline, we focused on the ERP methods below.

Most previous studies on the relationship between ERP and dementia reported increased latency in AD and MCI patients compared to age-matched healthy controls [35, 36]. Besides, lower amplitudes have also been found in patient groups [37–39]. Instead of these evidence, the EPR assessment procedures are not standardized and not included in clinical routine, probably because of the great variability of sensitivity and specificity of ERP measurements.

6.6 Development of the Neurodetector

When we noticed a cognitive decline in patients with severe motor deficits, we started thinking to turn the NC's disadvantage into an advantage; our idea is to use the decoding accuracy as an indicator of cognitive function, especially selective attention. Biomarker of selective attention, which is reflected by the ERP response to the target, should be sensitive to the cognitive decline in the MCI patients too. Therefore, we started the development of the EEG-based cognitive assessment system called the "Neurodetector" (ND). NC's core technologies are compatible with the ND (Fig. 6.4). Furthermore, the market size of ND is bigger than that of NC, which may facilitate the implementation of the NC under the influence of the

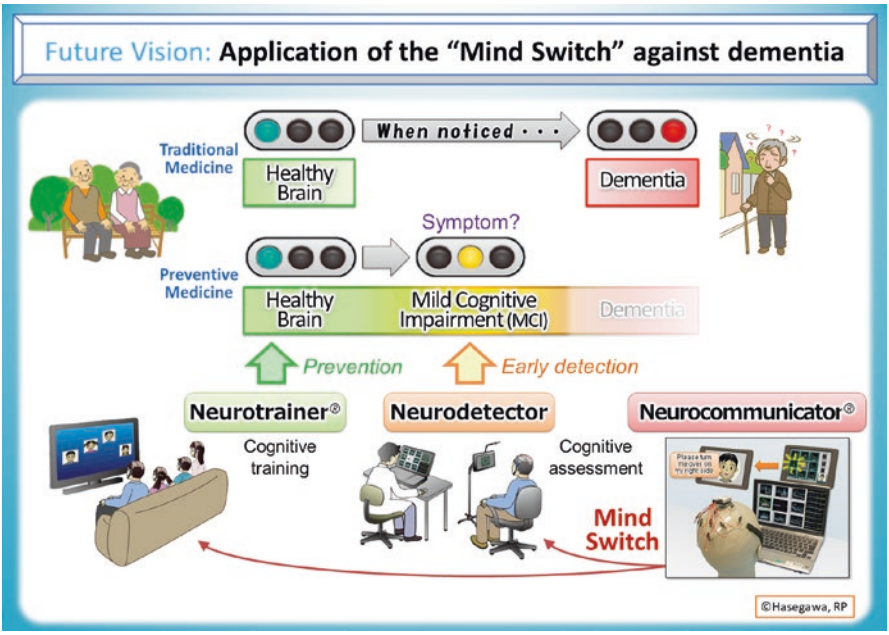

Fig. 6.4 Application of the "Mind Switch" against dementia

ND. The ND will also contribute to the judgment and adjustment of the introduction of the NC to new patients.

We have always tried to make the decoding accuracy in the NC as close to a 100% to develop a reliable communication system. On the other hand, the indicator of cognitive assessment in the ND is not necessarily close to the highest score for people with averaged cognitive abilities. Therefore, we focused on a single ERP response instead of accumulating multiple responses.

As a standard set of the ND, we prepared a test battery with three cognitive tasks that allow us to analyze the detailed attentional processes in each subject. In the main task "target selection task," the subject was required to respond to the appearance of the target, which was sequentially presented, mixed with seven kinds of non-targets. We also used control tasks, the "target only task" without any non-targets, and the "oddball target task" with a single kind of frequent non-target (the popular paradigm for ERP studies). Unlike the target-only task, the subject was requested to discriminate the target from the distractors in the oddball target and the target-selection tasks. Besides, the target-selection task requires top-down attention with a higher concentration while the oddball task does not necessarily require much concentration because the subject can find the target by the bottom-up attention automatically drawn by a sudden change of the environment. Therefore, the task is in an order of difficulty, from the target-only task, oddball-target task, and target-selection task.

We have observed 86 healthy subjects and the differentials of ERP responses between the three types of tasks. Although the ERP seemed to be different among tasks, it was difficult to evaluate how strongly the ERP responded based on its waveform. On the other hand, the change of decoding accuracy based on a single ERP response indicated the gradual increase of task difficulty. This implies that the ERP responses within a subject were dependent on their confidence level of the task. These results suggest that the individual difference between subjects of the decoding accuracy might be a good indicator of the level of cognitive performance reflecting individual differences.

Our future plan is to compare the decoding accuracy between patients and healthy volunteers. As stated above, some previous studies have shown that the average of the peak latencies, as well as the peak values were different among groups of healthy elderlies, elderly with MCI, and patients with AD. Although these studies did not examine the possibility of the categorization of each subject into groups (perhaps because of the excess overlap of peak values and peak latencies), the decoding accuracy by the ND might have the potential to predict the groups the subjects belong to.

6.7 Development of the Neurotrainer

There have been efforts to develop intervention methods to maintain or improve cognitive function in healthy elderly and MCI patients [40, 41]. One of the possibilities to address these issues is cognitive training [42]. This idea is dependent upon the hypothesis that exercising is good not only for the body but for the brain. Although this hypothesis is not fully supported with scientific evidence [43], the field of cognitive interventions is growing. Especially, the computerized cognitive training can be directed to a specific cognitive function; continually adjusted to individual user's performance; be highly immersive and enjoyable; and provide instant quantitative feedback [44].

We focused on the feasibility of ERP-based cognitive training to prevent dementia in elderly people. As the first step, we attempted to develop the "Neurotrainer" (Fig. 6.4) that utilized ERP responses as a Mind Switch to conduct cognitive tasks. We recorded the ERP data from 11 healthy non-elderly adult subjects during the oddball task with a game-like flashcard, giving feedback to the players depending on their level of ERP. All players produced strong ERPs and performed well at the level of about 83% success rate.

We also recorded the ERP data from 30 normal adults, including elderly people, for our research. Subjects performed a cognitive task as a competition with a paired player to select one of the eight gestures presented as the pictures on the PC monitors as soon as possible. The correct prediction was linked to the feedback of the robot gesture such as shooting a basketball. Players produced strong ERPs and performed well at about 85% success rate, regardless of their generation or gender.

These results suggest that the Neurotrainer could be a good candidate for cognitive training, which we plan to eventually commercialize as “bSports (brain-Sports).”

6.8 Summary

As discussed so far, neurotechnology such as an EEG-based BMI has a large potential to facilitate the maintenance/improvement of brain health. Neuroscience is now evolving from the basics to innovative industries—Neurotechnology. Neurotechnology will soon be available in a variety of fields, including medical, personal health care, entertainment, marketing [30], and authentication [45]. For this future advancement, convenient systems to record and decode brain signals are crucial, and we believe that EEG will lead this field with its unique advantages.

References

1. Donoghue JP. Connecting cortex to machines: recent advances in brain interfaces. Nat Neurosci. 2002;5(Suppl):1085–8. https://doi.org/10.1038/nn947.
2. Nicolelis MA. Brain-machine interfaces to restore motor function and probe neural circuits. Nat Rev Neurosci. 2003;4(5):417–22. https://doi.org/10.1038/nrn1105.
3. Wolpaw JR, Birbaumer N, McFarland DJ, Pfurtscheller G, Vaughan TM. Brain-computer interfaces for communication and control. Clin Neurophysiol. 2002;113(6):767–91. https://doi.org/10.1016/s1388-2457(02)00057-3.
4. Plum F, Posner JB. The diagnosis of stupor and coma. Contemp Neurol Ser. 1972;10:1–286.
5. Andrews K, Murphy L, Munday R, Littlewood C. Misdiagnosis of the vegetative state: retrospective study in a rehabilitation unit. BMJ. 1996;313(7048):13–6. https://doi.org/10.1136/bmj.313.7048.13.
6. Monti MM, Vanhaudenhuyse A, Coleman MR, Boly M, Pickard JD, Tshibanda L, Owen AM, Laureys S. Willful modulation of brain activity in disorders of consciousness. N Engl J Med. 2010;362(7):579–89. https://doi.org/10.1056/NEJMoa0905370.
7. Owen AM, Coleman MR, Boly M, Davis MH, Laureys S, Pickard JD. Detecting awareness in the vegetative state. Science. 2006;313(5792):1402. https://doi.org/10.1126/science.1130197.
8. Cruse D, Chennu S, Chatelle C, Bekinschtein TA, Fernandez-Espejo D, Pickard JD, Laureys S, Owen AM. Bedside detection of awareness in the vegetative state: a cohort study. Lancet. 2011;378(9809):2088–94. https://doi.org/10.1016/S0140-6736(11)61224-5.
9. Hayashi H, Kato S, Kawada T, Tsubaki T. Amyotrophic lateral sclerosis: oculomotor function in patients in respirators. Neurology. 1987;37(8):1431–2. https://doi.org/10.1212/wnl.37.8.1431-a.
10. Hayashi H, Oppenheimer EA. ALS patients on TPPV: totally locked-in state, neurologic findings and ethical implications. Neurology. 2003;61(1):135–7. https://doi.org/10.1212/01.wnl.0000069925.02052.1f.
11. Sutton S, Braren M, Zubin J, John ER. Evoked-potential correlates of stimulus uncertainty. Science. 1965;150(3700):1187–8. https://doi.org/10.1126/science.150.3700.1187.
12. Donchin E, Spencer KM, Wijesinghe R. The mental prosthesis: assessing the speed of a P300-based brain-computer interface. IEEE T Rehabil Eng. 2000;8(2):174–9. https://doi.org/10.1109/86.847808.

13. Farwell LA, Donchin E. Talking off the top of your head—toward a mental prosthesis utilizing event-related brain potentials. Electroencephalogr Clin Neurophysiol. 1988;70(6):510–23. https://doi.org/10.1016/0013-4694(88)90149-6.
14. Polich J. Updating P300: an integrative theory of P3a and P3b. Clin Neurophysiol. 2007;118(10):2128–48. https://doi.org/10.1016/j.clinph.2007.04.019.
15. Corralejo R, Nicolas-Alonso LF, Alvarez D, Hornero R. A P300-based brain-computer interface aimed at operating electronic devices at home for severely disabled people. Med Biol Eng Comput. 2014;52(10):861–72. https://doi.org/10.1007/s11517-014-1191-5.
16. Geronimo A, Simmons Z, Schiff SJ. Performance predictors of brain-computer interfaces in patients with amyotrophic lateral sclerosis. J Neural Eng. 2016;13(2):026002. https://doi.org/10.1088/1741-2560/13/2/026002.
17. Guy V, Soriani MH, Bruno M, Papadopoulo T, Desnuelle C, Clerc M. Brain computer interface with the P300 speller: Usability for disabled people with amyotrophic lateral sclerosis. Ann Phys Rehabil Med. 2018;61(1):5–11. https://doi.org/10.1016/j.rehab.2017.09.004.
18. Mak JN, McFarland DJ, Vaughan TM, McCane LM, Tsui PZ, Zeitlin DJ, Sellers EW, Wolpaw JR. EEG correlates of P300-based brain-computer interface (BCI) performance in people with amyotrophic lateral sclerosis. J Neural Eng. 2012;9(2):026014. https://doi.org/10.1088/1741-2560/9/2/026014.
19. Nijboer F, Sellers EW, Mellinger J, Jordan MA, Matuz T, Furdea A, Halder S, Mochty U, Krusienski DJ, Vaughan TM, Wolpaw JR, Birbaumer N, Kubler A. A P300-based brain-computer interface for people with amyotrophic lateral sclerosis. Clin Neurophysiol. 2008;119(8):1909–16. https://doi.org/10.1016/j.clinph.2008.03.034.
20. Nijboer F, Birbaumer N, Kubler A. The influence of psychological state and motivation on brain-computer interface performance in patients with amyotrophic lateral sclerosis—a longitudinal study. Front Neurosci. 2010;4:55. https://doi.org/10.3389/fnins.2010.00055.
21. Pires G, Nunes U, Castelo-Branco M. Statistical spatial filtering for a P300-based BCI: tests in able-bodied, and patients with cerebral palsy and amyotrophic lateral sclerosis. J Neurosci Methods. 2011;195(2):270–81. https://doi.org/10.1016/j.jneumeth.2010.11.016.
22. Riccio A, Simione L, Schettini F, Pizzimenti A, Inghilleri M, Belardinelli MO, Mattia D, Cincotti F. Attention and P300-based BCI performance in people with amyotrophic lateral sclerosis. Front Hum Neurosci. 2013;7:732. https://doi.org/10.3389/fnhum.2013.00732.
23. Sellers EW, Donchin E. A P300-based brain-computer interface: initial tests by ALS patients. Clin Neurophysiol. 2006;117(3):538–48. https://doi.org/10.1016/j.clinph.2005.06.027.
24. Wolpaw JR, Bedlack RS, Reda DJ, Ringer RJ, Banks PG, Vaughan TM, Heckman SM, McCane LM, Carmack CS, Winden S, McFarland DJ, Sellers EW, Shi H, Paine T, Higgins DS, Lo AC, Patwa HS, Hill KJ, Huang GD, Ruff RL. Independent home use of a brain-computer interface by people with amyotrophic lateral sclerosis. Neurology. 2018;91(3):e258–67. https://doi.org/10.1212/WNL.0000000000005812.
25. Yadav AP, Nicolelis MAL. Electrical stimulation of the dorsal columns of the spinal cord for Parkinson's disease. Mov Disord. 2017;32(6):820–32. https://doi.org/10.1002/mds.27033.
26. Hasegawa RP, Blitz AM, Geller NL, Goldberg ME. Neurons in monkey prefrontal cortex that track past or predict future performance. Science. 2000;290(5497):1786–9. https://doi.org/10.1126/science.290.5497.1786.
27. Hasegawa RP, Hasegawa YT, Segraves MA. Single trial-based prediction of a go/no-go decision in monkey superior colliculus. Neural Netw. 2006;19(8):1223–32. https://doi.org/10.1016/j.neunet.2006.05.035.
28. Hasegawa RP, Hasegawa YT, Segraves MA. Neural mind reading of multi-dimensional decisions by monkey mid-brain activity. Neural Netw. 2009;22(9):1247–56.
29. Hasegawa RP, Nakamura Y. An attempt of speed-up of neurocommunicator, an EEG-based communication aid. Lect Notes Comput Sci (LNCS). 2016;9947:256–63.
30. Hasegawa RP, Nakamura Y, Hasegawa YT, Sawahata H. Neural prediction of the target "to BUY" or "NOT to BUY" by the ERP-based cognitive BMI. Int Symp Affect Sci Eng. 2019;2019:1–4. https://doi.org/10.5057/isase.2019-C000043.

31. Prince M, Wimo AGM, Ali GC, Wu YT, Prina M. World Alzheimer Report 2015. The global impact of dementia: an analysis of prevalence, incidence, cost and trends. London. Alzheimer's Disease International 2015.
32. Rossini PM, Di Iorio R, Vecchio F, Anfossi M, Babiloni C, Bozzali M, Bruni AC, Cappa SF, Escudero J, Fraga FJ, Giannakopoulos P, Guntekin B, Logroscino G, Marra C, Miraglia F, Panza F, Tecchio F, Pascual-Leone A, Dubois B. Early diagnosis of Alzheimer's disease: the role of biomarkers including advanced EEG signal analysis. Report from the IFCN-sponsored panel of experts. Clin Neurophysiol. 2020;131(6):1287–310. https://doi.org/10.1016/j.clinph.2020.03.003.
33. Folstein MF, Folstein SE, McHugh PR. "Mini-mental state". A practical method for grading the cognitive state of patients for the clinician. J Psychiatr Res. 1975;12(3):189–98. https://doi.org/10.1016/0022-3956(75)90026-6.
34. Thomson EE, Zea I, Windham W, Thenaisie Y, Walker C, Pedowitz J, Franca W, Graneiro AL, Nicolelis MAL. Cortical neuroprosthesis merges visible and invisible light without impairing native sensory function. eNeuro. 2017;4(6):ENEURO.0262-17.2017. https://doi.org/10.1523/ENEURO.0262-17.2017.
35. Pedroso RV, Fraga FJ, Corazza DI, Andreatto CAA, Coelho FGM, Costa JLR, Santos-Galduróz RF. Latência e amplitude do P300 auditivo na doença de Alzheimer: uma revisão sistemática. Braz J Otorhinolaryngol. 2012;78(4):126–32. https://doi.org/10.1590/s1808-86942012000400023.
36. Polich J, Ehlers CL, Otis S, Mandell AJ, Bloom FE. P300 latency reflects the degree of cognitive decline in dementing illness. Electroencephalogr Clin Neurophysiol. 1986;63(2):138–44. https://doi.org/10.1016/0013-4694(86)90007-6.
37. Hedges D, Janis R, Mickelson S, Keith C, Bennett D, Brown BL. P300 amplitude in Alzheimer's disease: a meta-analysis and meta-regression. Clin EEG Neurosci. 2016;47(1):48–55. https://doi.org/10.1177/1550059414550567.
38. Juckel G, Clotz F, Frodl T, Kawohl W, Hampel H, Pogarell O, Hegerl U. Diagnostic usefulness of cognitive auditory event-related p300 subcomponents in patients with Alzheimers disease? J Clin Neurophysiol. 2008;25(3):147–52. https://doi.org/10.1097/WNP.0b013e3181727c95.
39. Parra MA, Ascencio LL, Urquina HF, Manes F, Ibanez AM. P300 and neuropsychological assessment in mild cognitive impairment and Alzheimer dementia. Front Neurol. 2012;3:172. https://doi.org/10.3389/fneur.2012.00172.
40. Middleton LE, Yaffe K. Promising strategies for the prevention of dementia. Arch Neurol. 2009;66(10):1210–5. https://doi.org/10.1001/archneurol.2009.201.
41. Plassman BL, Williams JW Jr, Burke JR, Holsinger T, Benjamin S. Systematic review: factors associated with risk for and possible prevention of cognitive decline in later life. Ann Intern Med. 2010;153(3):182–93. https://doi.org/10.7326/0003-4819-153-3-201008030-00258.
42. Irazoki E, Contreras-Somoza LM, Toribio-Guzman JM, Jenaro-Rio C, van der Roest H, Franco-Martin MA. Technologies for cognitive training and cognitive rehabilitation for people with mild cognitive impairment and dementia. A systematic review. Front Psychol. 2020;11:648. https://doi.org/10.3389/fpsyg.2020.00648.
43. Yates LA, Ziser S, Spector A, Orrell M. Cognitive leisure activities and future risk of cognitive impairment and dementia: systematic review and meta-analysis. Int Psychogeriatr. 2016;28(11):1791–806. https://doi.org/10.1017/S1041610216001137.
44. Zokaei N, MacKellar C, Cepukaityte G, Patai EZ, Nobre AC. Cognitive training in the elderly: bottlenecks and new avenues. J Cogn Neurosci. 2017;29(9):1473–82. https://doi.org/10.1162/jocn_a_01080.
45. Hasegawa RP, Hasegawa YT, Nakamura Y. Development of neuroauthenticator: feasibility of an EEG-based authentication. Proceedings of 2017 International Conference on Biometrics and Kansei Engineering IEEE Xplore: ((ICBAKE 2017)). 2017. p. 127–31.

Chapter 7
Electromyography and Performance

Tomoki Shiozawa and Hiroki Takada

Abstract Many people are staying home to prevent the spread of COVID-19 infections. The exercise is expected to prevent locomotive syndrome and enhance health promotion. Incidentally, the motion is driven by contraction/relaxation of muscles, which can be evaluated by the motion capture system and/or the surface Electromyography (sEMG). Now, the sEMG is known to be a noninvasive, unconstrained measurement that can be recorded simultaneously with the other bio-signal. In this chapter, a statistical procedure is herein introduced to evaluate the sEMG during the biofeedback training (BFT). We believe that the mathematical methods in this chapter will contribute to one of the nature and/or the basic techniques of the neuro-biofeedback and its training.

Keywords Electromyography (EMG) · Sensor output evaluation (SOE) system · Biofeedback training (BFT) · Functional near-infrared spectroscopy (fNIRS)

7.1 Introduction

The Italian physician L. Galvani showed the relationship between electricity and muscle contraction that occurs in the electric fluid that is carried to the muscles by the nerves. He coined the term *animal electricity* to describe the force that activates the muscles. One hundred fifty years after he determined their activation as being generated by an electric fluid that is carried by the nerves to the muscles [1], the mathematician N. Wiener studied an artificial hand controlled by an electrical

T. Shiozawa (✉)
Health Administration Center, Aoyama Gakuin University, Tokyo, Japan
e-mail: shiozawa@busi.aoyama.ac.jp

H. Takada
Department of Human and Artificial Intelligence, University of Fukui, Fukui, Japan
e-mail: takada@u-fukui.ac.jp

H. Takada, K. Yokoyama (eds.), *Bio-information for Hygiene*, Current Topics in Environmental Health and Preventive Medicine,
https://doi.org/10.1007/978-981-15-2160-7_7

current in the muscles. He proposed *cybernetics* [2], which focused on the myoelectric (ME) potential of about −90 mV recorded as electromyograms. The ME potential in skeletal muscles is often measured and recorded. The bio-signals are known to be generated by the following mechanism [3, 4]:

1.1. Form: Both ends of skeletal muscles are adhered to bones through tendons. Muscle fibers are 50–100 μm in diameter and are aligned longitudinally in a muscle cell. The fibers consist of muscular fibrils that are 1–2 μm in diameter and are composed of two types of filaments. A sarcomere is a unit of a muscle fiber in morphology; it is the region between disc-like Z bands that partition off the fibrils into two portions.
1.2. Route: The (efferent) nerve impulse (action potential) from the primary motor cortex (M1) cooperates with the premotor area and is transferred to α-motor neurons in the spinal cord through pyramidal tracts, extrapyramidal tracts, and the brainstem. Moreover, it arrives at the motor endplate through the terminal axon and results in muscle cell membrane excitation. This excitation of the muscle cell membrane transforms both sides of the muscle fiber. The membrane current is generated by the depolarization of the muscle membrane. Changes in the electrical potential (7–20 Hz) occur in the membrane current through the surrounding volume conductor. Muscular motion follows the above-mentioned bio-signal process.

ME potentials are induced by changes in nerve impulse firing patterns. Several muscle fibers controlled by a motor nerve are collectively called a motor unit (MU), several of which can be excited by nerve impulses, causing an MU action potential. The MU action potential measured on the skin's surface is the surface ME potential and is observed at a site that is spatially distant from the local region where the MU action potential waves are generated. Moreover, the larger is the MU, the faster is its contraction speed and its fatigue accumulation [3]. Electromyography (EMG) is clinically employed to detect an anomalous MU.

Several electromyographic methods are currently used, but needle electromyography (nEMG) and surface electromyography (sEMG) are most often applied. To physiologically evaluate electromyographic wave patterns for the detection of abnormalities, wave patterns obtained with nEMG or sEMG have been macroscopically examined, and subjectively judged by physicians.

2.1. nEMG findings are used to classify a disorder as neurogenic or myogenic. In the case where a disorder is both neurogenic and myogenic, nEMG findings provide important information about whether the disorder is acute, sub-acute, or chronic [5]. However, a needle electrode probe is used, which is percutaneously inserted into the muscular tissue.
2.2. sEMG findings are used for various evaluations, such as the classification of trembling for the diagnosis of involuntary motion, the diagnosis or differential diagnosis of dystonia and spasm, and the identification of involuntary constrictor muscles [4].
2.3. sEMG is also used for the determination of the electric potential through a nerve conduction examination (this procedure is called evoked EMG). In

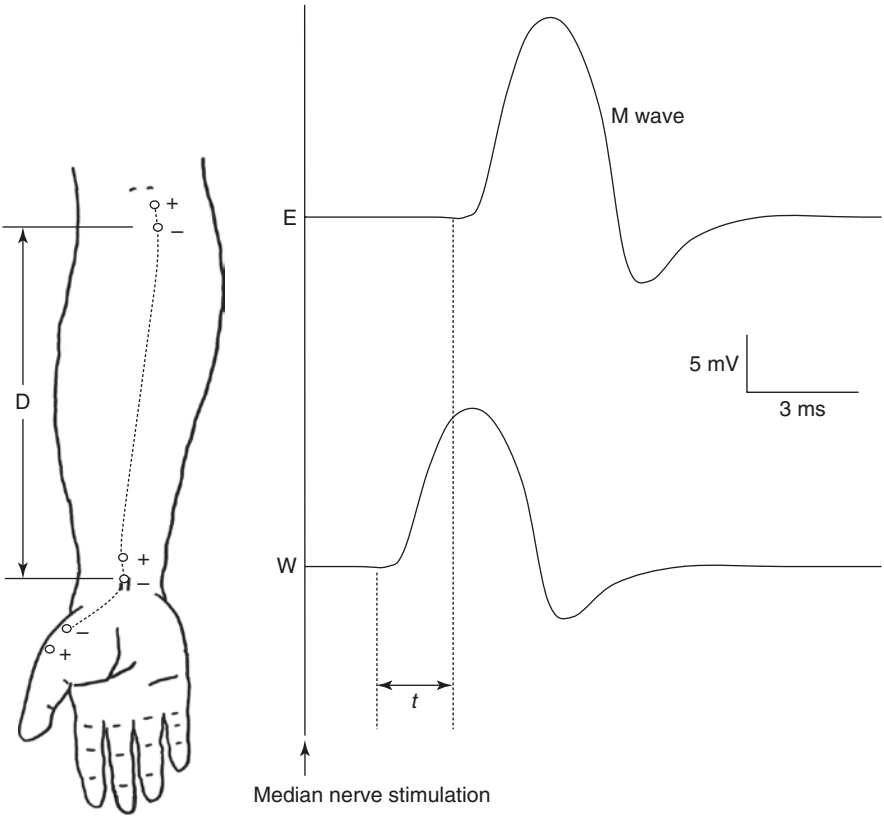

Fig. 7.1 Nerve conduction study of the median nerve. M waves obtained from the abductor pollicis brevis muscle by stimulating the wrist and elbow joints. Motor conduction velocity = D/*t*

evoked EMG, the electrostimulation of peripheral nerves is performed percutaneously (Kimura, 1989). Nerve conduction study (often called a nerve conduction examination) (Fig. 7.1) can reveal several findings (Appendix).

The examination methods described, except for method (2.2), are invasive and cause severe pain in patients. "Smoothing" and "integration" refer to two ways of quantifying EMG energy over time. Smoothing refers to continuously averaging out the peaks and valleys of a changing electrical signal, and integration refers to measuring the area under a curve over a period of time. These methods are used to examine the relative degree of muscular contraction and are also employed to provide parameters for the evaluation of muscular training conditions [6]. However, the results obtained are affected by the location of the measuring electrodes and the shape and size of the probes. As described above, this means that no algorithm for the quantification of the degree of muscular abnormalities or recovery has been established although EMG findings are macroscopically and subjectively evaluated. In this study, we applied the measurement parameters that have been developed for

evaluating the average rectified sEMG (ARS) data obtained from perineal muscles during biofeedback training (BFT) for the treatment of dysuria [7] and evaluated the effects of this training [8, 9].

7.2 Biofeedback Training

Kegel (1948; 1951) was the first to use BFT for the treatment of urinary incontinence (UI), and it was observed that if the pelvic floor muscles were hypotonic, bladder suspension surgery was less effective for treating stress-related incontinence [10, 11]. In order to improve the contractibility of the pubococcygeus portion of the levator ani muscle, Kegel invented the pressure perineometer [10, 11]. In the USA, at least 13 million community-living adults and more than 50% of all residents in nursing facilities suffer from UI [12]. The direct medical expenditure incurred for the care of these people is estimated to be >$15 billion annually, in addition to the $35.2 billion incurred annually for nursing home residents [13]. There is a consensus that in most cases, behavioral treatment modalities, including biofeedback, should be used before invasive modalities such as surgery.

7.2.1 Instrument

A biofeedback instrument has three tasks to perform [13]:

3.1. To monitor (in some way) a physiological process of interest
3.2. To measure (objectify) what is monitored
3.3. To present what is monitored or measured as meaningful information

EMG and biofeedback are often used simultaneously to handle movement during the procedure. Edmund Jacobsen commenced research at Harvard in 1908, and throughout the 1920s and 1930s worked to develop progressive muscle relaxation as an effective behavioral technique for the alleviation of neurotic tensions and many functional medical disorders [14]. He used crude electromyographic equipment to monitor the levels of muscle tension in his patients during the course of treatment. The classification of and historical perspectives on biofeedback applications can be found in reports by [15–17].

Temporal data are obtained using sEMG whose data is generally recorded by a computer at 2 kHz. The integral calculation was performed every 0.1 s. The average rectified sEMG (ARS) is calculated in real time and outputted. The subject is told to observe the outputted wave patterns and instruction signals, for instance the rectangular waves with constant-second period, superimposed on the same display, and then intermittently and continuously contract the target muscles. Transient periods were also added to this rectangular wave before constant amplitudes as necessary [18, 19].

7.2.2 Training

The following outline summarizes the training steps:

4.1. Exercise motion and posture were instructed.
4.2. Away from the center of the target muscles, AMG electrodes were placed at intervals of a few centimeters, and subjects were asked to perform their maximum voluntary contraction. The average integral waveform of the surface EMG was calculated for this period of muscle contraction and muscular activity corresponding to $\alpha = 75\%$ (third quartile) of maximum voluntary contraction was then estimated.
4.3. Muscular activity corresponding to $\alpha\%$ of maximum voluntary contraction was shown to the subject as the instruction signal and five cycles of intermittent signals were provided for 5–40 s of contraction (gradual build-up during the first 0–20 second), hereafter referred to as the "transient period (TP)," followed by 5–20 s of constant muscle activity, hereafter referred to as the "muscle contraction period (MCP)" and then 5–40 s of relaxation (the first 5–20 s are referred to as the pre-rest and the last 5–20 s as post-rest).

These series of flows were carried out eight times in a row. The surface EMGs were not recorded for the first two or three periods of these series as a practice.

As above-mentioned, the EMG waveforms were rectified and smoothed in real time at 0.1 s intervals of integration. These integral waveforms were then shown to subjects in addition to the instruction signals (teacher signal). Noise was removed from the surface EMG by inserting an AC removal filter whose cut-off frequency for the high range cutoff filters were set at 1 kHz. The evaluation was performed through the following "sensor output signal evaluation system."

7.2.3 Evaluation

The sensor output evaluation (SOE) system, developed in 2006 [20], can evaluate the fitness of the teacher signal in BFT whose aim is not the completion of mere muscular training but is to enhance muscle control. The ARS were analyzed according to the following mathematical algorithms of the sensor output signal evaluation system. Taking a mean of the ARS (MARS) as a threshold:

5.1. The MARS value during the muscular relaxation period and the measurement parameters in the following terms (5.2)–(5.4) indicating the ARS shape were determined every cycle, and the ARS values obtained from the target muscles were evaluated.
5.2. The maximum amplitude value was extracted and recorded.
5.3. The continuous muscular contraction duration (time between the first and last maximal values in a cycle exceeding the MARS) was measured.

5.4. The time constant of the exponential decay curve fit to the maximal points during the muscular contraction period in the BFT (all maximal values between the first and last maximal values exceeding the MARS in a cycle; β) were extracted as $\{x_m(t)\}$ and fit to the exponential decay curve

$$\hat{x}_m(t) = C\exp[-\beta t].$$

The numerical sequences of the four measurement parameters were calculated for each period in the teacher signals. However, a significant age correlation has been found in the parameter β determined at a certain repetition period [9, 21]. The relationship between the age of the subjects who had undergone sEMG and the values estimated in the seventh cycle were statistically examined to evaluate correlations between parameter and age measurements.

7.3 Visualization for Motion Performance

The motion is driven by the contraction/relaxation of muscles. Now, postural change and the performance can be evaluated by the simultaneous measurement of video cameras and the EMGs during the motion. We can note the visualization of the contraction/relaxation of muscles driving the motion performance [22, 23]. A part of these works, especially in [22], will be explained in the Chap. 10 in detail. Synchronous visualization of motion and cardiovascular performance indicators can reveal the relationship between changes in cardiovascular performance and motion during daily activities. In their visualization schematics, the motion is measured by the motion capture which is synchronized with the sEMG and Electrocardiogram. Here, we focus on the other visualization of the brain activity to control the motion performance.

7.3.1 Brain Activity During the BFT

One technique for the noninvasive measurement of brain activity that has been developed in recent years is brain functional imaging using near-infrared spectroscopy (fNIRS). With developments such as the miniaturization of diagnostic equipment, brain science is developing rapidly and a variety of brain activities are being defined [24–26]. The fNIRS is less constraining to the subject than the other measurement methods, such as functional magnetic resonance imaging (fMRI) and positron emission tomography (PET). In fact, previous work by the authors demonstrated the possibility that specific “local movement” (masticatory movement in this case) stimulates activity of the prefrontal cortex [27].

In conjunction with the last step (4.3), the optical brain function imaging device LABNIRS (Shimadzu Corporation, Kyoto) was used to measure Oxy-Hb concentration (Co) and Deoxy-Hb concentration (Cd) at a sampling frequency of 17.5 Hz [18, 19]. A holder was placed on the subject's head, with light-emitting/receiving probes.

Biometric data were obtained for the femoral rectus muscle in ten healthy young individuals (24.7 ± 4.5 years) with no abnormalities in the extremities and no past medical history of ear or nervous system disease. All subjects were about average size, and their body mass index (BMI) was distributed from 18 to 25 kg/m^2. The experiment was fully explained to the subjects beforehand, and written consent was obtained. The experiment was approved by the Ethics Committee of the Department of human and artificial intelligent systems, Graduate School of Engineering University of Fukui (No. 2).

Subjects were asked to sit back on a chair (with four fixed legs) and to kick with their dominant leg against a belt, attached to the lower part of the chair (Fig. 7.2). In this example, femoral rectus muscles were target to evaluate the BFT. Electromyography of examinees' rectus femoris muscles and near-infrared spectroscopy were simultaneously conducted to investigate the relationship between BFT and local cerebral blood flow. It was found that the change in Co during the MCP was greater than that during the pre-rest. The influence of a kicking motion on brain functioning was confirmed. These findings suggest that BFT is effective in activating working memory. Also, the time series of the changes in the CBF during

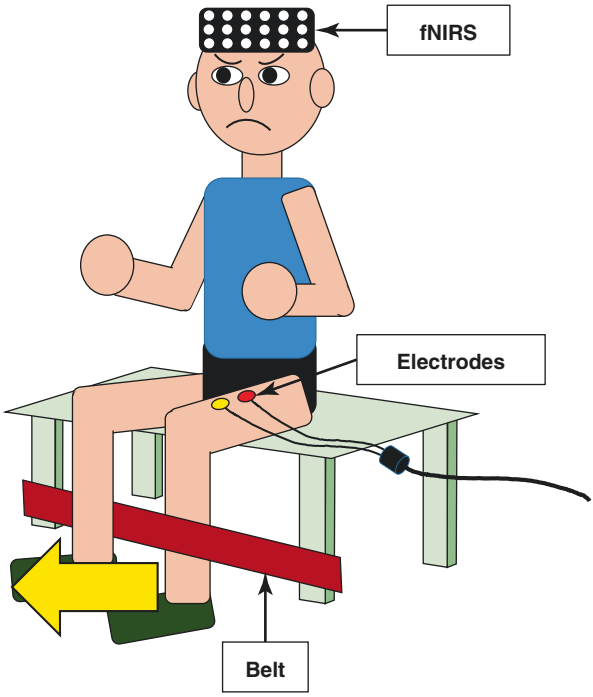

Fig. 7.2 An experiment image for Biofeedback training (BFT). In this case, the target muscle is set to be the femoral rectus muscles. Disposable electrodes are applied at an interval of several centimeters to the center of the femoral rectus muscles in the dominant leg

the BFT showed a distribution that deviated significantly from the normal distribution [18].

7.3.2 Mathematical Design for Bandpass Filters of the CBF

The BFT is also known as a countermeasure for patients with intractable epilepsy and a reduction method for mental stress [28–36]. However, a method for objectively evaluating does not have been established yet whereas subjective evaluation and findings were stated in the previous study. Also, there is no study to evaluate the cerebral hemodynamics and investigate the cerebral blood flow regulation during the BFT. According to our previous consideration in the bio-signal, it is necessary to evaluate a robust bio-system by using mathematical models because the changes in the system can be hardly found out. Moreover, it is important to set the cut-off frequency to denoise in the bio-signal, especially in the brain function analysis. However, there is no prior research that defined the cut-off frequency, based on the mathematical consideration. Therefore, we herein focused on the mathematical design of the cut-off frequency f_0 in the low-pass filtering.

The authors analyzed time sequences of the Co. The time series were smoothed by the low-pass filtering [19]. We can $\{x_t\}$. Translation errors E_{trans}, measuring the degree of determinism for the mathematical model of the time series [37], were herein estimated for each time series in addition to sequences of their temporal differences by the Double Wayland algorithm [38, 39]. Also, we compared E_{trans} for the abovementioned time series with their surrogate sequences that were generated by the Fourier shuffle (FS) algorithm [40, 41]. Setting the cut-off frequency to be $1 \geq f_0 \geq 0.3$ Hz, we have succeeded in findings that the mathematical model of the cerebral blood flow is regarded as a stochastic differential equation. Setting the cut-off frequency in the low-pass filtering to be less than 0.2 Hz, noise reduction is considered to be more effective than the other cases mentioned above. Also, we have succeeded in findings of the nonlinearity for hemodynamics in the cerebral blood flow on the frontal lobe during the muscle contraction and the post-rest. However, the cerebral blood flow in the frontal lobe is not always generated by the stochastic process as in $f_0 \leq 0.2$ Hz.

We believe that the mathematical methods in this chapter will contribute to one of the nature and/or the basic techniques of the neuro-biofeedback and its training [42, 43]. It is expected that this neuro biofeedback technique is applied to mindfulness meditation, which is introduced in the last chapter. Mind, body, and brain in humans are inseparable systems, and mental hygiene, which will be discovered in the future, is an uncharted territory.

Appendix

1. Decay of nerve conduction velocity (demyelination)
2. Attenuated amplitude of evoked electromyogram (axonal motor neuropathy)
3. Attenuated amplitude of sensory nerve action potential (axonal sensory neuropathy)
4. Temporal dispersion of electromyogram (existence of demyelinating disorder)
5. Attenuation (myasthenia gravis) or amplification (Lambert–Eaton myasthenic syndrome) of evoked potential due to repetitive stimulation
6. Conduction block (demyelination)
7. Delay of central motor conduction time (motor conduction disturbance of central nervous system)

References

1. De GL. Viribus Electricitatis in Motu Musculari Commentaries. De Bononiensi Scientiarum et Artium Instituto Atque Academia Commentarii. 1791;7:363–418.
2. Wiener N. Cybernetics. The technology press. New York: Wiley; 1948.
3. Akazawa K. Bioinformatic engineering. Tokyo: Tokyo Denki University Press; 2001.
4. Kizuka T, Masuda T, Kiryu T, Sadoyama T. Practical usage of surface electromyography. Tokyo: Tokyo Denki University Press; 2006. p. 65–92.
5. Kimura J. Electrodiagnosis in diseases of nerve and muscles: principles and practice. 2nd ed. Philadelphia: Oxford University Press; 1989. p. 209–304.
6. Aukee P, Penttinen J, Immonen P, Airaksinen O. Intravaginal surface EMG probe design test for urinary incontinence patients. Acupunt Electro-Ther Res Int J. 2002;27:37–44.
7. Tries J, Eisman E. Urinary incontinence—evaluation and biofeedback treatment. In: Schwartz MS, editor. Biofeedback a practitionaer's guide. New York: Guilford Press; 1995. p. 597–629.
8. Takada H, Shiozawa T, Miyao M, Matsuura M, Takada M. Consideration of indices to evaluate age-related muscle performance by using surface electromyography. Adv Exp Med Biol. 2010;680:585–91. https://doi.org/10.1007/978-1-4419-5913-3_64.
9. Shiozawa T, Takada H, Matsuura Y, Miyao M. Sensor output signal evaluation system for biofeedback training and its appreciation. In: Takada H, editor. Electromyography: new developments, procedures and applications. New York: NOVA Science; 2012. p. 67–84.
10. Kegel AH. Progressive resistance exercise in the functional restoration of the perineal muscles. Am J Obstet Gynecol. 1948;56:238–48.
11. Kegel AH. Physiologic therapy for urinary incontinence. J Am Med Assoc. 1951;146:915–7.
12. Fantil JA, Newman DK, Colling J. Urinary incontinence in adults: clinical practice guideline. MI: University of Michigan Library; 1996.
13. Peek CJ. A primer of biofeedback instrumentation. In: Schwartz MS, Andrasik F, editors. Biofeedback. New York: Guilford Press; 1995. p. 597–629.
14. Jacobson E. Progressive relaxation. Chicago: University of Chicago Press; 1938.
15. Gatchel RJ, Price KP. Critical applications of biofeedback. New York: Pergamon Press; 1979.
16. Gaarder KR, Montgomery PS. Clinical biofeedback: a procedural manual for behavioral medicine. 2nd ed. Baltimore: Williams & Wilkins; 1981.
17. Basmajian S. An anthology of visual poetry and collage. Toronto: Sober Minute Press; 1989.
18. Takada H, Miyao M, Shiozawa T, Watanabe T, Takada M. Distribution of cerebral blood flow during biofeedback training. Descente Sports Sci. 2015;36:78–89.

19. Tanimura T, Iida D, Jono Y, Takada M, Matsuura Y, Takada H. Nonlinear analysis using multiple cutoff frequencies for local cerebral blood flow during biofeedback training. J Adv Med Res. 2019;28(6):1–12.
20. Shiozawa T, Takada H, Miyao M. Sensor output signal evaluation system. Japan Patent 2012;4859035.
21. Takada H, Matsuura Y, Shiozawa T, Miyao M. Nonlinear analysis for evaluation of age-related muscle performance using surface electromyography. In: Schwartz M, editor. EMG methods for evaluating muscle and nerve function. London: InTech; 2012. p. 91–106.
22. Matsukawa T, Yokoyama K. Visualizing physiological information based on 3DCG. Forma. 2010;25:11–4.
23. Sunada H, Yokoyama K, Matsukawa T, Harada S, Takada H, Matsuura Y, Hirata T. Analysis of the motion in Kendo using motion capture system. IEICE Tech Rep (ME Bio Cyber.). 2011;111(121):31–5.
24. Furubayashi T, Motizuki H, Terao Y, Arai N, Hanajima R, Hamada M, Matsumoto H, Nakatani-Enomoto S, Okabe S, Yugeta A, Inomata-Terada S, Ugawa Y. Cortical hemoglobin concentration changes underneath the coil after single-pulse transcranial magnetic stimulation. J Neurophysiol. 2013;109(6):1626–163.
25. Groiss SJ, Motizuki H, Furubayashi T, Kobayashi S, Nakatani-Enomoto S, Nakamura K, Ugawa Y. Quadri-pulse stimulation induces stimulation frequency dependent cortical hemoglobin concentration changes within the ipsilateral motor cortical network. Brain Stimul. 2013;6(1):40–8.
26. Herold F, Wiegel P, Scholkmann F, Thiers A, Hamacher D, Schega L. Functional near-infrared spectroscopy in movement science. Neurophotonics. 2017;4(4):041403. https://doi.org/10.1117/1.NPh.4.4.041403.
27. Matsuura Y, Taniguchi T, Sugiura A, Miyao M, Takada H. Distribution of cerebral blood flow during gum-chewing. Forma. 2012;27:1–4.
28. Finley WW, Smith HA, Etherton MD. Reduction of seizures and normalization of the EEG in a severe epileptic following sensorimotor biofeedback training. Biol Psychol. 1975;2(3):189–203.
29. Tremback-Ball A, Gherghel E, Hegge A, Kindig K, Marsico H, Scanlon R. The effectiveness of biofeedback therapy in managing bladder bowel dysfunction in children. J Pediatr Rehabil Med. 2018;11(3):161–73. https://doi.org/10.3233/PRM-170527.
30. Tremback-Ball A, Gherghel E, Hegge A, Kindig K, Marsico H, Scanlon R. Awareness of comfort immediately after a relaxation therapy session affects future quality of life and autonomic function. J Pediatr Rehabil Med. 2018;11(3):161–73. https://doi.org/10.3233/PRM-170527.
31. McKenzie RF, Ehrisman WJ, Montgomery PS, Barnes RH. The treatment of headache by means of electroencephalographic biofeedback. Headache. 1974;13(4):164–72.
32. van Gelder LMA, Barnes A, Wheat JS, Heller BW. The use of biofeedback for gait retraining. Clin Biomech (Bristol, Avon). 2018;59:159–66. https://doi.org/10.1016/j.clinbiomech.2018.09.020.
33. Ma CZ, Zheng YP, Lee WC. Changes in gait and plantar foot loading upon using vibrotactile wearable biofeedback system in patients with stroke. 2018;25(1):20–7. https://doi.org/10.1080/10749357.2017.1380339.
34. Nagai Y, Aram J, Koepp M, Lemieux L, Mula M, Critchley H, Sisodiya S, Cercignani M. Epileptic seizures are reduced by autonomic biofeedback therapy through enhancement of fronto-limbic connectivity. EBioMedicine. 2018;27:112–22. https://doi.org/10.1016/j.ebiom.2017.12.012.
35. Xu J, Bao T, Lee UH, Kinnaird C, Carender W, Huang Y, Sienko KH, Shull PB. Configurable, wearable sensing and vibrotactile feedback system for real-time postural balance and gait training. 2017;14(1):102. https://doi.org/10.1186/s12984-017-0313-3.
36. Kubik P, Kraj B, Kubik A. Neurofeedback therapy influence on clinical status and some EEG parameters in children with primary generalized epilepsy. Przegl Lek. 2016;73(3):152–6.

37. Wayland R, Bromley D, Pickett D, Passamante A. Recognizing determinism in a time series. Phys Rev Lett. 1993;70:530–82.
38. Takada H, Morimoto T, Tsunashima H, Yamazaki T, Hoshina H, Miyao M. Applications of double-Wayland algorithm to detect anomalous signals. Forma. 2006;21(2):159–67.
39. Yoshikawa K, Takada H. Effect of Gaussian noise amplitude on translation error estimated by double-Wayland algorithm. J Math Syst Sci. 2012;2:482–8.
40. Theiler J, Eubank S, Longtin A, Galdrikian B, Farmer JD. Testing for nonlinearity in time series: the method of surrogate data. Physica D. 1992;58:77–94.
41. Theiler J, Prichard D. Constrained-realization Monte-Carlo method for hypothesis testing. Physica D. 1996;94(4):221–35.
42. Chang M, Iizuka H, Kashioka H, Naruse Y, Furukawa M, Ando H, Maeda T. Unconscious improvement in foreign language learning using mismatch negativity neurofeedback: a preliminary study. PLoS One. 2017;12(6):e0178694. https://doi.org/10.1371/journal.pone.0178694.
43. Kozlova LI, Shtark MB, Mel'nikov ME, Verevkin EG, Savelov AA, Petrovski ED. EEG-fMRI study of alpha-stimulation Neurobiofeedback training course. Bull Exp Biol Med. 2016;161(5):623–8. https://doi.org/10.1007/s10517-016-3471-6.

Chapter 8
Polysomnography

Fumiya Kinoshita, Masumi Takada, and Meiho Nakayama

Abstract Polysomnography (PSG) is a polygraph test that simultaneously records multiple biometric information such as brain waves, eye movements, electromyograms, respiration, and electrocardiograms during sleep over time. PSG is used in the diagnosis of sleep disorders and measurements on treatment effects as it can comprehensively and objectively evaluate changes in sleep stages and physiological phenomena during the course of overnight sleep. Current PSG inspection equipment can automatically evaluate accompanying events such as sleep stage or respiratory events. However, currently, evaluations from automatic analysis are not reliable, and inspection decisions are required. In this chapter, we present our efforts toward implementing automatic REM sleep without atonia (RWA) decisions with REM sleep behavior disorder (RBD).

Keywords Polysomnography (PSG) · REM sleep behavior disorder (RBD) · REM sleep without atonia (RWA) · Automatic analysis · Support vector machine (SVM) Convolutional neural network (CNN)

F. Kinoshita (✉)
Toyama Prefectural University, Toyama, Japan
e-mail: f.kinoshita@pu-toyama.ac.jp

M. Takada
Yokkaichi Nursing and Medical Care University, Yokkaichi, Mie, Japan
e-mail: takada@y-nm.ac.jp

M. Nakayama
Nagoya City University, Aichi, Nagoya, Japan
e-mail: nakayama@med.nagoya-cu.ac.jp

H. Takada, K. Yokoyama (eds.), *Bio-information for Hygiene*, Current Topics in Environmental Health and Preventive Medicine,
https://doi.org/10.1007/978-981-15-2160-7_8

8.1 Introduction

Sleep is not just an activity that allows recovery from fatigue but also essential for maintaining physical and mental health. Several research studies have reported interesting associations between sleep and health [1–7]. Studies involving various generations, from newborns to the elderly, have consistently reported that sleep is influenced by developmental stages and individual internal/external environments, and that sleep duration actually decreases with age once we reach adulthood [8].

Scientific studies have classified sleep into two major types: REM and non-REM sleep. Eugene Aserinsky and Nathaniel Kleitman, at the University of Chicago, first discovered REM sleep when they conducted experiments that measured the brain waves and eye movements during sleeping [9]. Prior to the discovery of REM sleep, the prevailing belief on the sleeping mechanism was that the sleeping state in humans and animals was uniform throughout the night. Hence, the discovery of REM sleep was a breakthrough that overturned conventional wisdom. Subjects in this experiment exhibited brain waves similar to a wakeful state and rapid eye movement (REM) during sleep, despite appearing to be a deep sleep. As a result, the sleep during this state was termed as REM sleep. Shortly thereafter, it was discovered that two types of sleep were experienced by humans and animals: REM and non-REM. Further investigations found that sleep as an activity actually consisted of alternate and cyclical appearances of these two forms of sleep. Non-REM sleep occurs immediately after falling asleep, and only after approximately 1 h of deep non-REM sleep does REM sleep appear. Non-REM and REM sleep subsequently alternate. This cycle is referred to as the sleep cycle, and it lasts approximately 80–100 min [10]. The percentage of REM sleep in the total sleep duration was approximately 50% in newborns, but it became roughly equivalent to those in adults (approximately 20%) by the age of 3 years.

Age-related mental, physical, and environmental changes increase the risk of insomnia and sleep disorders [11]. Neural mechanism disorders associated with REM sleep often underlie parasomnia, which frequently occurs in old age, and there is a concern that a serious central nervous system disease may be present in the background. Here, one such parasomnia includes REM sleep behavior disorder (RBD) [12, 13]. Body movement normally cannot occur during REM sleep owing to the behavioral characteristics of the muscle tone suppression mechanism. However, dysfunction of the muscle tone suppression mechanism along with RBD can cause complex and violent movement, such as swinging the wrists, punching, and kicking, despite being in REM sleep. Patients who are immediately awoken after the appearance of RBD immediately become conscious and can talk in detail about their dream experiences; hence, it is believed that RBD manifests itself as movements based on events during their dreams. Such abnormal behaviors are often violent, and there is a risk that they may hit furniture and hurt themselves or be a risk to their families or partners. For these reasons, RBD requires quick treatment. Polysomnography (PSG) is a method for objectively evaluating the sleep state. PSG

allows the capturing of the depth and course of overnight sleep. It also records various biometric information while capturing autonomous nervous functions and other accompanying phenomena during the sleep cycle.

8.2 Polysomnography

PSG is a polygraph test that simultaneously records multiple biometric information such as brain waves, eye movements, electromyograms, respiration, and electrocardiograms during sleep over time. PSG is the gold standard for diagnostic inspections of sleep-related diseases in sleep medicine and treatment [14, 15]. PSG is also used in the diagnosis of sleep disorders and measurements on treatment effects as it can comprehensively and objectively evaluate changes in sleep stages and physiological phenomena during the course of overnight sleep [16, 17].

Routinely performed PSG currently records brain waves, electrooculograms, mentalis muscle electromyograms, electrocardiograms, bilateral anterior tibial muscle electromyograms, respiration, snoring, body position, and arterial oxygen saturation. The standard PSG inspection methods and sleep-stage evaluations were standardized by Rechtschaffen and Kales in 1968 and became widespread [18], but the scoring manual created by the American Academy of Sleep Medicine (AASM) in 2007 has also witnessed widespread use in recent years [19].

Records of brain waves, electrooculograms, and mentalis muscle electromyograms are needed for sleep-stage evaluation, according to the latest AASM scoring manual [20]. Sleep stage is classified across five stages, with the notations of stage W (wake), stage N1, stage N2, stage N3, and stage R (REM). Evaluations are continuously performed every 30 s from the first section (epoch) at the start of inspection, and one of the sleep stages is assigned to each epoch. Sleep stages that occupy a larger proportion within the epoch are assigned when there are two or more sleep stages in a single epoch.

Current PSG inspection equipment can automatically evaluate accompanying events such as sleep stage or respiratory events. However, currently, evaluations from automatic analysis are not reliable, and inspection decisions are required. Meanwhile, there may be cases where variation in the results may occur according to the clinical laboratory technician in charge of inspection decisions, which can be problematic as these decisions require large amounts of time and experience.

8.3 RBD Evaluations Based on PSG Findings

One of the defining features of RBD is the occurrence of REM sleep without atonia (RWA). This is believed to be caused by the inhibition of muscle activity suppression for some unconfirmed reasons during REM sleep. Historically and traditionally, it

was believed that responsible lesions tend to exist in the brain's stem, which is the part of the brain that controls human arousal and sleep, and it has been indicated that its progression is related to the progression of Parkinson's disease and Lewy body dementia [21]. The confirmation of abnormal behavior during video monitoring in PSG and the frequency of RWA occurrence during REM sleep based on physiological indicators are essential diagnostic items in the diagnosis of RBD. Muscle activity caused by RWA is normally classified into two types: continuous muscle activity (tonic activity) and excessive transient muscle activity (phasic activity) [20]. The AASM scoring manual recommends the evaluation of RWA according to the following definitions:

- Tonic activity: When the amplitude of chin-EMG is continuously higher than the minimum amplitude during non-REM sleep for at least 50% of the total time in one REM sleep epoch.
- Phasic activity: When one REM sleep epoch is divided into ten consecutive small epochs lasting 3 s, with excessive transient muscle activity bursts included in at least five (50%) small epochs. The excessive transient muscle activity bursts mentioned here refer to those whose duration is 0.1–5.0 s and amplitude is more than four times that of background EMG activity.

The recorded results are generally read and interpreted during inspection decisions by clinical laboratory technicians when PSG is used to diagnose sleep disorders. However, no clear criteria have been established for these decision methods, and many decision criteria other than those of the AASM scoring manual have been proposed [22, 23], with no internationally unified rules having been established. Given that the decision criteria are not clear, RWA decision software is also not commercially available, and clinical laboratory technicians must conduct inspection decisions in actual clinical settings. RWA is not only considered to be an RBD-specific finding but also one that reflects the progression of pathological conditions.

8.4 Efforts Toward Automatic Analysis

We seek to develop an RWA decision program that simulates clinical laboratory technicians by considering the inspection decisions by clinical laboratory technicians and the decision results from the proposed automated algorithms. Thus far, we have compared and investigated the two machine learning methods of support vector machine (SVM) and convolutional neural network (CNN) for RWA decisions [24, 25]. In the following sections, we present our efforts toward implementing automatic RWA decisions.

8.4.1 Acquisition of Experimental Data

We used the measurement data on 12 men and women (average age ± standard deviation: 72.7 ± 1.7 years) who have visited the Nagoya City University Hospital Sleep Treatment Center for PSG inspection owing to suspected REM sleep behavioral disorders. The Philips Respironics Alice 5 was used as the measurement device, and each physiological indicator was measured at a sampling frequency of 200 Hz. The chin-EMG during REM sleep measured from the PSG of the 12 subjects was used as the experimental data. The chin-EMG during REM sleep was divided into 30 s intervals, and RWA decisions were taken based on visual inspection by an individual clinical laboratory technician. The total acquired number of epochs of the chin-EMG during REM sleep was 2094 epochs (total of 1047 min). Figure 8.1

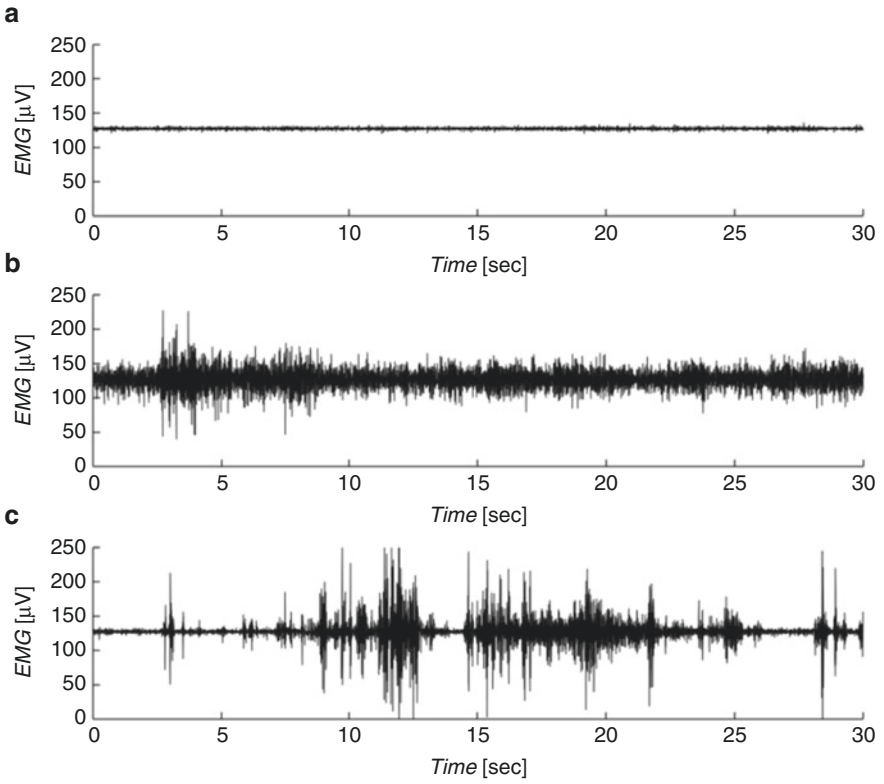

Fig. 8.1 Example of epochs labeled based on inspection decisions. (**a**) No abnormalities, (**b**) tonic activity, and (**c**) phasic activity

Table 8.1 Breakdown of epochs labeled by a clinical laboratory technician

Decision result	Epoch number
No abnormalities	1233
Tonic activity	664
Phasic activity	197
Total	2094

presents an example of the results of the RWA inspection decisions made by the clinical laboratory technician. Muscle activity was not observed in the electromyographic waveforms where RWA was not expressed, whereas the electromyographic waveforms where RWA was expressed exhibited intense muscle activity, even during REM sleep. Next, a breakdown of the epochs labeled by the clinical laboratory technician are shown in Table 8.1.

8.4.2 Pre-processing of Time-Series Data

It is desirable that the data used have no individual differences between subjects when discriminating between time-series data using machine learning. However, as the data used in this experiment were time-series data of surface electromyograms, the amplitude fluctuations were influenced by muscle mass, subcutaneous fat thickness, and electrical resistance of the skin. Hence, the preprocessing method that we implemented for the time-series data is shown below:

I. The epoch with the smallest variance in the non-REM sleep period was extracted and then normalized by subtracting the average value.
II. A value that was twice the standard deviation of the epoch extracted from I was calculated.
III. Each epoch during REM sleep was normalized by subtracting the average value.
IV. The time-series data for each epoch during REM sleep was divided by the value calculated in II.

A typical example of the epoch waveform before and after pre-processing is presented in Fig. 8.2. An example of the pre-processing applied to that shown in Fig. 8.2a is presented in Fig. 8.2b, and an example of the pre-processing applied to that shown in Fig. 8.2c is presented in Fig. 8.2d.

Furthermore, an average rectified value (ARV) is often used for the pre-processing of surface electromyograms. ARV is a waveform that is obtained by taking the absolute value from the signal amplitude and smoothening it by integrating (or applying a low-pass filter) over a given time range. A particular benefit of ARV lies in the fact that the muscle activity occurring in the surface electromyogram is more directly expressed than in the original waveform. This may make the characteristics of phasic activity more prominent during its evaluation. Hence, we also investigated cases where ARV processing was performed on each epoch with a window width of

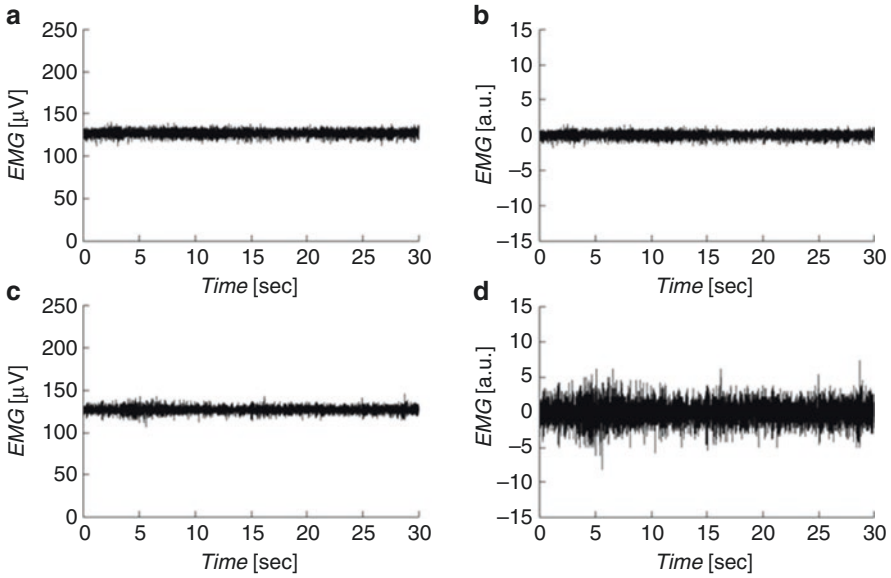

Fig. 8.2 Typical examples of epoch waveforms before and after pre-processing. (**a**) No abnormalities (without preprocessing), (**b**) No abnormalities (with preprocessing), (**c**) Tonic activity (without preprocessing), and (**d**) Tonic activity (with preprocessing)

0.2 s. A typical example of an epoch waveform before and after ARV is presented in Fig. 8.3. An example of an ARV applied to Fig. 8.3a is presented in Fig. 8.3b, and an example of an ARV applied to Fig. 8.3c is presented in Fig. 8.3d.

8.4.3 SVM and CNN Parameter Settings

We focused on the basic statistics of the time-series data for the feature extraction used in SVM. The following 10 items were calculated for the basic statistics of each epoch during REM sleep: mean value, sample variance, sample standard deviation, median value, mode, kurtosis, skewness, minimum value, maximum value, and total value. The parameters that need to be adjusted when using SVM were determined through Bayesian optimization [26], and the number of parameter searches was set to 200 (Table 8.2).

Each epoch during REM sleep was converted to grayscale image data for the feature extraction in the CNN. The size of the image data was set at 64 × 98 pixels (6272 dimensions), and the vertical axis, horizontal axis, and axis labels were excluded from the image data. Parameters that needed to be adjusted when using CNN were determined through Bayesian optimization, and the number of parameter searches was set to 200 (Table 8.3).

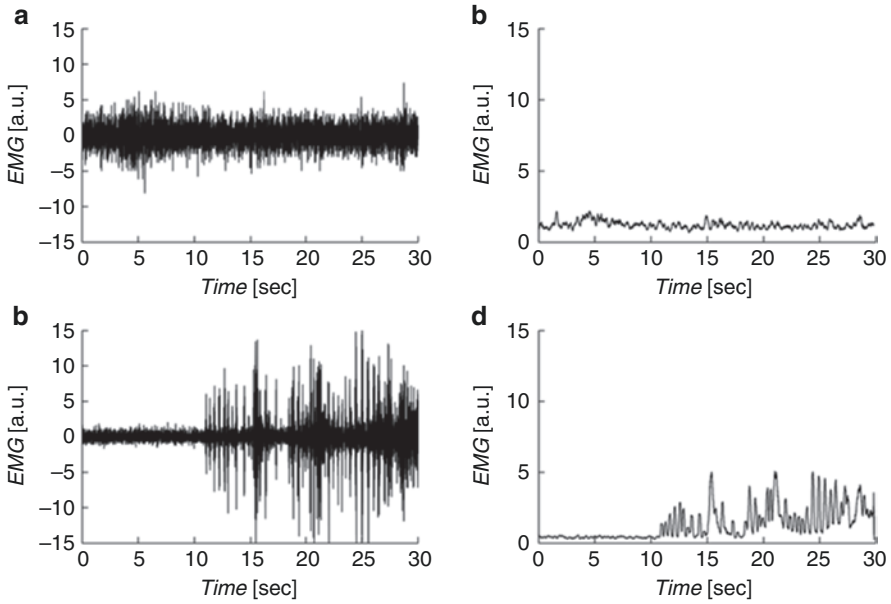

Fig. 8.3 Typical example of epoch waveform before and after ARV. (**a**) Tonic activity (without ARV), (**b**) Tonic activity (with ARV), (**c**) Phasic activity (without ARV), and (**d**) Phasic activity (with ARV)

Table 8.2 Search range of SVM parameters based on Bayesian optimization

Parameter	Search range
C (Misjudgment tolerance)	10^{-2}, 10^{-1}, 1, 10, 10^{2}, 10^{3}
γ (Weight on individual learning data)	10^{-2}, 10^{-1}, 1, 10, 10^{2}, 10^{3}

Table 8.3 Search range of CNN parameters based on Bayesian optimization

Parameter	Search range
Number of filters	Integer value from 10 to 50
Filter size	Integer value from 10 to 50
Mini-batch size	32, 64, 128
Dropout ratio	Real number between 0.1 and 0.9
Optimization algorithm	Momentum SGD, Adam, MSVAG, SMORMS3

The SVM and CNN discrimination accuracy was calculated by extracting a single subject as a test case and setting the remaining 11 subjects as learning cases to perform cross-validation with all the subjects, with each acting as a test case once. The RWA discrimination accuracy (recall ratio, precision, and F value) calculated from each subject when using SVM is presented in Table 8.4. The F value was the maximum when using the basic statistics after ARV as feature values in RWA

Table 8.4 RWA discrimination accuracy by SVM (Average ± SD)

		Recall ratio (%)	Precision (%)	*F* value (%)
Tonic activity	Basic statistics	72.8 ± 28.1	61.0 ± 27.4	57.6 ± 27.3
	Basic statistics (ARV)	74.7 ± 20.9	70.1 ± 29.4	65.5 ± 21.8
Phasic activity	Basic statistics	29.6 ± 33.4	34.9 ± 37.0	27.2 ± 29.0
	Basic statistics (ARV)	44.0 ± 33.7	41.9 ± 34.2	38.1 ± 27.6

Table 8.5 RWA discrimination accuracy by CNN (Average ± SD)

		Recall ratio (%)	Precision (%)	*F* value (%)
Tonic activity	Electromyographic waveform image	85.0 ± 13.7	77.0 ± 22.6	78.1 ± 16.2
	Electromyographic waveform image (ARV)	78.4 ± 14.0	82.4 ± 17.2	78.7 ± 11.6
Phasic activity	Electromyographic waveform image	56.0 ± 30.2	63.4 ± 33.9	54.6 ± 25.5
	Electromyographic waveform image (ARV)	69.3 ± 22.1	74.0 ± 25.8	67.1 ± 18.6

discrimination using SVM. Next, the RWA discrimination accuracy calculated from each subject when using CNN is presented in Table 8.5. The *F* value was also the maximum when using the image data after ARV as feature values in RWA discrimination using CNN.

8.4.4 RBD Prevalence Using Discriminant Analysis

Discriminant analysis was utilized to estimate prevalence. It involved assessing whether the data of the patient and non-patient group could be accurately classified using the evaluation indices of the two machine learning methods. Discriminant analysis is a method that estimates the group to which an unknown sample belongs when the group to which a certain sample belongs is already known. Discriminant analysis derives discriminants based on the distribution of known samples and estimates the most likely group to which the sample to be estimated belongs by applying its attribute values to the discriminant. The RWA occurrence frequency in subjects diagnosed with RBD was calculated using each RWA discriminator with the maximum F value for SVM and CNN (Fig. 8.4). Next, a similar index was calculated for the 13 subjects for whom PSG was implemented but RBD was not diagnosed, and discriminant analysis was conducted using the Mahalanobis distance measure [27]. The discriminant analysis results are presented in Table 8.6. Estimates of RBD prevalence using SVM resulted in the misjudgment of one subject in the patient group and two subjects in the non-patient group. Meanwhile, estimates of RBD prevalence using CNN resulted in misjudgment of zero subjects in the patient group and two subjects in the non-patient group.

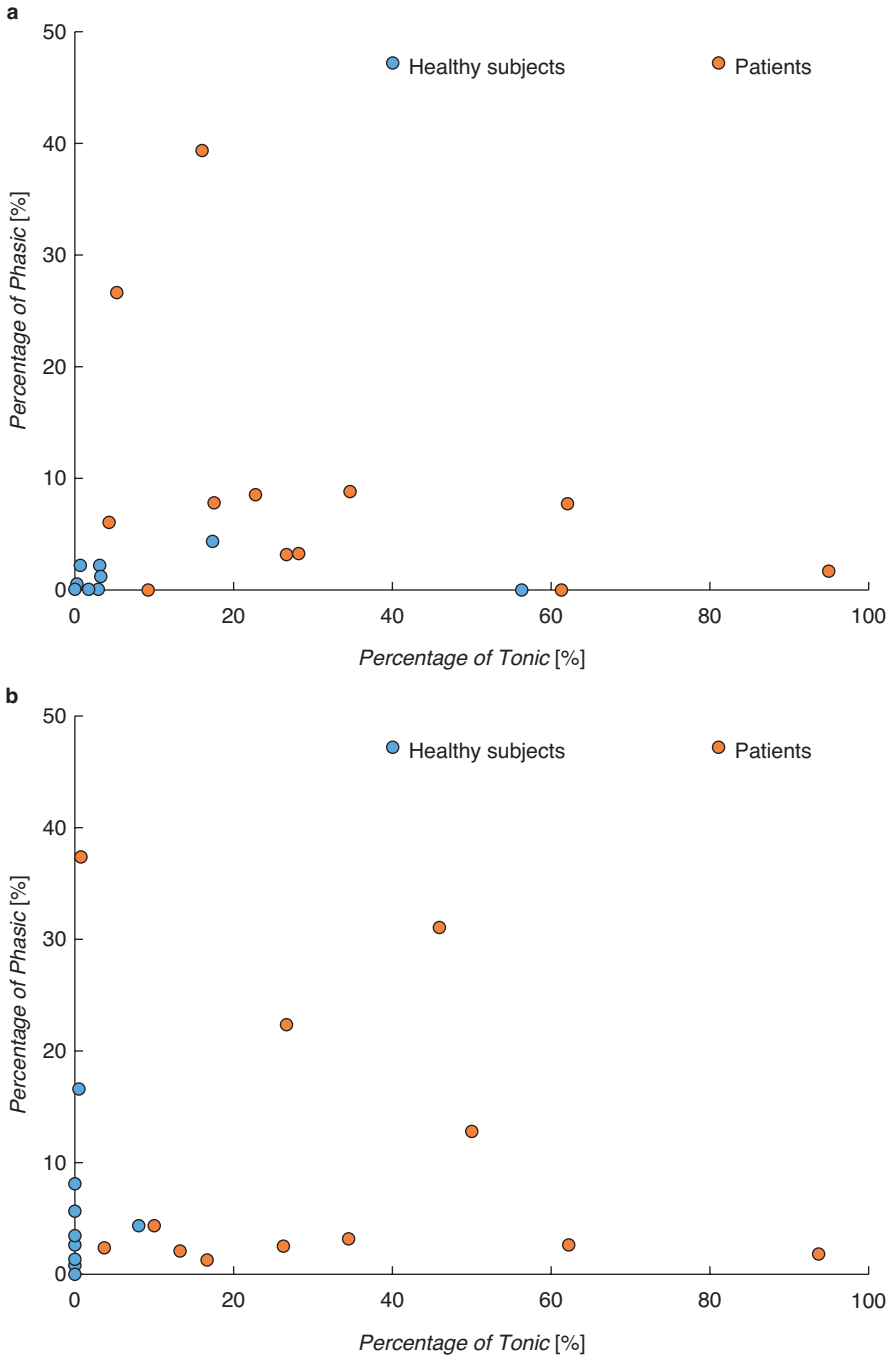

Fig. 8.4 RWA occurrence frequency using each discriminator. (**a**) SVM and (**b**) CNN

Table 8.6 Number of erroneously detected persons

Number of misjudgments	SVM	CNN
Patients	1/12	0/12
Healthy subjects	2/13	2/13

8.5 Conclusions

Because PSG requires specialized staff and large-scale equipment, there is a limited number of facilities that can implement it. However, we could extract extremely meaningful information from the PSG very well by attempting to understand sleep physiology and pathophysiology and interpreting PSG data with the appropriate methods. When PSG is used for the diagnosis of sleep disorders, the reading and interpretation of recorded data are performed by clinical laboratory technicians. However, there may be variation in the results obtained by the clinical laboratory technicians in charge of inspection decisions, and these decisions also require large amounts of time and experience. In this chapter, we introduced the automatic PSG analysis methods that we have implemented, with a focus on RBD, a form of parasomnia. Methods that used CNN, which is a type of deep learning, resulted in the misjudgment of zero and two individuals in the patient and non-patient groups, respectively, when estimating the prevalence of RBD in 25 individuals. The prevalence estimation based on our proposed automated algorithm is thought to be effective as a form of primary screening for RBD. Patients require hospitalization for 2 days and one night when conducting PSG at a sleep center, and expenses can be high. Furthermore, as very expensive measurement equipment is needed for PSG, there are a limited number of people who can be examined at a single time. Advances in automated algorithms are believed to be beneficial for the estimation of RBD prevalence at home as well, and we expect that these algorithms will be applied to simple PSG results that will be measured using wearable devices in the next step.

References

1. Kojima M, Wakai K, Kawamura T, Tamakoshi A, Aoki R, Yingsong L, et al. Sleep patterns and total mortality: a 12-year follow-up study in Japan. J Epidemiol. 2000;10:87–93.
2. Goto A, Yasumura S, Nishise Y, Sakihara S. Association of health behavior and social role with total mortality among Japanese elders in Okinawa. Jpn Aging Clin Exp Res. 2003;15:443–50.
3. Amagai Y, Ishikawa S, Gotoh T, Doi Y, Kayaba K, Nakamura Y, et al. Sleep duration and mortality in Japan: the Jichi medical school cohort study. J Epidemiol. 2004;14:124–8.
4. Mesas AE, López-García E, León-Auñoz LM, Guallar-Aastillón P, Rodríguez-Artalejo F. Sleep duration and mortality according to health status in older adults. J Am Geriatr Soc. 2010.
5. Kronholm E, Laatikainen T, Peltonen M, Sippola R, Partonen T. Self-reported sleep duration, all-cause mortality, cardiovascular mortality and morbidity in Finland. Sleep Med. 2011;12:215–21.
6. Lange T, Perras B, Fehm HL, Born J. Sleep enhances the human antibody response to hepatitis a vaccination. Psychosom Med. 2003;65:831–5.

7. Matsumoto Y, Mishima K, Satoh K, Tozawa T, Mishima Y, Shimizu T, et al. Total sleep deprivation induces an acute and transient increase in NK cell activity in healthy young volunteers. Sleep. 2001;24:804–9.
8. Ohayon MM, Carskadon MA, Guilleminault C, Vitiello MV. Meta-analysis of quantitative sleep parameters from childhood to old age in healthy individuals: developing normative sleep values across the human lifespan. Sleep. 2004;27:1255–73.
9. Aserinsky E, Kleitman N. Regularly occurring periods of eye motility, and concomitant phenomena, during sleep. Science (80-). 1953;118:273–4.
10. Dement W, Kleitman N. Cyclic variations in EEG during sleep and their relation to eye movements, body motility, and dreaming. Electroencephalogr Clin Neurophysiol. 1957;9:673–90.
11. Kim K, Uchiyama M, Okawa M, Liu X, Ogihara R. An epidemiological study of insomnia among the Japanese general population. Sleep. 2000;23:41–7.
12. Yaremchuk K. Sleep disorders in the elderly. Clin Geriatr Med. 2018;34:205–16.
13. Miyamoto T, Miyamoto M, Iwanami M, Kobayashi M, Nakamura M, Inoue Y, et al. The REM sleep behavior disorder screening questionnaire: validation study of a Japanese version. Sleep Med. 2009;10:1151–4.
14. Japan Society of Neurovegetative Research. Autonomic nervous function test. 5th ed. Tokyo: Bunkodo; 2007. (in Japanese)
15. Japanese Society of Sleep Research. Suimingaku (sleep research). Tokyo: Asakura (in Japanese); 2009.
16. Kryger MH, Roth T, Dement WC. Principles and practice of sleep medicine. Princ Pract Sleep Med. 2005.
17. Rundo JV, Downey R. Polysomnography. Handb Clin Neurol. 2019.
18. Kales A, Rechtschaffen A. A manual of standardized terminology, techniques and scoring system for sleep stages of human subjects. Los Angeles, BIS/BRI, UCLA, 1968.
19. Iber C, Ancoli-Israel S, Chesson A, Quan SF. The AASM manual for the scoring of sleep and associated events: rules. Terminology and Technical Specification. J Clin Sleep Med. 2007.
20. Berry RB, Albertario CL, Harding SM, for the American Academy of Sleep Medicine, et al. The AASM manual for the scoring of sleep and associated events: rules, terminology and technical specifications, version 2.5. American Academy of Sleep Medicine: Darien, IL; 2018.
21. Lotharius J, Brundin P. Pathogenesis of Parkinson's disease: dopamine, vesicles and α-synuclein. Nat Rev Neurosci. 2002;3:932–42.
22. Lapierre O, Montplaisir J. Polysomnographic features of REM sleep behavior disorder: development of a scoring method. Neurology. 1992;42:1371–4.
23. Frauscher B, Iranzo A, Gaig C, Gschliesser V, Guaita M, Raffelseder V, et al. Normative EMG values during REM sleep for the diagnosis of REM sleep behavior disorder. Sleep. 2012;35:835–47.
24. Kinoshita F, Takada H, Nakayama M. A study on classification algorithm of REM sleep behavior disorder. Electron Commun Jpn. 2019;102:9–14.
25. Miyanaga K, Kinoshita F, Touyama H, Nakayama M. A deep learning based approach for the classification algorithm of REM sleep behavior disorder. In: Paper presented at the 18th International Conference on Machine Learning and Cybernetics (ICMLC), Kobe Convention Center, Kobe, July 2019.
26. Snoek J, Larochelle H, Adams RP. Practical Bayesian optimization of machine learning algorithms. Adv Neural Inf Process Syst. 2012. 2951–9.
27. McLachlan GJ. Mahalanobis distance. Resonance. 1999;4:20–6.

Chapter 9
Stabilometry

Hiroki Takada, Rentarou Ono, Kohki Nakane, Fumiya Kinoshita, and Meiho Nakayama

Abstract It had taken a long while for the stabilometry to be established for the measurement of the center of gravity of the body and its motion process. The stabilometry is of interest not only in the otolaryngology but also in various scientific fields such as the rehabilitation studies, the sports science, and the space medicine. In this chapter, the application and the theoretical description are also given to show the future possibility. Moreover, the generative adversarial network (GAN) is also introduced to conduct the numerical analysis of the body sway, and we propose a new type of the diagnostic assistance technology and a novel method with use of the artificial intelligence (AI) and deep learning in these fields.

Keywords Stabilometry · Righting reflex · Stabilometer · Statokinesigram (SKG) Stabilogram · Stochastic differential equation (SDE)

9.1 Introduction

In the Chap. 2, Electrocardiogram (ECG) is introduced in detail, however, Willem Einthoven W., who was a Dutch physiologist, invented the first practical ECG in 1895. He received the Nobel Prize in Physiology or Medicine in 1924 for the discovery of the mechanism of the electrocardiogram [1, 2]. It was known that the beating of the heart produced electrical currents, but the instruments of the time

H. Takada (✉) · R. Ono · K. Nakane
Department of Human and Artificial Intelligence, University of Fukui, Fukui, Japan
e-mail: takada@u-fukui.ac.jp

F. Kinoshita
Faculty of Engineering, Department of Electrical and Computer Engineering, Toyama Prefectural University, Toyama, Japan

M. Nakayama
Good Sleep Center and Department of Otolaryngology, Nagoya City University, Nagoya, Japan

H. Takada, K. Yokoyama (eds.), *Bio-information for Hygiene*, Current Topics in Environmental Health and Preventive Medicine,
https://doi.org/10.1007/978-981-15-2160-7_9

could not accurately measure this phenomenon without placing electrodes directly on the heart. Development for the bioinstrument became a footprint in our human history.

Stabilometry is known to be a test for the equilibrium function, which is useful for overall evaluation of the stability in the standing posture and diagnosis of the equilibrium function disorder. The postural sway is observed during the stabilometry included in the medical treatment fee as a test method to diagnose vertigo, dizziness, and imbalance. A body equilibrium function test procedure, termed stabilometry, is considered useful in comprehensively evaluating the equilibrium function. Stabilometry is typically performed with a subject involuntary standing in Romberg's posture, in which the feet are together. Sways of the CoP are measured for 60 s at a time with their eyes closed after the test with their eyes open. It is an unstable standing position because the base of support is narrow, so body sway becomes marked, and a reduced equilibrium function is likely to be evident in statokinesigrams (SKGs)/stabilograms. In our previous study, we often investigate the control system under unstable conditions. We have developed an apparatus for adjusting the tilt angle on the slope on which the body sway is recorded. As a side note, otolaryngologists distinguish between SKGs and stabilograms that are defined in the Sect. 9.3.

The stabilometer has been developed as a clinical device for evaluating body balance function [3], but its history is long. In 1380, the center of gravity (CoP) in human was statically recorded by Borreli [4], who measured where the CoP was by putting a corpse on a board [5]. In the twentieth century, the motion process of the CoP was tried to measure as scale weight fluctuations with standing upright, on spring scales. Whereas Basler had been succeeded in measuring one-dimensional motion process of the CoP in 1928 [6], Travis has been reported simultaneous measurement of the lateral and the anterior/posterior [7]. The pressure sensor (strain gauge) currently used for measuring the CoP has been developed in 1964 [8]. Now that the pressure can be measured electrically, the body sway can be displayed on the oscilloscopes. In recent years, the development of highly precise electrical devices has advanced body balance function tests [9]. Regarding stabilometers for evaluating static body balance, many analysis methods have been improved as a result of progress in device accuracy and computer software.

Motion process of the CoP is important not only on clinical diagnosis [10] but also elucidation of the human system to control a standing upright as a two-legs robot [11]. The body sway is observed with his/her upright posture which can be involuntarily kept by the iteration of reflexes. This posture is originally in defiance of gravity, and it is easy to fall down, however, the righting reflex, also known as the labyrinthine righting reflex, corrects the body deviation when it is taken out of its normal upright position. The head will be resulted to move back into position as the rest of the body follows. Measurement methods and analytical indices of SKGs have been proposed to increase the diagnostic value of stabilometry [12]. The analytical indices include the total length of body sway and the locus length per unit area. The latter is considered to represent micro changes in postural control and to serve as a scale of proprioceptive postural control.

As mentioned above, the stabilometry is basically conducted with subjects' eyes open and their eyes closed. Compared to the Romberg test (RT), our equilibrium function and/or system to control the upright posture can be evaluated more quantitatively in detail since this condition is performed by the same way as in the RT [13]. The method of the stabilometry is indicated in the following Appendix as a test guide of the Japanese Society for Equilibrium Research.

In the past, it was defined how many centimeters on a recording paper should be recorded as the deviation of 1 cm in the center of gravity. For X–Y recording, it is appropriate that displacement on the SKG is consistent with the deviation of 1 cm. Thus, calibrations and/or accuracy of the stabilometer are required to measure the body sway in the clinical test and the research for the equilibrium function. For instance, stabilometers made by Anima Co. Ltd. (Fig. 9.1) are reliable inspection devices that were confirmed to Japanese Industrial Standards (JIS) with high accuracy. The stabilometer is a clinical device currently used for the stabilometry with insurance indication. A certain accuracy is required in order to use the stabilometers in clinical tests. Therefore, stabilometers were registered Japanese Industrial Standards (JIS) as *T-1190-1987* in 1987 by the Japanese Society for Equilibrium Research (JSER) [14], and the stabilometry was authorized as stabilometer examination in 1994. A medical stabilometer came to be used as an apparatus for the stabilometry widely afterward in the clinical fields and posted in a medical fee table in Japan. According to the JIS, the stabilometers are required to measure in the following conditions:

1. A subject with a weight of 10 kg to 150 kg.
2. Within ±1 mm as an error of the center of gravity.
3. The free vibration frequency > 20 Hz.
4. Within ±1 mm as drift characteristics after 30 and/or 60 min.

In 2015, the Japanese society for equilibrium research reported on the accuracy of the clinical gravicorder [15]. At that time, the calibration device made by the abovementioned company is also used to survey the accuracy of stabilometers.

As stated above, SKGs are recorded in Romberg's posture, which is an upright posture with the feet placed together. This posture is unstable with a small support area so that deterioration in the equilibrium function can be detected. Static stabilometry has been applied to the following instability involved in the system to control upright postures in their natural standing.

1. In the body tracking test (BTT), dynamic equilibrium function is qualitatively evaluated by the blindfolded vertical writing and stepping tests for directional deviation, which is also called Unterberger-Fukuda [16] stepping test. Compared with the Gait Test, this clinical way is also widely conducted in Japan today because it saves space. The deviation of direction is ascertained more easily by it than by other static standing tests such as Romberg's, Mann's, or Flounier's tests. Yasuda and Utamura (1970) have found that its greater sensitivity to deviation phenomenon in comparison with that of the other tests. They also observed remarkable deviation to the opposite side of the canal paresis (CP) [17].

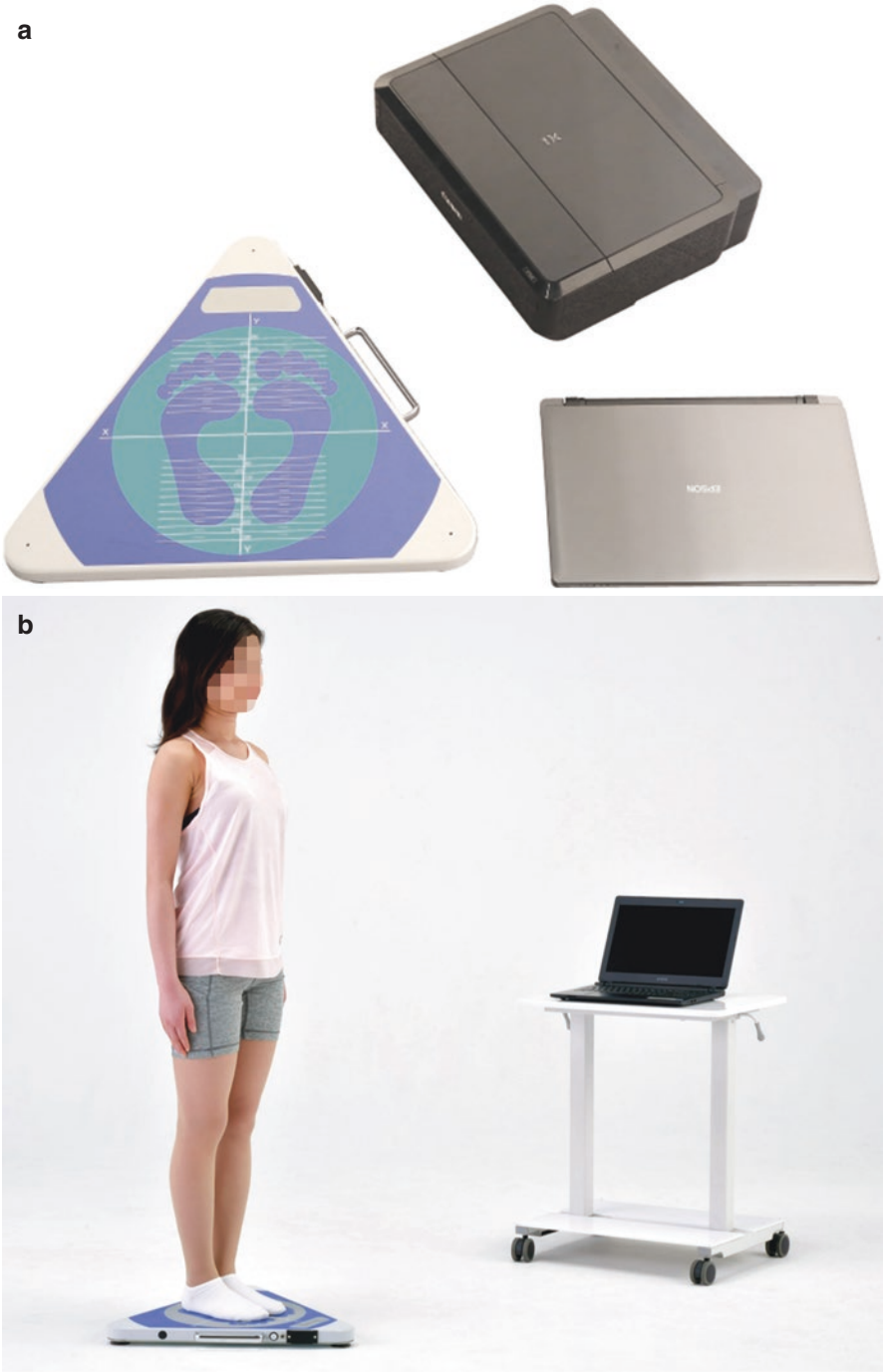

Fig. 9.1 Gravicorders; gravicorders made by Anima Co. Ltd. (Tokyo, Japan) (**a**), experimental landscape (**b**)

Moreover, the BTT using visual stimulation has been developed as a new method for stimulus evaluation using a stabilometer for dynamic body balance evaluations [9, 18, 19].

2. The Galvanic body sway test (GBST) can also be performed as a vestibular stimulus evaluation. Typical electrode arrangements are illustrated in [20]. By placing an electrode on each mastoid (one positive and one negative), medial-lateral sway and horizontal/torsional eye movement can be produced by stimulating both labyrinths in opposite directions simultaneously. An alternate electrode configuration allows the method to assess each labyrinth separately, which can now be accomplished only with caloric testing. Galvanic vestibular stimulation (GVS) is performed by applying small electrical currents to the vestibular labyrinth using electrodes while recording either eye movements [21] or postural sway [22–24]. In most cases, subjects stand with their eyes closed. It is easy to observe the response to the GSV by averaging the outputs from the stabilograms because their variations in the body sway are small. Using the monopolar rectangular wave and the bipolar rectangular wave, DC stimulations are applied to subjects. In our experiments, the later electrical stimulation was used [25–28]. SKGs of the elderly were compared with those of the young stimulated by the electrical stimulation [25, 26], and we examined whether deterioration of the equilibrium function with advancing age could be simulated by applying the electrical stimulation to subjects. Theoretical expression has been stated in [28], which is corresponding to the Sect. 9.3.

9.2 Stereopsis

When users viewed moving pictures on liquid crystal displays (LCDs), they experienced a visually induced motion sickness that was caused by a disagreement between the visual stimulation and the stimulation of the inner ear [29]. The blurred images on the LCDs sometimes induced “image sickness” in viewers, which is an unpleasant feeling that is similar to motion sickness. Significant increases in the postural sway were observed during the image sickness induced by simulator [30]. We have studied several contents of the instability of human control system [31]. Physiological mechanism of the motion sickness had been explained in detail [31] in addition to the evidence of the possibility to evaluate the severity of the motion sickness by conducting the stabilometry.

9.2.1 Our Discovery in Previous Studies

We have reported on some findings obtained by comparing fixation distances between accommodation and convergence in young and middle-aged subjects while they viewed 2D and 3D video clips [31]. In these studies, measurements were made

by our combination of apparatuses, and 2D and 3D video clips were presented through a liquid crystal shutter system. As a result, subjects' accommodation and convergence were found to change the diopter value periodically when viewing 3D images. An important result is that, when subjects are young, accommodative power while viewing 3D images is similar to the distance of convergence, while subjects are middle-aged, their accommodation is weak. This result denies the hypothesis that the motion sickness induced by 3D video clips is caused by the sensory conflict as a disagreement between convergence and visual accommodation. The motion sickness induced by 3D video clips might be caused by the sensory conflict as a disagreement between visual and vestibular inputs. However, this disagreement should be examined more carefully in future studies.

The motion sickness induced by 3D video clips might be caused by the sensory conflict as a disagreement between visual and vestibular inputs as follows. We have reported that the VIMS could be detected with the total locus length and sparse density, which were used as analytical indices of SKGs. We showed an analysis of the severity of motion sickness induced by 3D video clips on an LCD compared to that induced by viewing the video clips on an head-mounted display (HMD), and discussed on the body sway models [32]. We measured the body sway in the controlled trial and during exposure to a conventional 3D film on an LCD and an HMD. Friedman's tests showed the main effects in the above-mentioned indices for the SKGs. Multiple comparisons revealed that viewing the 3D film on the HMD significantly affected the body sway, despite a large visual distance. Hence, there are factors of stereoscopic images inducing motion sickness except for the size of displays.

We could not evaluate the severity of the VIMS while viewing 3D video clip but have succeeded in observing significant instability after the tests with their eyes open. On the detection stand of a stabilometer (G5500; Anima Co., Ltd.) in the Romberg posture, we measured body sway quantitatively during the controlled trial, exposure to a 3D movie on an LCD, and that on an HMD, which is widely spread in use due to advantages of being individually wearable, and providing views of a wide visual angle [31].

9.2.2 Effects of Low/High-Definition Stereoscopic Video Clips

We investigated the effects of low/high-definition 3D video clips on the human body. In this experiment, we measured the body sway and recorded a SKG from which the severity of the VIMS could be estimated. The brain function, especially in the hemodynamics in the CBF, was also measured.

Biometric data were obtained for the center of pressure (CoP), heart rate variability, and hemodynamics on the surface of the cerebrum in 11 healthy young individuals (mean ± standard deviation: 22.6 ± 1.0 years) with no abnormalities in the extremities and no past medical history of ear or nervous system disease. Moreover, the visual acuity of subjects with the naked eye and/or contact lenses had

to be greater than 0.8 and capable of stereoscopic vision. The experiment was fully explained to the subjects beforehand, and written consent was obtained. In this study, subjects wore a head-mounted display (HMD) GOOVIS G2 (Lets-co.jp, Nagoya), and the following video clips (VCs) were projected to the HMD:

VC1) stereoscopic video clip with a resolution of 1080p.
VC2) stereoscopic video clip with a resolution of 360p.

The displayed content was supplied by Sky Crystal (Olympus Memory Works Ltd. Co., Tokyo), which was modified with the company's permission and was used as the visual stimulus in this experiment. A sphere was ambulated in a video clip in a complex manner.

Biometric data such as the SKG, electrocardiogram (ECG), and oxy-/deoxygenated hemoglobin concentrations on the cerebrum blood flow were recorded while the participant viewed high-resolution video clip VC1 and low-resolution video clip VC2. Each sway of the CoP was recorded at a sampling frequency of 100 Hz. The subjects were instructed to maintain the Romberg posture during the duration of the trials. The subjects were asked to use peripheral vision for VC1 for the first 60 s and VC2 for the next 60 s, and to stand when there were no images (resting state). The stabilometry was conducted by using a Wii balance board (Nintendo, Kyoto). This trial was repeated five times.

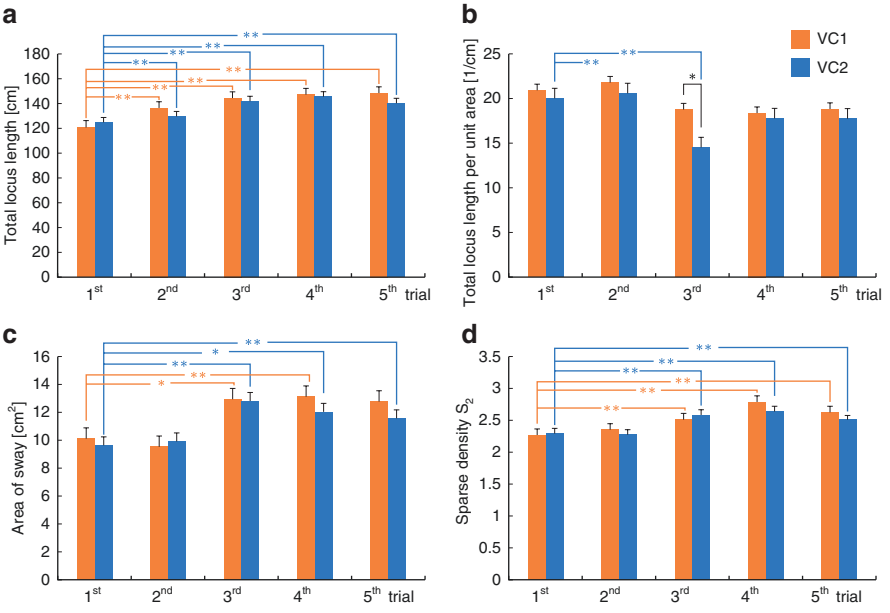

Fig. 9.2 Comparison of sway values while viewing VCs for each trial; total locus length (**a**), area of sway (**b**), total locus length per unit area (**c**), and sparse density S_2 (**d**), Changes in oxygenated hemoglobin concentration in the cerebrum blood flow recorded while viewing the VC2 compared to that while viewing the VC1 (**e**). *Statistical significant difference ($p < 0.1$), **Statistical significant difference ($p < 0.05$)

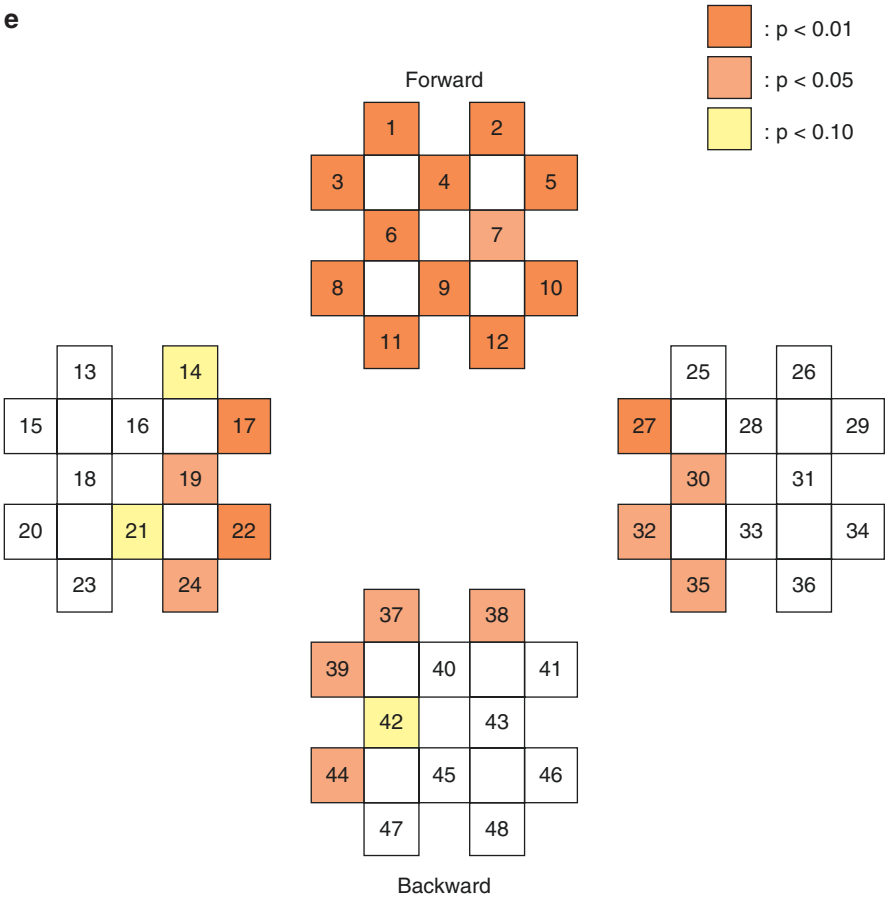

Fig. 9.2 (continued)

For NIRS, the LABNIRS (Shimadzu, Kyoto) was used. Channels were arranged as follows: 1–12 ch on the frontal lobe, 13–24 ch on the left temporal lobe, 25–36 ch on the right temporal lobe, and 37–48 ch on the occipital lobe (Fig. 9.2a). Results would be stated in the next section.

9.2.3 Simultaneous Measurement with fNIRS

Sway values such as the area of sway, total locus length, total locus length per unit area, and sparse density [33, 34] were estimated from the SKGs. By using the Wilcoxon signed-rank test, we compared the sway values while viewing the VCs for a trial as follows. The statistical significance was herein set to be 0.05.

As shown in Fig. 9.2a–d, there was no statistical significance in the difference between the sway values while viewing the VCs during the trials except for Fig. 9.2c. In the third trial, the total locus length per unit area while viewing VC1 tended to be different from that while viewing VC2 ($p < 0.1$). For the total locus length (Fig. 9.2a), area of sway, and sparse density (Fig. 9.2d), the sway values for the n-th trial ($n = 3$, 4, 5) were significantly greater than those for the first trial while viewing VC1 ($p < 0.05$). In addition, all sway values for the n-th trial ($n = 3$, 4, 5) were significantly greater than those for the first trial while viewing VC2 ($p < 0.05$).

No statistical differences were observed between the sway values while viewing the high-resolution video clip (VC1) and those while viewing the low-resolution video clip (VC2). The VIMS did not result from differences between the resolutions in this study. In addition, there was a statistical significance between the sway values of the n-th trial and those of the first trial ($n = 3$, 4, 5) while viewing any video clip. The changes in the sway values were considered to be owing to acclimatization in the upright posture.

The oxygenated hemoglobin concentration in the cerebrum blood flow recorded while viewing VC2 was compared to that while viewing VC1. Significant changes were observed in the frontal lobe, temporal lobe, and upper occipital lobe (Fig. 9.2e).

According to the fNIRS measurement, significant changes were observed in the temporal lobe and upper occipital lobe that corresponded to the ventral and dorsal streams, respectively [35, 36]. It is difficult to recognize the visual objects and motion processes owing to the low resolution of the video clip. Activity in the ventral and dorsal streams was enhanced, and their cooperativeness might be expected to be found in the next step.

9.3 Mathematical Model

Stabilograms are graphs of time series data that are obtained from the projection of the motion process on the SKG to each X- or Y-axis. In the SKG, variables x and y are regarded to be independent [37]. The linear stochastic differential equation (Brownian motion process) has been proposed as a mathematical model to describe body sway [38–40]. To describe the individual body sway, we especially show that it is necessary to extend the following nonlinear stochastic differential equations:

$$\frac{\partial x}{\mathrm{d}t} = -\frac{\partial}{\partial x} U_x(x) + \mu_x w_x(t), \tag{9.1}$$

$$\frac{\partial y}{\mathrm{d}t} = -\frac{\partial}{\partial y} U_y(y) + \mu_y w_y(t), \tag{9.2}$$

where $w_x(t)$ and $w_y(t)$ represent the white noise [41]. We can herein consider the physiological reason why the noise terms are included in these equations. It might

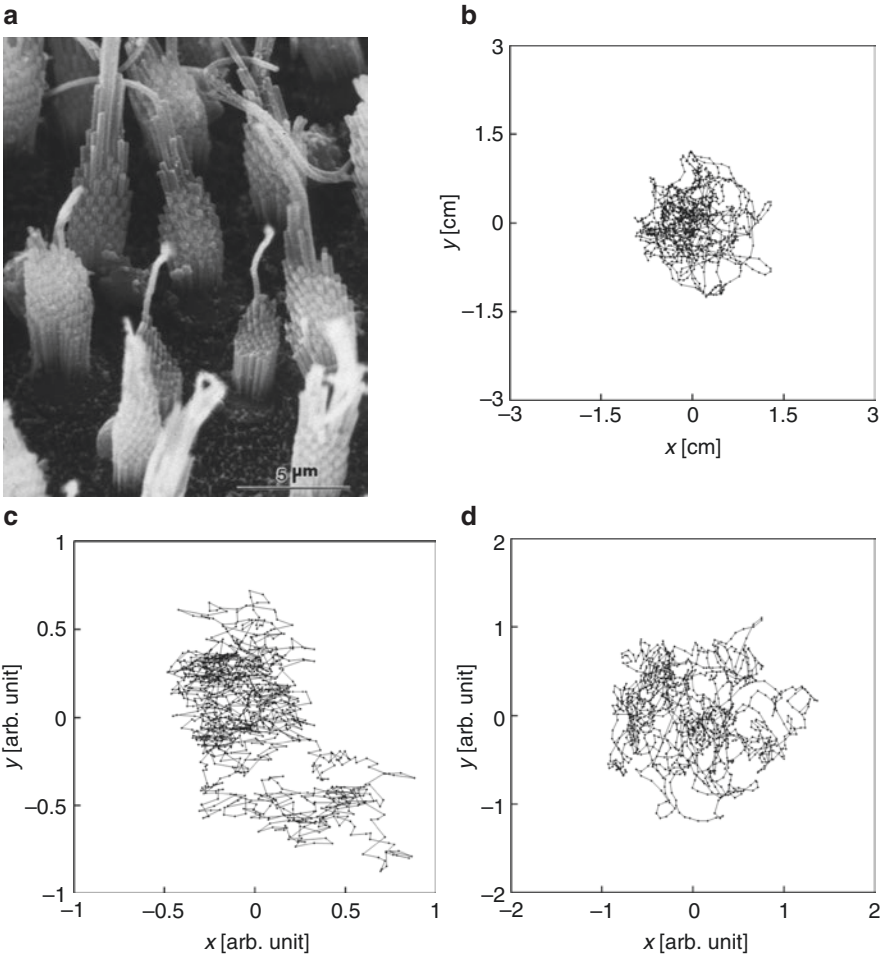

Fig. 9.3 Evidence and results in numerical simulations of the body sway; electron micrograph of hair cells on the sensory epithelium of the otolithic organ (**a**), a typical SKG observed a young healthy man (**b**), a typical result of the numerical simulation derived from the Gaussian white noise (**c**), a typical result of the numerical simulation derived from the pink noise (**d**)

be caused by the stereocilia and especially the kinocilium pointing in random directions on the otoliths (Fig. 9.3). The following formula describes the relationship between the distribution in each direction, $G_x(x)$, $G_y(y)$, and the temporal averaged potential constituting the stochastic differential equations (SDEs):

$$U_x(x) = -\frac{\mu_x^2}{2} \ln G_x(x) + \text{const.}, \tag{9.3}$$

$$U_y(y) = -\frac{\mu_y^2}{2} \ln G_y(y) + \text{const.} \tag{9.4}$$

The variance of stabilograms generally depends on the temporal averaged potential function (TAPF) with several minimum values when it follows the Markov process without abnormal dispersion. SDEs can represent movements within local stability with a high-frequency component near the minimal potential surface, where a high density at the measurement point is expected.

Histograms of the stabilograms were obtained from each stabilogram. Mean of each stabilogram was set to (0, 0) by statistical processing. We compared histograms that were composed of all subjects' stabilograms with eyes open. The TAPFs in viewing 2D and 3D video clips were determined from the histograms using

$$\widehat{U_x}\left(x\right) = a_x x^4 + b_x x^3 + c_x x^2 + d_x x, \tag{9.5}$$

$$\widehat{U_y}\left(y\right) = a_y y^4 + b_y y^3 + c_y y^2 + d_y y. \tag{9.6}$$

The TAPFs were herein regressed by these polynomials of degree 4. SDEs were derived from Eqs. (9.1) and (9.2), the mathematical model of the body sway, into which was substituted the Eqs. (9.5) and (9.6), respectively. These SDEs were rewritten into the difference equations, and numerical solutions were obtained with the Runge–Kutta formula as the numerical calculus. The pseudo-random numbers (mean ± standard deviation, 1 ± 1) were generated by Mersenne Twister method [42]. Box-Muller transformation was performed to substitute the white Gaussian noise into the second terms, the noise terms, on the right-hand side of the difference equations [43]. Moreover, we have performed inverse Fourier-transformation of 1/*f*-like power spectrum to generate the pink noise, which is considered to be appropriate to the numerical simulation of the body sway because 1/*f*-like fluctuation has been also found in the biosignal [44–47]. This pink noise was substituted for the noise terms instead of the white Gaussian noise as described previously.

The noise amplitude μ and time step Δt were set to be every 0.1 step from 0.1 to 1.0 and 0.01 step from 0.05 to 0.40, respectively. Numerical analysis was employed for 11,200 steps, and the first 10,000 steps of the numerical solutions were discarded due to dependence of the initial value (x, y) = (0, 0). Any pseudo numbers were standardized so that their means and standard deviations became 0 and 1, respectively.

In our previous research, numerical solutions were evaluated using the area of sway, total locus length, and the statistical indices for the distribution of the displacement x or y such as the standard deviation, the skewness, and the kurtosis [31, 48]. The numerical solutions were herein evaluated using the following nonlinear analysis:

1. According to the Wayland algorithm, translation error (E_{trans}) is calculated in these numerical solutions. We can measure the degree of the determinism involved in the mathematical model generating the time series. Translation error (E'_{trans}) is also calculated in sequences of the temporal differences of the numerical solutions. Low frequency and/or trend components are expected to be

removed by the mathematical operation of the temporal difference. In fact, it has been shown that sensitivity to detect the noise component and/or the stochastic variations is enhanced by using the translation error E'_{trans} [49].

2. The following error is now defined to evaluate the numerical solutions that are compared to the original time series data of each component in the stabilograms:

$$\epsilon = \sqrt{\left(E^s_{\text{trans}} - E^r_{\text{trans}}\right)^2 + \left(E'^s_{\text{trans}} - E'^r_{\text{trans}}\right)^2}, \tag{9.7}$$

where the superscript s means the value estimated from the numerical solution, and r means that from the time series data.

3. The average values of the error (8.7) are obtained from ten numerical solutions for each parameter μ and Δt.
4. The combination of μ and Δt with the smallest error was defined as an optimum solution.

According to this method, we could obtain the optimum solutions to Eqs. (9.1)–(9.2). Observed SKG (Fig. 9.3b) was compared to simulative ones (Fig. 9.3c–d). Figure 9.3c, d was generated by substituting the white Gaussian noise and the pink noise into terms of the noise terms of the difference equations, respectively. As a result, the components of high frequency in the numerical solutions were enhanced in the increase of each parameter μ and Δt, respectively. The range distributed by the Gaussian white noise was less than half of those in the SKGs data and about half of those derived from the pink noise. Based on the discussion of calculation accuracy, digits in the evaluation value ϵ could be coarse-grained in these numerical simulations. In this numerical analysis, rich optimum solutions were expected to be derived from the pink noise. Moreover, the following qualitative property could be found in the results of these numerical simulations (Fig. 9.3c–d). The motion process derived from the pink noise tended to be persistent (Fig. 9.3d) whereas that from the Gaussian white noise looked like drunken stagger (random walk) as shown in Fig. 9.3c. As for the stabilometry findings, the SKG was closer to Fig. 9.3c rather than Fig. 9.3d. In the SKG as in Fig. 9.3b, we could extract cusp-shape trajectories where the righting reflex would be occurred.

9.4 New Models of Body Sway Described by AI

Sequences can be generated as similar as possible to actual data by the Generative Adversarial Network (GAN). Using the GAN, it is also possible to conduct the numerical analysis of the stochastic process as the body sway. In this section, we introduce numerical solutions to GANs as models describing the body sway during exposure to the 3D video films. Moreover, severity of the motion sickness is induced to the GAN as an endogenous variable. We have succeeded in extracting

characteristic form obtained from high percentage in the contribution of the endogenous variable to the severity of the motion sickness.

9.4.1 Definition of GANs

In recent years, the development of artificial intelligence has been remarkable, especially in machine learning models using deep learning, and results exceeding the correct recognition rate by humans have been confirmed in the field of image recognition [50]. It refers to the 1000-class image classification with labels such as birds, cats, ships, etc. In addition, this deep learning is attracting attention not only in the field of classification and regression, but also in the field of image generation. Among them, Generic Advertising Network (GAN) is known as a generation model [51].

In the GANs, a generator (G) and a discriminator (D) are used as shown in [51, 52]. Random sequences are input into the former neural network G, which outputs simulative arrangements to be as similar as possible to actual data. On the other hand, generated data and the actual data are input into the later neural network D, which distinguishes whether the simulative data can be regarded as actual data.

Based on the error from the correct answer to these output results, we conducted machine learning for each network G and D. After the output of D, the discriminator D was learned as follows; the correct answer to the was given to D whether the data input to D had been generated by G. In the next step, the weights of D were updated so that the error between the output of D and the correct answer became small. Also, the weights of G were updated so that the error between the back propagation from D and the correct answer became small. However, a value opposite to the correct answer abovementioned in D is herein given as a back propagation because the correct answer for D is incorrect for G. In this way, G learns to cheat D, and D learns to find G out, respectively. By repeating this machine learning, G gradually generates simulative arrangements close to actual data. As an example, we herein show a new model expression to conduct the numerical simulation of the body sway with the use of the GANs. As a side note, the mathematical model of the body sway has been described by stochastic differential equations, which was introduced in the last section.

9.4.2 Model of Body Sway Described by GANs

Two hundred and thirty eight health young volunteers participated in this study. They stood in the Romberg's posture on the stabilometer. The body sway was recorded as a SKG while viewing 3D video clips for 60 s, where the sampling frequency was set to be 20 Hz [53, 54]. In order to employ the numerical simulation of the body sway, these SKGs were referred to as the machine learning for the GANs.

The simulative arrangements were generated by the generator G. The degree of determinism in the sequences was evaluated by calculating the translation error using the Wayland algorithm. The values of the translation errors obtained from the SKG data were compared with those for the simulative SKGs in detail [53]. As a result of evaluating the similarity between the data and the numerical simulations from the viewpoint of degree of the determinism, it is possible for the GANs to describe the body sway.

In the previous studies, the random noise is only used as the input of the generator G. In [54], the conditions of the input array have been expressed as endogenous variables to substitute to an input node of G and output from an end node of D. Therefore, it is possible to control the generation of simulative arrangements from the GANs. We have succeeded in applying to employ the numerical simulation of the body sway influenced by the VIMS. The degree of motion sickness can be obtained from subjects that stand with the upright posture [31]. In [55], we have already classified 3D video clips that remarkably affect the equilibrium function in accordance with observations on the SKGs and the sway values while/after viewing the video clips.

Also, the machine learning stated in the last section was performed using the SKGs as image data while/after viewing the video clips. For this machine learning, we tried to control the simulative arrangements generated by inputting the information for the video clips, that is, severity of the VIMS (high/low) into the generator G. In addition to discriminating whether the input image for the discriminator D is a SKG data or a simulative arrangement, D was also trained to discriminate high/low severity of motion sickness. These estimations were finally output from two nodes. In other words, it is concentrated in a small number of artificial neurons close to the output layer, however, they depend on the output of artificial neurons in many intermediate layers. Superimposing the weights of those artificial neurons close to the output layer on the image array, the partial trajectories could be extracted from the image array input to D. It is possible to visualize characteristic form of the partial trajectories. We have considered that the size and the number of the trajectories depend on the output of D, the discrimination of the severity of the VIMS.

In the SKGs, we have succeeded in visualizing the form which is regarded as a characteristic of the VIMS (Fig. 9.4). This shows the contribution rate to the endogenous variable that indicates the severity of motion sickness, and the part with the high contribution rate is shown in warm colors. As a part with a high contribution rate, we extracted cusp-shaped trajectories where the righting reflex would be occurred. Form of these trajectory is very similar to those derived from the pink noise of use in the numerical solution to the SDEs in the last section. We believe that it is important for the studies of the AI to be implicated by the mathematical analysis and the numerical analysis of the mathematical model in parallel.

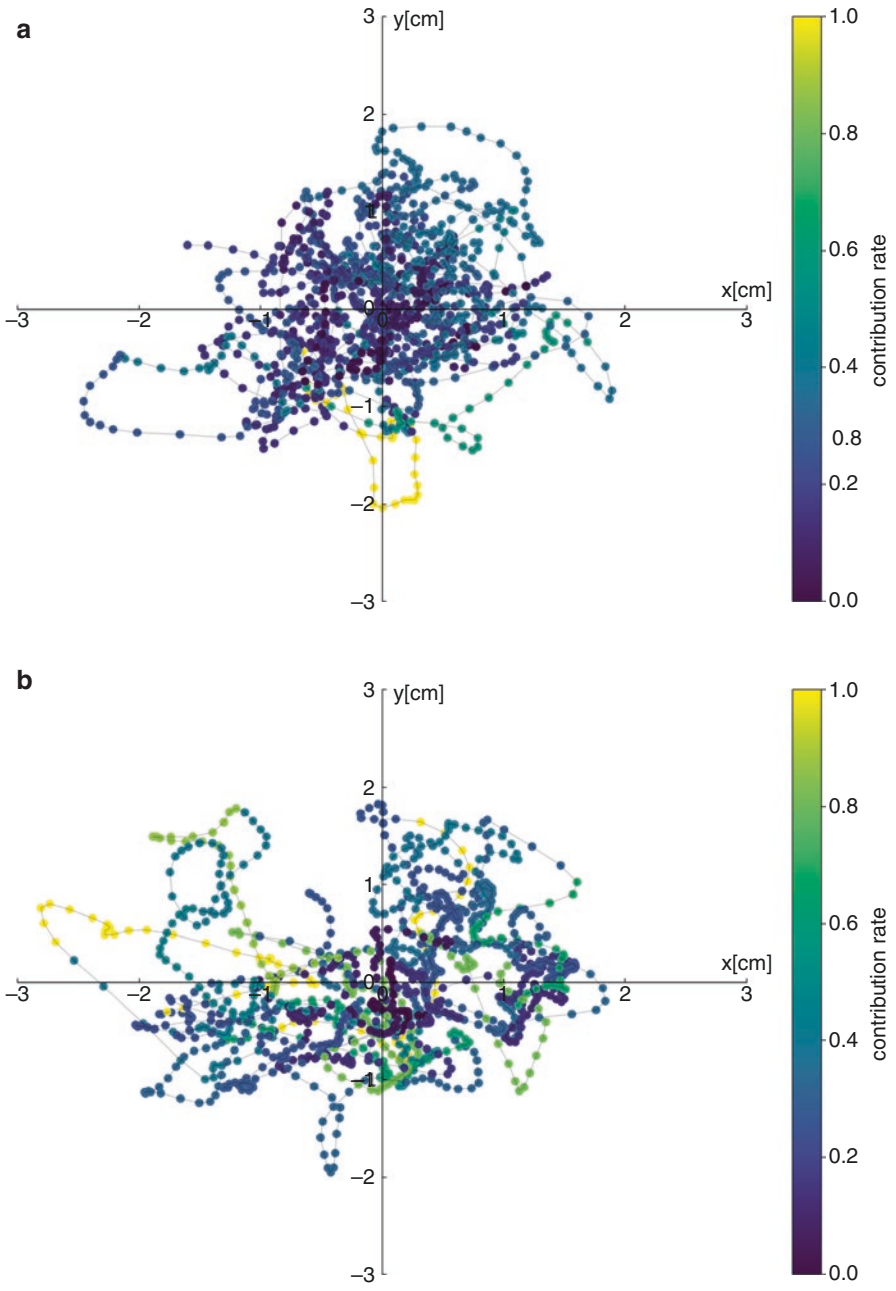

Fig. 9.4 A characteristic of the VIMS in SKGs; a typical SKG observed a young healthy subject without the motion sickness (**a**), a typical SKG observed a young healthy subject with the motion sickness (**b**)

Appendix Standards

Do not talk or give instructions during recording.

1. Clinical laboratory: A silent and evenly lit room, under the condition that body deviation for subjects does not occur due to sound or visual stimulations.
2. Arrangement for the stabilometry: Match the reference point on the stabilometer with the reference point on the charts.
3. Definition in the recording: In *X*–*Y* recording, the representation point of the CoP would move toward the upward (*Y*) and right (*X*) directions in stabilograms if the CoP deviated to the anterior and to the right, respectively. The anterior and the right directions are herein defined as positive in their axes that span Euclidian *XY*-plane. Subjects' center of gravity is projected onto this two-dimensional *XY*-plane. In the graphs of time course of the CoP for each component (Stabilogram), the representation point would move toward the upward if the CoP deviates forward and to the right.
4. Upright posture: Both upper limbs should be on each body side. Stabilometry should be performed in a natural standing posture. On the stabilometer, stand so that the center of subject's soles coincides with the reference point on the stabilometer.
5. Subjects would be instructed to close their eyes on the morrow of the stabilometry with their eyes open.
6. Visual target: The subjects with their eyes open are instructed to gaze at the visual target set at their front and their eye level in the stabilometry. The target should be put at a distance of 1–3 m from the stabilometer. Subjects with their eyes closed should keep their posture without circling their head as well as in the stabilometry with their eyes open. At this time, subjects had been instructed in advance to imagine that they were still gazing at the target.
7. Take off your footwear and inspect on their bare feet, but you can leave it as it is if it is thin socks.
8. Foot position: Subjects stand upright with feet together. Subjects would be asked to take a wide stance with feet parallel or to stand with both heels in contact if it were difficult to keep upright posture with feet together. In these cases, it is necessary to note the distance between feet or the angle between the semimajor axes of both feet.
9. Onset of recording: Recording can be started about 10 to 15 s after subjects stood on the stabilometer when the body sway has been stabilized. SKGs and stabilograms should be recorded except for transient processes.
10. Recording duration: SKGs and stabilograms are basically recorded for 60 s. In the case where it is difficult to stand upright for 60 s, recording is performed for 30 s. Chart lasting time (recording duration) should be noted only if it were other than 60 s.

Acknowledgment Figure 9.1 was provided by Anima Co. Ltd. (Tokyo, Japan). This chapter was supported in part by the Japan Society for the Promotion of Science, Grant-in-Aid for Scientific Research (C) Number 20K12528.

References

1. Einthoven W. Le Télécardiogramme Arch Int Physiol. 1906;4:132.
2. Soffer A. Snellen, Einthoven's machine, alive and well. Chest. 2005;128:487–8.
3. Kapteyn TS, Bles W, Njiokiktjien CJ, Kodde L, Massen CH, Mol JM. Standardization in platform stabilometry being a part of posturography. Agressologie. 1983;24:321–6.
4. Palmer CE. Studies of the center of gravity in the human body. 1944;15(2):99–180. https://doi.org/10.2307/1125537.
5. Palmer CE. Center of gravity of the human body during growth. Am J Phys Anthropol. 1923;11:423–55.
6. Basler A. Zur Physiologie des Hockeno. Z Biol. 1929;88:523–30.
7. Travis RC. A new stabilometer for measuring dynamic equilibrium in the standing position. J Exp Psychol. 1944;34:418–24.
8. Baron JB. Presentation d'un appareil pour mettre en evidence les deplacements du center de gravite du corps dans le polygone de sustentation. Societe de medecine et d'hygiene du travail. 1964;25:41–9.
9. Yamamoto M, Yoshida T. Body tracking test (BTT), galvanic body sway test (GBST). Equi Res. 2011;70(3):135–44.
10. Okawa T, Tokita T, Shibata Y, Ogawa T, Miyata H. Stabilometry: significance of locus length per unit area (L/a) in patients with equilibrium disturbances. Equil Res. 1995;54:283–93.
11. Xu JX, Sun Y. Modeling and analysis of the falling process based on a five-link gait model. CIS 2012;40. https://doi.org/10.2316/Journal.201.2012.1.201-2319.
12. Suzuki J, Matsunaga T, Tokumatsu K, Taguchi K, Watanabe Y. Q&a on Stabilometry GuideBook (1995). Equil Res. 1996;55:64–77.
13. Examination of equilibrium standardization committee. The standardization of the equilibrium function test. Equil Res. 2006;65(6):468–503.
14. Stabilometers. JIS T-1190-1987. http://www.kikakurui.com/t1/T1190-1987-01.html
15. Diagnosis standardization committee & Insurance medical care committee in Japan society for equilibrium research (JSER). Precision of the stabilometer for medical use. Equi Res. 2015;74(1):44–50. https://doi.org/10.3757/jser.74.44
16. Fukuda T. Statokinetic reflexes in equilibrium and movement. Tokyo: University of Tokyo Press; 1984.
17. Yasuda K, Utamura Y. Peculiarities of Fukuda's stepping test. J Otol Jpn. 1970;15:233–9. (In Japanese)
18. Yoshida T, Yamamoto M, Orihara H, Miyake T, Osafune H, Oda M. Age-dependent changes in dynamic body balance as evaluated by the body tracking test (BTT). J Otolaryngol Jpn. 1999;102:27–34.
19. Yoshida T, Yamamoto M, Nomura T, Seto A, Kobayashi M, Takeuchi J. Examination of a new quantitative evaluation method for the body tracking test (BTT). Equil Res. 2003;62(1):47–54.
20. Furman JM, Wuyts FL. Vestibular laboratory testing. In: Aminoff's electrodiagnosis in clinical neurology. 6th ed. Berkeley: Elsevier; 2012. p. 699–723. https://doi.org/10.1016/B978-1-4557-0308-1.00032-7.
21. Severac CA, Faldon M, Popov K, Day BL, Bronstein AM. Short-latency eye movements evoked by near-threshold galvanic vestibular stimulation. Exp Brain Res. 2003;148:414–8. https://doi.org/10.1007/s00221-002-1326-z.

22. Benson AJ, Jobson PH. Body sway induced by a low frequency alternating current. Int J Equil Res. 1973;3:55–61.
23. Hlavacka F, Njiokiktjien C. Postural responses evoked by sinusoidal galvanic stimulation of the labyrinth. Influence of head position. Acta Otolaryngol. 1985;99:107–12. https://doi.org/10.3109/00016488509119152.
24. Tokita T, Ito Y, Takagi K. Modulation by head and trunk positions of the vestibulo-spinal reflexes evoked by galvanic stimulation of the labyrinth. Observation by labyrinthine evoked by EMG. Acta Otolaryngol. 1989;107:327–32. https://doi.org/10.3109/00016488909127516.
25. Takada H, Takada M, Miyao M, Furuta M, Tanaka K, Shiozawa Y. Effects of galvanic vestibular stimulation on statokinesigrams of the elderly. Geron. 2008;7(3):329. https://doi.org/10.4017/gt.2008.07.03.009.00.
26. Takada H. Expression for mathematical models of time series data in dual space: Expression of balance function during galvanic vestibular stimulation. Proc IEEE Int Conf Comp Sci Eng. 2016. https://doi.org/10.1109/ICCSE.2016.7581545.
27. Sugiura A, Akachi K, Yoshida A, Ito C, Kondo S, Tanaka K, Takada H. Experimental study on control of visually evoked postural responses by galvanic vestibular stimulation. Proc IEEE (ICCSE). 2017. https://doi.org/10.1109/ICCSE.2017.8085467.
28. Takada H. Theoretical expression of the balance function during galvanic vestibular stimulation in dual space. Adv Sci Tech Eng Syst J. 2017;2(1):186–91.
29. Reason JT. Motion sickness adaptation. J R Soc Med. 1978;71:819–29.
30. Stoffregen TA, Smart LJ. Postural instability precedes motion sickness. Brain Res Bull. 1998;47:437–48.
31. Takada H, Miyao M, Fateh S. Stereopsis and hygiene. Singapore: Springer; 2019.
32. Takada H, Miyao M. Visual fatigue and motion sickness induced by 3D video clip. Forma. 2012;27:S67–76.
33. Takada H, Kitaoka Y, Ichikawa M, Miyao M. Physical meaning of geometrical index for stabilometry. Equil Res. 2003;62(3):168–80.
34. Japan Society for Equilibrium Research. Standard of Stabilometry. Equil Res. 1983;42:367–9.
35. Uludag K, Dubowitz DJ, Yoder EJ, Restom K, Liu TT, Buxton RB. Coupling of cerebral blood flow and oxygen consumption during physiological activation and deactivation measured with fMRI. Neuroimage. 2004;23:148–55.
36. Ungerleider LG, Mishkin M. Two cortical visual systems. In: Ingle DJ, Goodale MA, Mansfield RJW, editors. Analysis of visual behavior. Cambridge: MIT; 1982.
37. Goldie PA, Bach TM, Evans OM. Force platform measures for evaluating postural control: reliability and validity. Arch Phys Med Rehabil. 1989;70:510–7.
38. Emmerrik REA, Sprague RLV, Newell KM. Assessment of sway dynamics in tardive dyskinesia and developmental disability: sway profile orientation and stereotypy. Mov Dis. 1993;8:305–14.
39. Collins JJ, Luca CJD. Open loop and closed-loop control of posture: a random-walk analysis of center of pressure trajectories. Exp Brain Res. 1993;95:308–18.
40. Newell KM, Slobounov SM, Slobounova ES, Molenaar PC. Stochastic processes in postural center of pressure profiles. Exp Brain Res. 1997;113:158–64.
41. Takada H, Kitaoka Y, Shimizu Y. Mathematical index and model in stabilometry. Forma. 2001;16:17–46.
42. Matsumoto M, Nishimura T. Mersenne twister: a 623-dimensionally equidistributed uniform pseudo-random number generator. ACM Trans Model Comp Simul. 1998;8(1):3–30.
43. Box GEP, Muller ME. A note on the generation of random normal deviates. Ann Math Statist. 1958;29(2):610–1.
44. Kobayashi M, Musha T. 1/f fluctuation of heartbeat period. IEEE Trans BME. 1982;29(6):456–7.
45. Castiglioni P, Frattola A, Parati G, Rienzo M. 1/f-modeling of blood pressure and heart rate spectra: relations to aging. Proc Ann Int Conj IEEE Eng Med Biol Soc. 1992;465–6.
46. Hausdroff J, Peng C, Ladin Z, Wei J, Goldberger A. Is walking a random walk? Evidence for long-range correlations in stride interval of human gait. J Appl Physiol. 1995;78(1):349–58.

47. Goldberger A. Ko baiter K, Bhargava V. 1/f-like scaling in normal neutrophil dynamics: implications for hematologic monitoring. IEEE Trans Biomed Eng. 1986;33(9):874–6.
48. Kinoshita F, Miyao M, Takada M, Takada H. Expression of balance function during exposure to stereoscopic video clips. ASTES J. 2017;2:121–6. https://doi.org/10.25046/aj020114
49. Takada H, Morimoto T, Tsunashima H, Yamazaki T, Hoshina H, Miyao M. Applications of double-Wayland algorithm to detect anomalous signals. Forma. 2006;21(2):159–67.
50. He K, Zhang X, Ren S, Sun J. Delving deep into rectifiers: surpassing human-level performance on ImageNet classification. Proc IEEE Int Conf Comp Vision. 2015. https://doi.org/10.1109/ICCV.2015.123.
51. Goodfellow I, Pouget-Abadie J, Mirza M, Xu B, Warde-Farley D, Ozair S, Courville A, Bengio Y. Generative adversarial nets. Proc Conf Neur Info Process Sys. 2014;2672–80.
52. Radford A, Metz L, Chintala S. Unsupervised representation learning with deep convolutional generative adversarial networks. Proc Int Conf Learn Represent. 2016; arXiv preprint. arXiv:1511.06434.
53. Nakane K, Takada H, Yamamoto S, Ono R, Takada M. Numerical analysis of bio-signal using generative adversarial networks. Lect Note Comp Sci. 2020;12423–9. (in Press).
54. Nakane K, Ono R, Yamamoto S, Takada M, Kinoshita F, Sugiura A, Matsuura Y, Fujikake K, Takada H. Numerical analysis of body sway for evaluation of 3D sickness. Proc IEEE Int Conf Comp Sci Edu. 2020;89–95.
55. Amano N, Takada H, Jono Y, Tanimura T, Kinoshita F, Miyao M, Takada M. Analysis of the body sway while/after viewing visual target movement synchronized with background motion. Lect Note Comp Sci. 2018;10908:3–14.

Chapter 10
Motion Capture

Kiyoko Yokoyama

Abstract Frailty prevention is an important social problem for healthy life extension in an aging society. It is useful to continue daily exercise to augment muscular strength, maintain the sense of balance, and prevent motor function deterioration with aging. Motion analysis is being carried out as one method of diagnosing frailty. This chapter introduces an optical motion capture system suitable for high-precision measurement of motion, and describes methods for visualizing body condition in synchronization with motion. In the first method, the motion measured by motion capture is expressed by the animation of a 3D computer graphics character, and the color and motion of the muscle and heart of the character are synchronously changed. The second method focuses on a specific part of the body and superimposes velocity, acceleration, and muscle activity on the locus of the coordinates.

Keywords Optical motion capture system · Visualizing physiological condition · Visualizing velocity and acceleration · Motion analysis · Integrated visualization of motion and biological signals

10.1 Introduction

Frailty prevention is an important social problem for healthy life extension in an aging society. It is useful to continue daily exercise to augment muscular strength, maintain the sense of balance, and prevent motor function deterioration with aging. Motion analysis is being carried out as one method of diagnosing frailty [1, 2]. An optical motion capture system is a piece of equipment that achieves motion analysis with high precision. This chapter introduces a technique of synchronous visualization with human motion in a three-dimensional space using optical motion capture and biological signals such as electromyograms (EMGs) and electrocardiograms (ECGs) and a technique of visualizing motion that aims for application in the study of motion.

K. Yokoyama (✉)
Graduate School of Design and Architecture, Nagoya City University, Nagoya, Aichi, Japan
e-mail: yokoyama@sda.nagoya-cu.ac.jp

H. Takada, K. Yokoyama (eds.), *Bio-information for Hygiene*, Current Topics in Environmental Health and Preventive Medicine,
https://doi.org/10.1007/978-981-15-2160-7_10

10.2 Optical Motion Capture System

An optical motion capture system is a device for measuring and recording the three-dimensional coordinates of a single marker photographed by multiple cameras. To enable high-precision measurement for motion analysis or the like, a method of radiating infrared rays from a camera and photographing an infrared reflecting marker image is generally used. The maximum frame rate of 200 to 300 fps and some models offer 810 fps. In the latest models, it is also possible to measure and record markerlessly, in other words, using multiple video cameras to film a person in everyday clothes in a three-dimensional space. Optical motion capture systems have a wide range of applications, from the entertainment field including 3D computer graphics animation production [3], character motion production in virtual reality [4], game production [5], and media art [6] to utilization in motion analysis such as analyzing workers' labor [7], measuring the effect of rehabilitation [8], treatment in sports medicine and failure prevention [9].

As illustrated in Fig. 10.1, about 30–40 markers are attached mainly to joints for measurement of whole-body movement. The three-dimensional coordinates of the markers are recorded as time series. When reproducing motion as an animation of an object, the shape of the object is modeled using 3D computer graphics software or the like. The modeled object is connected with the measured marker positions. In the case of motion analysis, the joint angles and movement speed, acceleration, and momentum of parts are calculated from the measured three-dimensional coordinates. Figure 10.2 shows a scene of measurement in the studio and the measurement screen of the motion capture system.

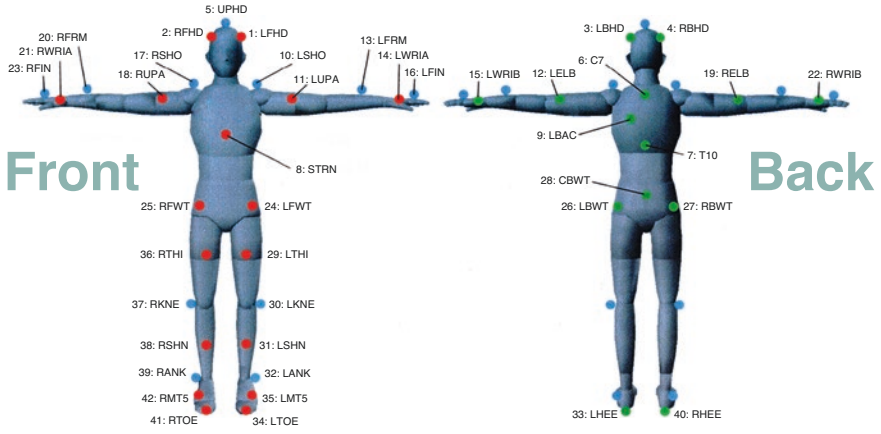

Fig. 10.1 Example of marker positions

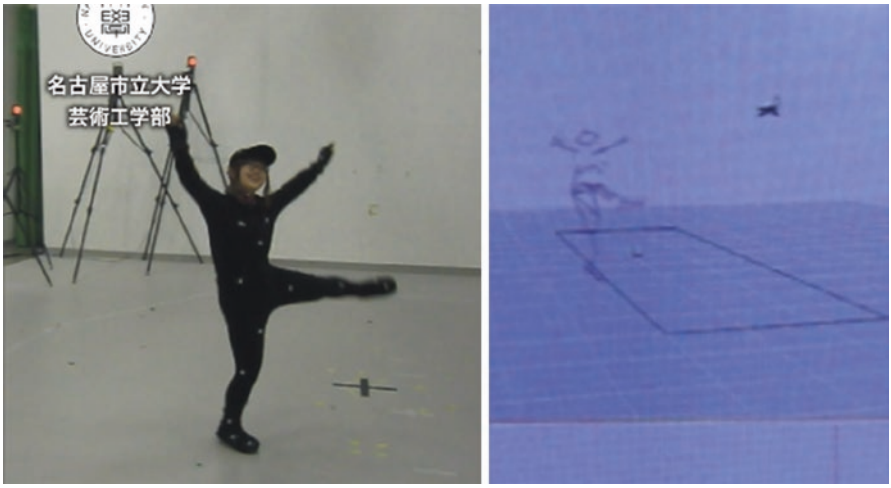

Fig. 10.2 Scene of measurement in the studio and the measurement screen of the motion capture system

10.3 Integrated Visualization of Motion and Biological Signals

Motions measured with motion capture and biological signals such as EMGs and ECGs that reflect the state inside an organism are synchronously visualized using character animation [10]. The training effect of exercise can be evaluated by simultaneously expressing the movement of the body and EMG. It is also possible to apply it to the workload of labor and the usability evaluation of products. Synchronous visualization of motion and cardiovascular performance indicators can reveal the relationship between changes in cardiovascular performance and motion during daily activities [11]. As shown in the visualization schematics in Fig. 10.3, motion is measured by motion capture and synchronized with EMG and ECG. EMGs calculate the integrated EMGs after full-wave rectification and expresses the magnitude of the integrated EMGs by the brightness of the color of the muscle at the measurement site. In the case of red, the color of the muscle is black when the value of integrated EMG is small, in other words, the force exerted by the muscle is small, and bright red when the force exerted by the muscle is large and the value of the integrated EMG is large. Since the waveform of the ECG is generated in synchronization with the contraction motion of the heart, the CG heart model is displayed in a small size in synchronization with the R wave that appears as a sharp wave in the figure, and is gradually expanded until the next R wave occurs. In this way, the CG heart model in animation beats in synchronization with

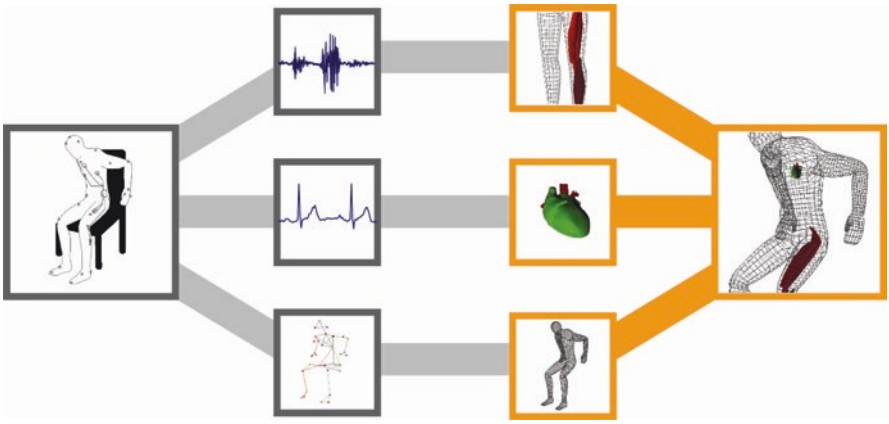

Fig. 10.3 Schematic diagram of motion and biological signals integrated visualization system

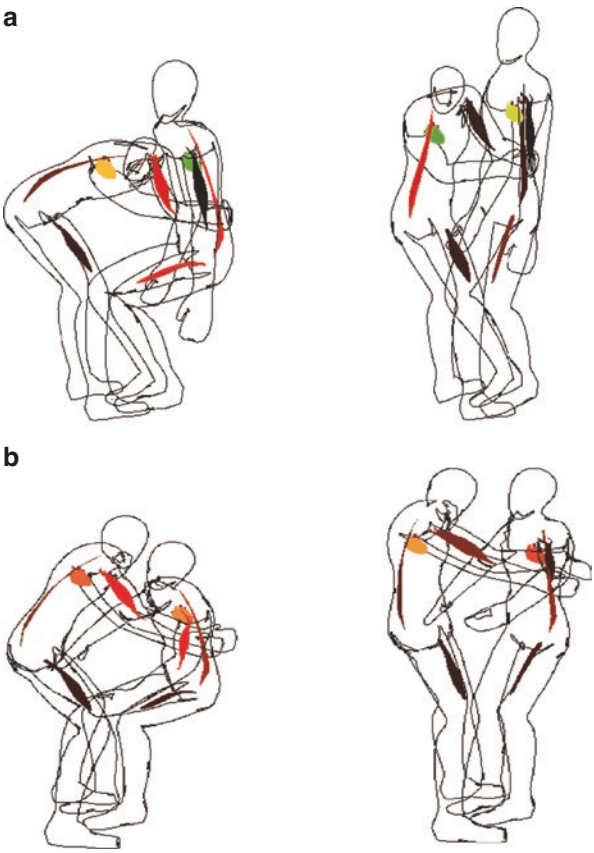

Fig. 10.4 An example of visualizing an electromyographic heart rate and a motion simulating (**a**) active assistance and (**b**) passive assistance

measured ECG. The instantaneous heart rate, which is obtained by converting the heartbeat interval into a heart rate, can be calculated from the ECG, and is expressed by the color of the heart. When the heart rate is fast, it is red, when medium, it is yellow, and when slow, it is green.

Figure 10.4 shows an example of visualizing an electromyograph, heart rate, and motion simulating active assistance (a) and passive assistance (b). The action is assistance standing up from a chair. In active assistance, the person stands upon his or her own as much as possible, with the caregiver helping them move. In passive assistance, the person leaves all movements to the caregiver and stands up with the help of the caregiver alone. When (a) and (b) are compared, the color of the caretaker's heart is yellow in active assistance, but becomes orange close to red in passive assistance, indicating that the caretaker's exercise burden in passive assistance is large. As for the color of the muscles of the cared person, both the upper arm and the back during passive assistance were red and orange, suggesting that force was applied to the whole body.

Figure 10.5 shows the posture at the time of posture change from the sitting position to standing up and the balance of autonomic nervous activity at that time. The color of the heart indicates the heart rate, and the size of the rings around the heart indicates the autonomic nerve activity balance. A small ring indicates increased sympathetic nerve activity; a large ring indicates increased parasympathetic nerve activity. The autonomic nerve activity balance is based on the fact that parasympathetic nerve activity is enhanced when the amplitude of the high-frequency component (HF) of the heart rate variability time series is large [12], and the size of the ring is determined in relation to the value of HF calculated with a 30 s window

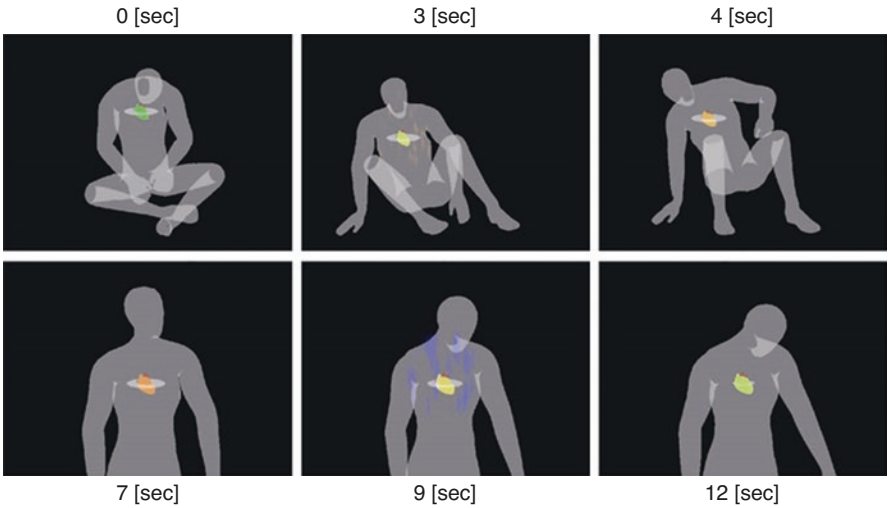

Fig. 10.5 Examples of visualization of the posture and the balance of autonomic nervous activity while posture change from sitting to standing. The color of the heart indicates the heart rate, and the size of the rings around the heart indicates the parasympathetic nerve activity

width. In the sitting position, the heart is green and has large rings, indicating increased parasympathetic activity and a low heart rate. On the other hand, immediately after standing up (time point 7 s), the heart rate increases and the color of the heart turns orange. The result of visualization intuitively shows that the rings become smaller and the sympathetic nerve activity increases in the standing position.

10.4 Visualization of Motion Loci, Velocity and Acceleration, and Muscle Activity

This visualization method is intended to be used to support motion education. It can be applied to sports education, handing traditional performing arts, and learning work movements with less physical load. It presents the trajectory, velocity, and acceleration of a specific part at the same time.

The motion locus is drawn with spheres. Velocity and acceleration visualization relates velocity to the radius of the sphere and acceleration to the color. The greater the speed, the thicker the locus, and the slower, the thinner the locus. When acceleration is positive, the color changes to green, yellow, and red as the value increases. When acceleration is negative (deceleration), it changes to light blue, blue, and purple, corresponding to an increase in the absolute value. For visualization of muscle activity, the integrated EMG values calculated by full-wave rectification of the EMG are related to the radius of the sphere on which the locus is drawn. When the muscle is exerting a large force, the locus is thick, and when the force is small, the locus is thin. Color is drawn only when the muscle activity is larger than the threshold value, and it is drawn in red when the muscle activity is large and the acceleration is positive, and in blue when the muscle activity is large and the acceleration is negative. It is designed to distinguish whether the subject is trying to accelerate or slow down.

Figure 10.6 shows an example of visualization using data obtained by measuring motion capture when a skilled painter paints a 910 mm × 1820 mm board with a roller brush and simultaneous measurement of the EMG of the biceps brachii. In (a), the radius and color of the sphere, which the locus is drawn with, respectively, represent the velocity and acceleration of the marker on the back of the hand holding the roller brush. In (b), as in (a), the locus is the coordinates of the marker on the back of the hand holding the roller brush, and the radius of the sphere, which the locus is drawn with, is the muscle activity of the biceps brachii, and the color is drawn in red and blue depending on whether the acceleration calculated from the time series of the marker on the back of the hand is positive or negative. The upper part and the lower part are painted separately, and the characteristics of the painting motion of the expert are intuitively conveyed, such as that the upper arm is used for downward direction change, the upper arm is not used for upward direction change, and the thickness of the locus does not change except for direction change and the painting is done at a constant speed.

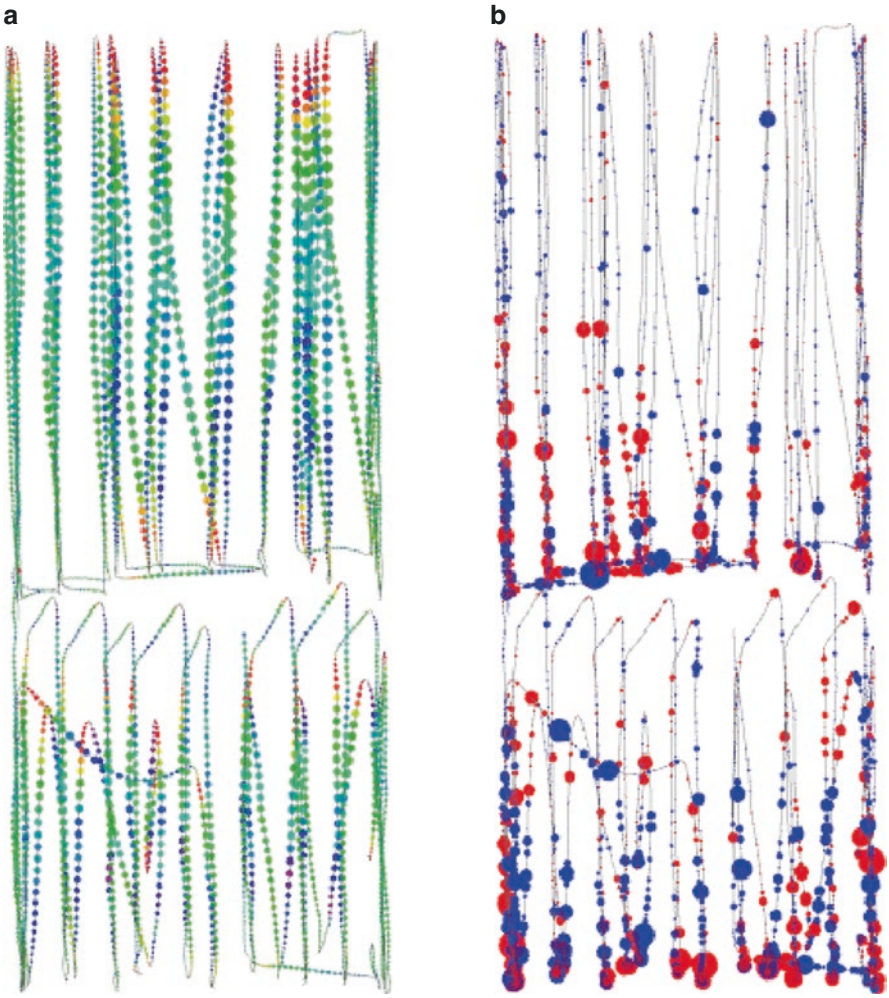

Fig. 10.6 An example of visualization of painting motion by a skilled painter. (**a**) Radius and color of the sphere, which the locus is drawn with, respectively, represent the velocity and acceleration of the marker on the back of the hand holding the roller brush. (**b**) The locus is the coordinates of the marker on the back of the hand holding the roller brush, and the radius of the sphere, which the locus is drawn with, is the muscle activity of the biceps brachii, and the color is drawn in red and blue depending on whether the acceleration calculated from the time series of the marker on the back of the hand is positive or negative

10.5 Conclusion

This chapter introduces an optical motion capture system suitable for high-precision measurement of motion, and describes methods for visualizing body state in synchronization with motion. In the first method, the motion measured by motion

capture is expressed by the animation of a 3D computer graphics character, and the color and motion of the muscle and heart of the character are synchronously changed. This method makes it possible to evaluate the work load accompanied by physical movement and to visualize the effect on the body part accompanied by movement, and it can contribute to the prevention of health impairment caused by work and sports. It is also possible to visualize cardiovascular dynamics in response to movements in daily life and to contribute to the prediction of dangerous conditions such as sudden changes in blood pressure in response to movements. The second method focuses on a specific part of the body and superimposes velocity, acceleration, and muscle activity on the locus of the coordinates. This method can be used as an auxiliary teaching material for explaining exercise methods for frailty prevention, etc., and as educational support using example work motions with less physical burden on skilled workers.

References

1. Ganea R, Paraschiv-Ionescu A, Salarian A, Bula C, Martin E, Rochat S, Hoskovec C, Piot-Ziegler C, Aminian K. Kinematics and dynamic complexity of postural transitions in frail elderly subjects. In: Proceedings of 29th IEEE EMBC; 2007. https://doi.org/10.1109/IEMBS.2007.4353745
2. Schwenk M, Howe C, Saleh A, Mohler J, Grewal G, Armstrong D, Najafi B. Frailty and technology: a systematic review of gait analysis in those with frailty. Gerontology. 2014;60(1):79–89.
3. Geng W, Yu G. Reuse of motion capture data in animation: a review. ICCSA. 2003;2003:620–9.
4. Chan JCP, Leung H, Tang JKT, Komura T. A virtual reality dance training system using motion capture technology. IEEE Trans Learn Technol. 2011;4(2):187–95.
5. Rincon AL, Yamasaki H, Shimoda S. Design of a video game for rehabilitation using motion capture, EMG analysis and virtual reality. 2016 CONIELECOMP; 2016. https://doi.org/10.1109/CONIELECOMP.2016.7438575
6. Meador WS, Rogers TJ, O'Neal KR, Kurt EM, Cunningham C. Mixing dance realities: collaborative development of live-motion capture in a performing arts environment. Comput Entertain. 2004. https://doi.org/10.1145/1008213.1008233
7. Bortolini M, Gamberi M, Pilati F, Regattieri A. Automatic assessment of the ergonomic risk for manual manufacturing and assembly activities through optical motion capture technology. Proc CIRP. 2018;72:81–6.
8. Mirabella O, Raucea A, Fisichella F, Gentile L. A motion capture system for sport training and rehabilitation. In: Proceedings of 4th HSI 2011; 2011. https://doi.org/10.1109/HSI.2011.5937342
9. Charbonnier C, Kolo FC, Duthon VB, et al. Assessment of congruence and impingement of the hip joint in professional ballet dancers: a motion capture study. Am J Sports Med. 2010. https://doi.org/10.1177/0363546510386002
10. Matsukawa T, Umetani T, Yokoyama K. Development of health monitoring system based on three-dimensional imaging using bio-signals and motion data. In: Proceedings of 27th EMBC; 2007. https://doi.org/10.1109/IEMBS.2007.4352591
11. Matsukawa T, Yokoyama K. Visualizing physiological information based on 3DCG. Forma. 2010;25:11–4.
12. Task Force of the European Society of Cardiology the North American Society of Pacing Electro-physiology: Heart rate variability – standards of measurement, physiological interpretation, and clinical use, Circulation. 1996;93(5):1043–65.

Chapter 11
A Development of Physical Feedback Structure for Virtual Rehabilitation System Using Air Pressure

Kouki Nagamune and Shinto Nakamura

Abstract With the aging society, a rehabilitation system using Virtual Reality (VR) technology that can be easily performed at home without limiting the place and time is being developed. In recent years, research on tactile sensation in VR has been conducted, and various wearable devices have been developed, but there are few reports on the effects of tactile sensation and reality in VR rehabilitation. In this study, we developed a device that can obtain feedback information of tactile sensation and observed the effect of the presence or absence of tactile sensation stimulation in VR rehabilitation.

For the rehabilitation system, Box and Block Test, which is one of the upper limb function tests, was created on Unity, which is a game engine, and automated. We also aimed to develop a compact pneumatic system using an air pump and latex balloon for tactile stimulation. In the experiment, the distances between the index finger and thumb, and the middle finger and thumb were measured, and the difference in score and distance was calculated in the Box and Block Test on Unity with and without tactile information.

Keywords Virtual Reality (VR) · VR rehabilitation · Training system · Physical feedback · Tactile sensation

K. Nagamune (✉) · S. Nakamura
Graduate School of Engineering, Human and Artificial Intelligent Systems, University of Fukui, Fukui, Japan
e-mail: nagamune@u-fukui.ac.jp

H. Takada, K. Yokoyama (eds.), *Bio-information for Hygiene*, Current Topics in Environmental Health and Preventive Medicine,
https://doi.org/10.1007/978-981-15-2160-7_11

11.1 Introduction

Currently, Japan is aging with the development of medical care. As of September 2020, the ratio of elderly people (65 years old and over) to the total population of Japan is 28.7%, which is the highest ratio in the world [1]. As the population ages, the number of elderly people with disabilities is expected to increase, such as an increase in cases of falls and strokes due to decreased activities of daily living (ADL), and an increase in the number of elderly people with disabilities due to sequelae of strokes. Therefore, it is necessary to improve the movement by nursing care and rehabilitation, but there are various problems. Currently, the number of days that medical insurance can be used for maintenance rehabilitation is fixed for each disease. In addition, there is a shortage of care workers such as physical therapists (PTs), and occupational therapists (OTs), and there are cases where the situation worsens without receiving sufficient rehabilitation [2].

In recent years, rehabilitation systems using Virtual Reality (VR) technology have been developed to solve these problems. By using VR technology, continuous rehabilitation at home becomes easy because it can be done at any time and place. In addition, depending on the program, it is possible to reproduce various environments and give it a game-like character, which has the advantage of maintaining motivation [3].

However, the presentation of information to sensations other than sight and hearing is still insufficient, and it is possible that the immersive feeling and effectiveness of the actual upper limb function test are reduced. There are many parts that have not yet been elucidated regarding the sense of tactile force. Previous research has been conducted by various presentation methods to reproduce, but it is inevitable to increase the number of devices to present more complicated information. In addition, the number of reports of VR rehabilitation used is small, and the importance of tactile force sensation information in VR rehabilitation is uncertain.

In this study, we focus on the effect generated by giving tactile sensation stimulation using an air pressure system and obtaining feedback information by sensation other than visual information. The Box and Block Test, which is one of the upper limb function tests, is performed on the screen of a personal computer (PC) to evaluate the effect and importance of the presence or absence of tactile feedback information in VR rehabilitation.

11.2 Preliminary

11.2.1 Tactile Sensation

Tactile sensation is a sensation caused by each receptor on the body surface by interaction with an object, and can feel pressure, temperature, and pain.

The skin is divided into three layers: Epidermis, dermis, and subcutaneous tissue, each of which has receptors that respond to various stimuli. From the epidermis to the dermis, the Meissner corpuscle and the Merkel corpuscle are located, and from the dermis to the subcutaneous tissue, the Pacinian corpuscle and the Ruffini ending are located, and the adaptation speed and frequency characteristics differ for each receptor. In addition, the structure changes depending on the hairy and hairless parts and age.

In addition, there are two-point discrimination ability and spatial localization ability in the sensory distinction on the skin. The two-point discrimination ability indicates whether two points on the skin can be clearly distinguished as two points when they are stimulated at the same time, and the minimum distance between the two points is defined as the two-point discrimination threshold. Call. Spatial localization ability is the ability to recognize the stimulus position by stimulating one point, and is expressed by the magnitude of the error. Receptors for these tactile stimuli, especially touching feeling and pressure, are densely distributed in the fingertips and nose and have high ability. Therefore, there are many previous studies targeting fingertips when reproducing tactile stimuli.

11.2.2 Box and Block Test

The Box and Block Test is one of the upper limb function tests, and the outline of the procedure and scoring is specified by Matiowetz et al. (1985) [4]. It is simple and can be inspected in a short time, and the dexterity of one hand is measured. It can be used in various patients with brain injury. Table 11.1 shows the equipment required for the inspection.

The inspection procedure is as follows. Prepare a box bisected by a partition on the table.

1. Put all 150 wooden cube blocks with a side of 25 mm into the box compartment on the patient's dominant hand side.
2. The patient moves the block to the other compartment in 60 s. It is evaluated according to the number of blocks moved.

In addition, there are some points to note when performing the inspection. The observer of the examination sits facing the patient and observes whether the patient's fingertips are moving across the partition. Blocks that are confirmed to have crossed the partition are counted and dropped or bounced in the other section. Even if two

Table 11.1 Equipment required for box and block test

1	Box 537 [mm] × 254 [mm] × 85 [mm] (W × D × H)
2	Partition to sperate the box 254 [mm] × 254 [mm]
3	Block 25 [mm] × 25 [mm] × 25 [mm] (W × D × H)
4	Stopwatch

or more are moved at the same time, they are counted as one block. The evaluation is performed after paying attention to these points. The higher the score, the better the dexterity of the hand. The evaluation sheet for entering the score has columns for entering the patient's dominant hand, examination date, score of the dominant hand, and score of the nondominant hand.

11.3 Method

The outline of the system in this study is shown in Fig. 11.1. The information of the fingers obtained by Leap Motion Controller [5–7] is displayed on the monitor, and Box and Block Test is performed in the virtual space. When contact is detected between the virtual hand and the virtual object, the air pump is driven through the microcontroller and a tactile sensation is given to the fingertips. The drive of the air pump is controlled by the PWM (Pulse Width Modulation) signal, and the latex balloon, which is the tactile force presentation part, is inflated step by step.

11.3.1 Box and Block Test on Unity

The Box and Block Test is reproduced using the development platform Unity (Ver.2020.1.12f1 Personal) (Fig. 11.2). Tables 11.2 and 11.3 show the sizes of boxes and blocks. The box is the same size as the actual size, and the block is set to a cube with a side of 100 mm, which is slightly larger than the actual size. This is to make

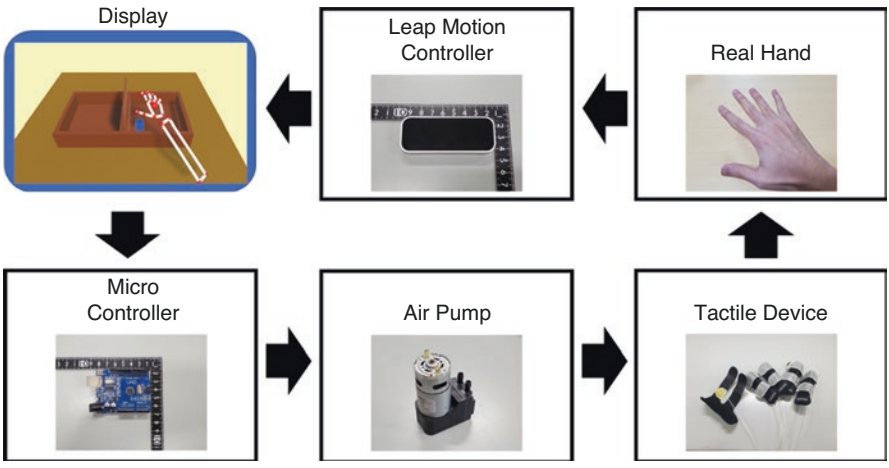

Fig. 11.1 Overview of the system

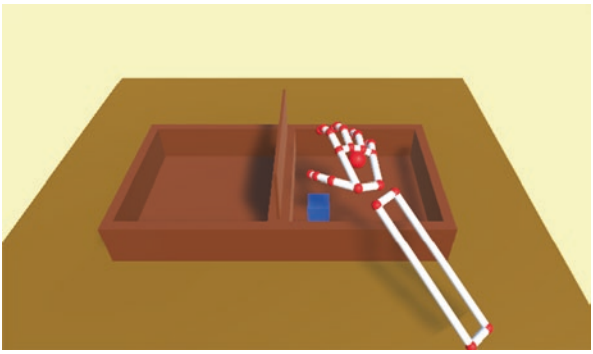

Fig. 11.2 Box and block test on unity

Table 11.2 Box scale on unity

Depth	290 [mm]
Width	580 [mm]
Height	185 [mm]

Table 11.3 Block scale on unity

Depth	40 [mm]
Width	40 [mm]
Height	40 [mm]

it easier to determine whether there is a difference between the ease of grasping and the presence or absence of tactile information. In addition, blocks are displayed one by one in the box on the dominant hand side, and the next block is set to be generated as soon as the movement to the other box is completed.

11.3.2 Microcontroller

The KKHMF UNO R3 development board (Apple Trees E-commerce co., LTD) is a development board compatible with the Arduino UNO R3 which is one of the microcontrollers. The air pump is flexibly driven by performing serial communication with Unity and changing the value of the PWM signal according to the signal. The PWM signal can be used with digital pins numbered 3, 5, 6, 9, 10, and 11, and the value changes between 0 and 255 depending on the degree of interference between the virtual hand and the virtual object. Arduino IDE is used as the development environment. The main specifications are shown in Table 11.4.

Table 11.4 Specification of KKHMF UNO R3 development board

Digital I/O	0–13
Analog I/O	0–5
Output voltage	DC 5 [V], DC 3.3 [V]
Input voltage	5–9 [V] (AC Adapter)
Size	73 [mm] × 52 [mm]

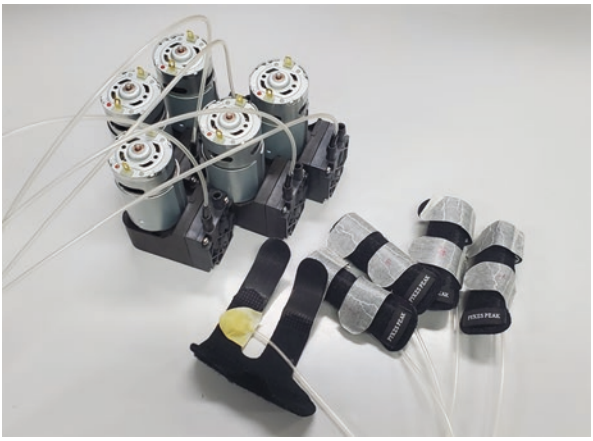

Fig. 11.3 Overview of physical feedback system with air pump

11.3.3 Physical Feedback System with Pump

Figure 11.3 shows a panoramic view of the pneumatic system. The air sent out by the air pump (D2028, SparkFun Electronics) passes through the tube and inflates the balloon, which is the tactile force presentation part. Balloons are attached to finger supporters and are attached by wrapping the finger supporters around each finger. The recognition rate was improved by attaching a white tape to the finger supporters.

11.3.4 Distance Measurement Between Block and Fingertip

As a method for observing the effect of the presence or absence of tactile sensation, the distance between the thumb and index finger, and the thumb and middle finger when grasping a virtual object is measured. In addition, the distance between the three fingertips of the thumb, index finger, and middle finger and the midpoint of the virtual object is measured, and the PWM signal is controlled according to the distance. The PWM signal can be set from 0 to 255. The midpoint coordinates of each fingertip and virtual object. The distance between each fingertip and the midpoint of the virtual object is calculated by the following formula:

Table 11.5 Transition of PWM value according to the distance between the virtual fingertip and the virtual object

Distance [%]	PWM value
100–80	100
80–60	135
60–40	170
40–20	205
20–0	240

$$\text{Distance} = \sqrt{\left(Fx_n - Mx\right)^2 + \left(Fy_n - My\right)^2 + \left(Fz_n - Mz\right)^2} \tag{11.1}$$

where Fx_n, Fy_n, and Fz_n, are the position of the fingertip at the time n, respectively. Mx, My, and Mz are the midpoint position of the virtual object.

At this time, the coordinate deviation between Unity and Leap Motion Controller is corrected by multiplying the z-axis coordinate value of each fingertip by -1.

Next, the setting of the PWM signal value will be explained. First, the virtual hand and virtual object are set to slip through. At this time, each time the virtual object is touched, the distance between the touched fingertip and the midpoint of the virtual object is measured and saved. Assuming that the distance is 100%, if the subjects move their fingertip closer to the midpoint of the virtual object after touching it, the PWM value will change in five steps according to the distance. Table 11.5 shows the change in PWM value according to the distance. This is applied with each finger, and the air pump is driven according to the PWM value.

11.4 Experiment

The following experiments were performed on two subjects (male, 23.5 ± 0.5 years old, right-handed). This study was performed on the dominant hand side, and the number of blocks moved to the other section in 60 s was counted in the same way as the actual Box and Block Test. To get used to the operation feeling, the experiment was conducted according to the following flow after setting a practice time of 30 s:

1. Display blocks one by one in the section on the dominant hand side.
2. Grab the block and move it over the partition to the other section.
3. When a block touches the floor of the other section, the count is increased, and the block is erased.
4. Regenerate a new block in the dominant handed section.

The above flow was performed twice for 60 s, with and without gloves. The order was no gloves, yes, no, and yes. The blocks that went out of the compartment were deleted without counting, and a new block was generated again on the dominant

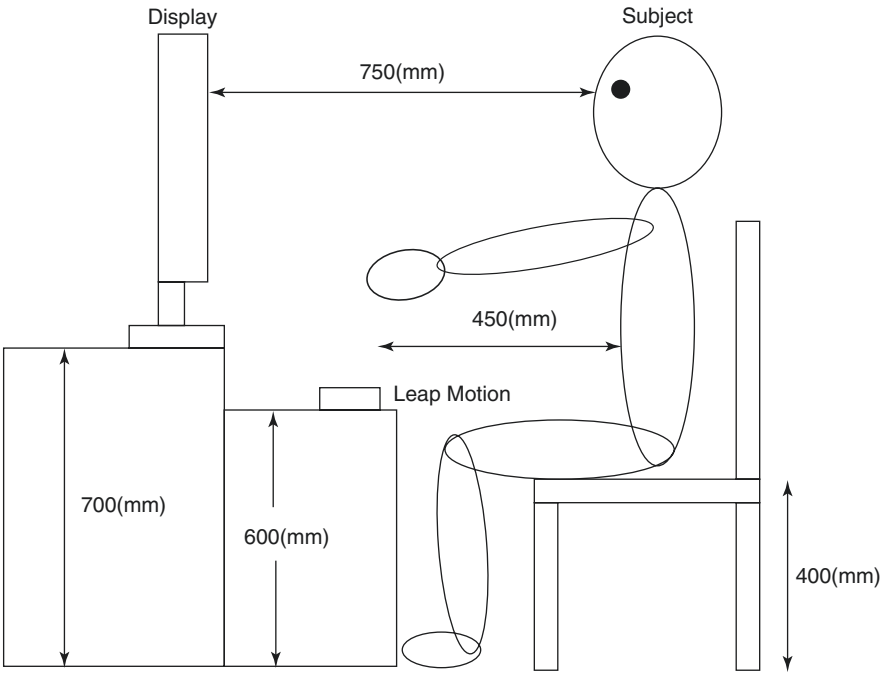

Fig. 11.4 Experimental setup

hand side. In addition, when generating blocks, by setting them to be generated at random positions in the dominant hand side section, it was possible to prevent the blocks from becoming accustomed to repeated operations.

During the experiment, the distances between the index finger and thumb, and the distance between the middle finger and thumb, both with and without gloves, were measured and the data were compared. In addition, the air pump was not driven in five steps by the PWM value, and the measurement was performed in two steps of the PWM value of 180 and 0 in this study.

The experimental environment is shown in Fig. 11.4. Considering the performance of the Leap Motion Controller, install it at a position 100 mm lower than the monitor. Also, by matching the height of the table on which the monitor is placed with the actual desk, it is reproduced as if the Box and Block Test is being performed on the desk.

11.5 Results

The distance between the fingertips in subject # 1 is shown (Figs. 11.5 and 11.6). Horizontal axis (s) is time, and vertical axis is distance (m). Box and Block Test scores were 12 and 20 points, respectively. The longest distance was about 100 mm.

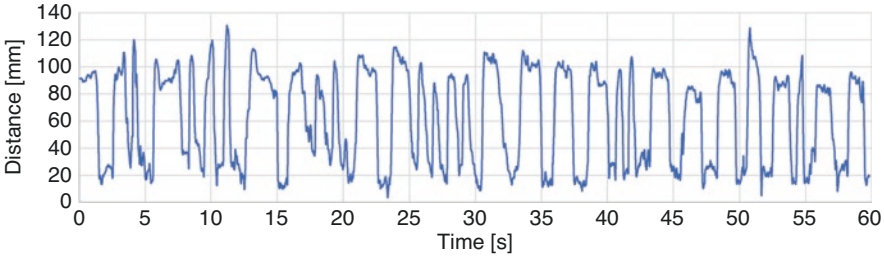

Fig. 11.5 A distance between fingers without the glove

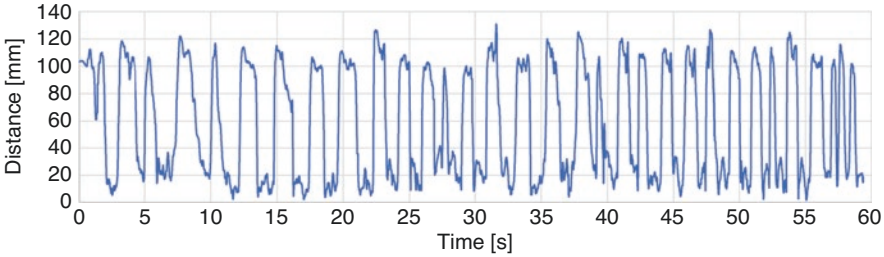

Fig. 11.6 A distance between fingers with the glove

Then, the shortest distance was about 20 mm. Since one side of the block is 40 mm, it can be seen that the subject is holding it.

11.6 Discussions

In both the subjects, the distance between the fingertips while grasping the block in the case of wearing the glove is shorter than that in the case of not wearing the glove. In addition, in subject # 2, when the glove was not attached, the distance was slightly separated from the moment when the block was grasped, but when the glove was attached, the distance from when the block was grasped to when it was released changed. The amount was small. From these, it is considered that when the glove is attached, it is trying to grasp more due to the tactile stimulus. In addition, it is thought that it recognizes the grip of a virtual object and tries to maintain that distance. When humans grip an object, they tend to apply a force between 1.2 and 1.4 times the minimum required gripping force, so they could play a sufficient role as a tactile stimulus. The score of the Box and Block Test was higher than the score with the glove attached and without the glove. However, it is hard to say that the order of the presence or absence of gloves has no effect, so it is necessary to increase the number of subjects and the number of repetitions and continue measurement.

11.7 Conclusion

In this study, we developed a system for measuring the effect of the presence or absence of tactile feedback information in a rehabilitation system using VR technology. For the rehabilitation system, Box and Block Test, which is one of the upper limb function tests, was created on Unity, which is a game engine, and automated. We also aimed to develop a compact pneumatic system using an air pump and latex balloon for tactile stimulation. In the experiment, the distances between the index finger and thumb, and the middle finger and thumb were measured, and the difference in score and distance was calculated in the Box and Block Test on Unity with and without tactile information.

As a result, it was found that the distance between fingertips became shorter in the presence of tactile information. It is considered that this is because the virtual object is being grasped more firmly by the tactile information. In addition, the score also improved, which is related to the ease of grasping. However, due to the small number of data and the characteristics of how to grasp the block depending on the individual, it is necessary to continue measurement. In addition, we believe that the reliability of the data can be improved by performing various measurements such as increasing the size of the block and changing the shape.

The experimental environment needs to be more like the original Box and Block Test experimental environment. In this study, when the Box and Block Test was displayed on the monitor, the viewpoint was projected on the monitor as if it were an actual Box and Block Test. However, in the experimental environment, the experiment was conducted while stretching the arms and looking at the boxes and blocks displayed on the monitor, and there was a discrepancy between the actual line of sight and the line of sight in the monitor, so it is necessary to correct it. In terms of giving a more immersive feeling, it is easy to suppress the deviation of the viewpoint by using a head-mounted display or AR technology. In addition, since there are ways to grip blocks not only with the fingertips but also with the entire hand, the prospect is to create a device that can give tactile stimuli over a wider range, such as the palm side or the dorsal side of the palm.

References

1. Ministry of Internal Affairs and Communications. Statistical Topics No. 126, Elderly People in Japan from the Viewpoint of Statistics; 2020.
2. https://www.mhlw.go.jp/content/12000000/000549665.pdf. Accessed 10 Dec 2020.
3. Imam B, Jarus T. Virtual reality rehabilitation from social cognitive and motor learning theoretical perspectives in stroke population. Hindawi. 2014;7.
4. Mathiowetz V, Volland G, Kashman N, Weber K. Adult norms for the box and block test of manual dexterity. Am J Occup Ther. 1985;39:386–91.

5. Weichert F, Bachmann D. Bartholom aus Rudak and Denis Fisseler. Analysis of the accuracy and robustness of the leap motion controller. Sensors. 2013;6391.
6. https://www.ultraleap.com/datasheets/Leap_Motion_Controller_Datasheet.pdf. Accessed 10 Dec 2020.
7. Guna J, Jakus G, Pogačnik M, Tomažič S, Sodnik J. An analysis of the precision and reliability of the leap motion sensor and its suitability for static and dynamic tracking. Sensors. 2014;3705.

Chapter 12
Artificial Intelligence for Medical Imaging and Hygiene

Akihiro Sugiura

Abstract Artificial Intelligence (AI) is commonly defined as machine intelligence that is programmed to think like humans and emulate their behavior or simply the technology of developing AI. People receive great benefits from services based on AI technology without even realizing it. One of the technologies that underlie AI is machine learning, and deep learning is a new type of machine learning. Mathematical models of deep learning usually employ a neural network model that imitates the human brain neural network, and a deep neural network has some middle layers to solve the highly difficult issues. A Convolutional Neural Network (CNN), which is a type of deep learning network, can analyze an image directly. In the field of medical imaging and diagnosis, deep learning is already being used to solve numerous difficult issues. Systems have been developed using CNNs and have achieved practical medical application. This chapter focuses in detail on the relationship between deep learning, medical imaging, and hygiene. In particular, it contains an explanation and technical summary of machine learning, the application of deep learning in medical imaging, and the association of the Coronavirus disease 2019 (COVID-19) infection with hygiene and deep learning.

Keywords Deep learning · Convolutional neural network (CNN) · Medical imaging · Coronavirus disease 2019 (COVID-19)

A. Sugiura (✉)
Department of Radiological Technology, Gifu University of Medical Science Seki, Gifu, Japan
e-mail: asugiura@u-gifu-ms.ac.jp

H. Takada, K. Yokoyama (eds.), *Bio-information for Hygiene*, Current Topics in Environmental Health and Preventive Medicine,
https://doi.org/10.1007/978-981-15-2160-7_12

12.1 Introduction

In recent years, Artificial Intelligence (AI) has attracted a significant amount of attention. It has already been utilized in numerous fields owing to its vast potential for technological innovation. People are already receiving great benefits from some services based on AI without even realizing it. For example, image recognition technology such as auto-detection or auto-classification techniques can recognize components (e.g., humans, background, or structural objects such as vehicles) and their positions in a picture or image, using image analysis. There is also the auto-recognition of handwriting characters, and voice recognition that can recognize spoken words, which can then be converted to text. Virtual assistance services such as Siri™ and Google Assistant™ use embedded AI.

AI is commonly defined as machine intelligence that is programmed to "think" like humans and emulate their behavior, or simply the technology of developing AI, although AI does have some other similar interpretations. One of the technologies underlying AI is machine learning, and there is a new type of machine learning called deep learning, which is the core technology behind the current third wave of AI development. Specific technologies for AI are depicted hierarchically in Fig. 12.1 (and explained in detail in the next section). In the second wave of AI that continued into the late 1990s, some feature amounts of a target object such as an image or voice were manually extracted. Then, the target object was categorized by machine learning using the extracted feature amounts. In contrast, the use of deep learning proposed by Hilton et al. was to extract a set of feature amounts; however, this was done automatically (Fig. 12.2) [1, 2]. Thus, deep learning has a better performance and is easier to apply than conventional machine learning. Generally, a huge volume of data is required for training a deep learning network. Expansion of the Internet has enabled the accumulation of data and knowledge (e.g., images and documents). Much of the data for deep learning possessed by online businesses and institutions has also become available at no cost. In addition, drastic increases in processing

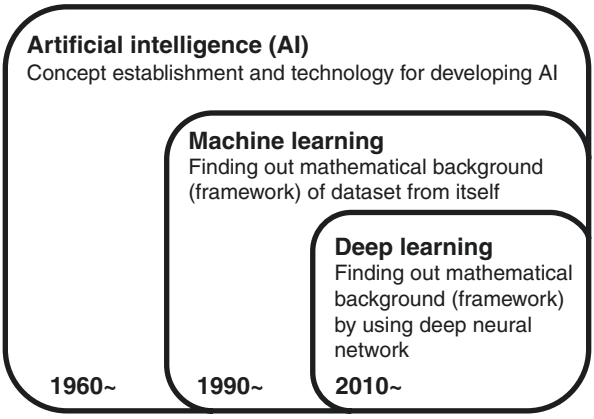

Fig. 12.1 Transition of concepts and technology in AI

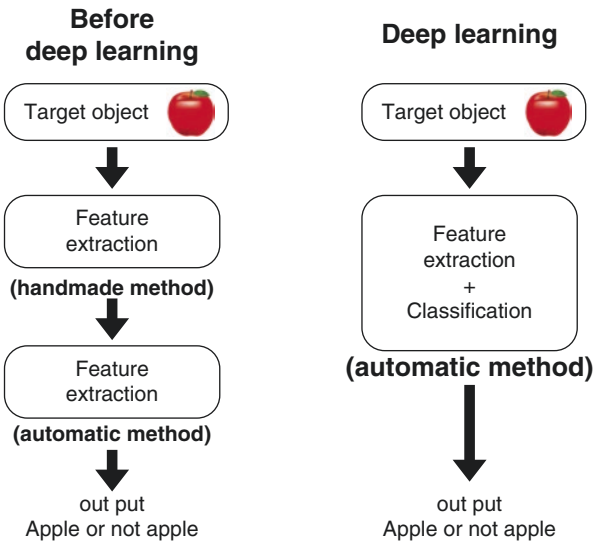

Fig. 12.2 Comparison of processing steps before and after the development of deep learning

capabilities of computers has enabled the use of deep learning. Consequently, several researchers now use deep learning to address their research problems.

In the field of medical imaging and diagnosis, deep learning has been used to address challenging issues. Some systems with practical medical applications have also been developed. This chapter focuses on the relationship between deep learning, medical imaging, and hygiene. In particular, this chapter provides a technical summary of machine learning, the application of deep learning in medical imaging, and also its application with the Coronavirus disease 2019 (COVID-19) infection and hygiene.

12.2 Basis for Deep Learning in Medical Imaging

Machine learning, which is one of the fundamental technologies for AI, requires that the machine identifies regularity or patterns in underlying data. Humans or machines need to manually or automatically extract the characteristics of the input data as mathematical values, then classify the input data or predict the output from the input data. In some cases, they also find new knowledge or interpret the mathematical framework associated with the input data. To perform classification or prediction, supervised learning is applied wherein the labeled data is used as input data during training. In this case, "labeled" may be used to refer to attributed, grouped, or known output values (i.e., a known relationship between x and $f(x)$ in a function). The mathematical model in machine learning is optimized during training using these labeled datasets to find the most optimized state yielding the minimum error. After training, the unlabeled data are used as input to the trained mathematical

model, to obtain new classification or prediction results. Alternatively, to test and model the mathematical structure of datasets, unsupervised learning is required wherein unlabeled data are used as input. Here, "unlabeled" may be used to refer to unattributed, ungrouped, or unknown output values. Unsupervised learning defines criteria that classify such uncategorized data. More specifically, in unsupervised learning, the amounts of the features that can represent the mathematical framework of the dataset, are extracted from each of the datasets. Next, a mathematical model of the feature amounts is constructed to group each set of data into clusters. Finally, each group is named (to give it a meaning).

One of the mathematical models in the field of machine learning is the neural network model that imitates the neural network of the human brain. In the human brain, brain neurons propagate action potential to a few adjacent neurons in sequence through the synapses of the dendrite segment. During the propagation action potential, signal transfer is weighted depending on the importance of the information. These mechanisms are the basis of an artificial neural network model. The neural network generally has a hierarchical architecture called multilayer perceptron (at least three or more layers including both input and output layers). Figure 12.3 shows a schematic of a neural network model. The white circles represent the nodes (artificial neurons), and the neural network has multiple layers: input layer, middle (hidden) layers, and output layer. The input data in the input layer propagates, and the parameters for weighting of the middle layer are adjusted to obtain the calculation results in the output layer. During training, the weighting factor of each edge is adjusted as the model is tuned to obtain the minimum error, which is the gap between the model output from the label and the actual output from the optimized model. The backpropagation method proposed by Hinton is also frequently applied during model tuning [3].

The neural network model that has a number of middle layers is called a deep neural network [1, 2]. Compared to the traditional neural network, a deep neural network can overcome poor optimization problems, which are attributed to multi-middle-layer models, e.g., the vanishing gradient problem [4]: which does not adequately correct the weighting factor of the edge near the input layer in the multilayer

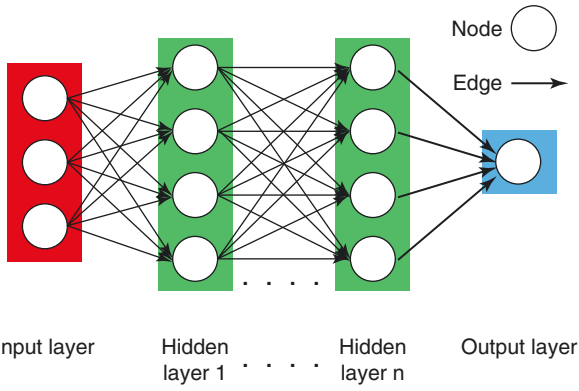

Fig. 12.3 Schematic diagram of the neural network model

neural network. Various types of deep learning models have been developed so far. One of these models is the Convolutional Neural Network (CNN) [5, 6], which has usually been associated with human vision sense. The CNN can input an image directly. In addition, as an example of the CNN as depicted in Fig. 12.4, the CNN can extract some feature values from unstructured data such as images, by a set of convolutional layers and a pooling layer in the middle layers. The convolutional layers create feature maps made from brightness or outline information by convolutional operation. Then, a pooling layer decreases in the feature maps by down-sampling to be more robust to changes in the position of the feature in the image and a decrease in processing costs. A fully connected layer recognizes input data, such as image classification, from these feature maps. The CNN is frequently utilized in image classification, target object detection, image segmentation, and regression tasks. The major CNN architectures are listed in Table 12.1. The conventional neural network is used to solve the regression task and a CNN is used in the case of addressing the regression task for an image.

One of the unsupervised learning models is the Generative Adversarial Network (GAN) proposed by Goodfellow in 2014 [18]. The GAN generates virtual data similar to real data or performs data conversion by learning the features of real datasets. This unique deep learning model has recently attracted public attention owing to its potentially wide application. Figure 12.5 shows an outline drawing of a typical GAN. The GAN composed of different neural networks: one is the generator and the other the discriminator, both of which are antagonistically connected. The generator creates an artificial image similar to a real image by creating the generated image added noise components. In contrast, the discriminator distinguishes whether

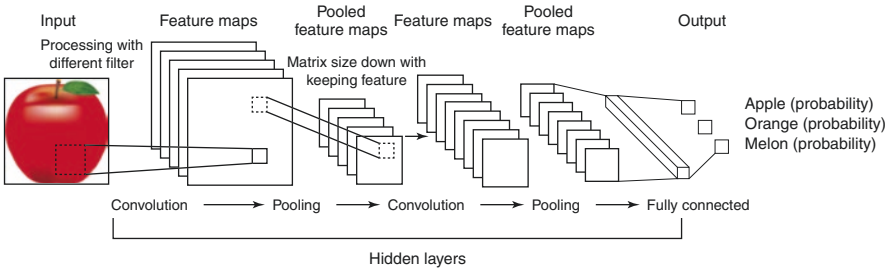

Fig. 12.4 Processing flow and construction of the convolutional neural network

Table 12.1 Major CNN architecture

Task	Network architecture
Classification	Lenet [5], AlexNet [2], VGGnet [7], GoogleNet [8], ResNet [9]
Detection	R-CNN [10], Fast R-CNN [11], Faster R-CNN [12], SSD [13]
Segmentation	FCN [14], SegNet [15], U-Net [16], V-Net [17]

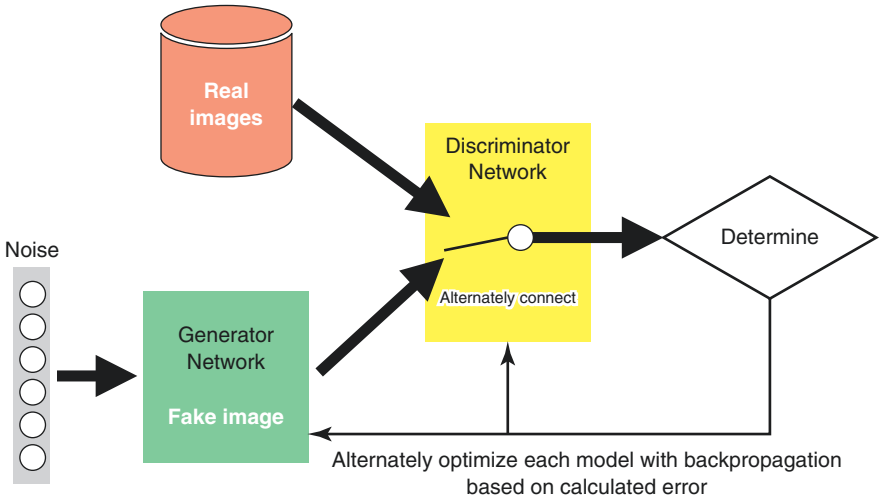

Fig. 12.5 Generating real-fake images by the generative adversarial network

the image is real or generated, by comparing the generated image to a real one. The discriminator and generator are trained in an alternative manner (model optimization). During discriminator training, the model is optimized to determine that the real training image is true, and the generated image is false. In contrast, during generator training the model is optimized to determine that the generated image is true. In this way, the repeated adversarial learning generates an identical generated image. The original type of GAN has a problem in that the generated image potentially blurs [19]. However, the deep convolutional GAN (DCGAN) [19], which is a modified version of the GAN, generates a clear image because DCGAN improves this problem by correcting the model architecture and changing the method for the weighting factor adjustment.

12.3 Application of Artificial Intelligence in Medical Imaging

On July 14, 2020, a search of PubMed returned 15,037 hits for the words "Deep learning", and 9,467 hits for the words "Convolutional Neural Network" or "CNN." In addition, the number of published papers has increased exponentially since 2014—the numbers in 2014, 2017, and 2018 were less than 1,000, 2,000, and 4,000 respectively, and in 2019 alone it was over 7,000. In annual medical meetings of the Radiological Society of North America, the number of registered abstracts for machine learning has also drastically increased. This situation indicates that machine learning (especially deep learning) is the center of the research target in medical imaging and diagnosis fields. As described earlier, the CNN can carry out image classification, target object detection, and image segmentation. The next three sections present application cases for each of these technologies.

12.3.1 Classification

The classification task in medical imaging is to clearly separate normal and abnormal images. Only doctors with specialist knowledge can perform this type of task as a diagnosis. In the current medical system, machine learning is expected to support the doctors in this type of task (classification). The feature of supervised learning is that classification by machine learning follows the doctor's diagnostic criteria because the label (supervisor) of the training data is absolutely the doctor's diagnosis. The following describes particular cases in past studies on the classification of medical images.

- Yasaka et al. reported the differentiation of liver images using dynamic computed tomography (CT) (plain, enhanced arterial phase, and enhanced late-phase) [20]. Many cases were diagnosed according to five categories (category A, classic hepatocellular carcinomas (HCCs); category B, malignant liver tumors other than classic and early HCCs; category C, indeterminate masses or mass-like lesions and rare benign liver masses other than hemangiomas and cysts; category D, hemangiomas; and category E, cysts). In the training phase, 55,536 images (including data augmentation) were used for training. A total of 100 images were categorized in the testing phase. As a result, the median diagnostic accuracy and area under curve (AUC) in receiver operating characteristic (ROC) [21] analysis were 0.84 and 0.92, respectively.
- Abiyev et al. reported that they demonstrated the feasibility of classifying typical chest pathologies in chest X-rays [22]. The chest X-rays were divided into 12 image findings: atelectasis, cardiomegaly, consolidation, edema, effusion, emphysema, fibrosis, infiltration, mass, nodule, pneumonia, and pneumothorax. In the training phase, 84,084 images (70% of 120,120 images available) were used for training. A total of 36,036 images (30% of 120,120 images available) were classified in the testing phase. As a result, the diagnostic accuracy of the proposed network was 0.924, and the prediction accuracy of the mass was approximately 0.95.
- Gorji et al. reported that they classified mild cognitive impairment (MCI) from brain images scanned with magnetic resonance imaging (MRI) (sagittal, axial, and coronal view) [23]. Brain MRI images were divided into three groups according to the diagnostic level (normal, early MCI, and late MCI). In the training phase, this study used 8,400 images (70% of 12,000 images available (including data augmentation)) in each view. A total of 3,600 images (30% of 12,000 images available (including data augmentation)) were classified in the testing phase. As a result, diagnostic accuracy and the AUC between the normal group and the late MCI group in the sagittal view were 0.9454 and 0.994, respectively (best result). In addition, results between the early MCI and late MCI, and between the normal and the early MCI were also highly accurate: diagnostic accuracy was 0.93 and 0.9396, and AUC was 0.981 and 0.988, respectively.
- Liu et al. reported the differentiation of nodule patch images extracted from lung CT images [24]. The nodule patches were separated into three groups (benign, primary malignant, and metastatic malignant). This study used 47,716 images

(including data augmentation) and ran 10-fold cross validation five times. In addition, patch images from an original multi-view CNN (which extracted some patches from one nodule using different matrix sizes) were applied as input data to reduce the error rate. As a result, their model achieved an error rate of 0.139 for ternary classifications.

- Esteva et al. reported that they demonstrated classification of skin lesions [25]. The skin lesion images were divided into three groups (benign lesions, malignant lesions, and nonneoplastic lesions). In the training, this study used 127,463 images including 757 types of diseases and ran a 10-fold cross validation. In addition, they utilized a GoogleNet Inception v3 [26] architecture trained using transfer learning. A total of 1,942 images were classified in the testing phase. As a result, the average accuracy of the CNN was 0.721, and two dermatologists attained 0.6556 and 0.66, respectively. As can be seen, the CNN achieved a high accuracy for the classification task.

12.3.2 Detection

The detection task in medical imaging is to locate and detect suspected abnormal image findings. This type of task is also exclusively performed by doctors. There is a fear that oversight may occur due to the diagnostic reading environment or differences in the skill level of reading. Thus, machine learning is expected to support the prevention of oversight as a safety net. The following are particular cases in related studies on detection.

- Zhang et al. proposed a system that detected lung tumor candidates in positron emission tomography (PET) images [27], based on the Mask R-CNN (modified R-CNN) [28]. This system consisted of three different Mask R-CNN's in terms of a multi-scale input image. Images with three different scales were used to produce three kinds of training data with resolutions of 512 × 512, 768 × 768, and 1,024 × 1,024, respectively. Moreover, these three Mask R-CNN models were then integrated using a weighted voting strategy to diminish the false-positive outcomes. This study used 594 images of lung cancer in the training phase. Then, 134 images were employed as the test set in the test phase. The precision, recall, and F-value of the system were 0.90, 1, and 0.95, respectively.
- Chiao et al. proposed a system that included detection, segmentation, and differentiation functions (benign or malignant) of breast cancer ultrasound images based on the Mask R-CNN [29]. In the training phase, 246 images (80% of 307 images available) were used. In testing the proposed system, 61 images (20% of 307 images available) were used. The mean average precision accuracy of lesion detection/segmentation was 0.75. In addition, the accuracy in this test of benign–malignant classification of breast cancers was 0.85.
- Ribli et al. proposed a detection system for breast cancer mammograms based on the Faster R-CNN [30]. The system detected and classified malignant or benign

lesions on mammograms. This study in the training phase used 2620 images. In addition, their system utilized transfer learning using 1.2 million images from the ImageNet as pre-training. A total of 115 images (of which 8 images were excluded) were detected and classified in the testing phase. The results of the test were that the system achieved 0.95 of AUC, and was able to detect 90% of the malignant lesions with only 0.3 false-positive marks per image.

- Couteaux et al. reported classifying MRI images of the knee with respect to the presence of tears in the knee menisci, meniscal tear location, and meniscal tear orientation by using the Mask R-CNN [31]. In the training, 1,124 images were used (excluding poor quality images), including normal cases and tears in various directions. A total of 700 images were used to test the proposed method. Consequently, the weighted average of the AUC considering the detection task, the tear localization task, and the orientation classification task, was 0.906.

As mentioned above, many detection tasks have achieved high precision by employing R-CNN and its improvement methods. In addition, as one can see from the case examples, the system simulated image diagnosis process was usually developed because the system combined both the detection and the classification functions.

12.3.3 Segmentation

For the segmentation task, a high accuracy of automatic area extraction is required compared to the detection task. In medical imaging, targets of segmentation are frequently the organs or affected areas. Further, accurate segmentation has many advantages, such as accurate understanding of treatment area, acquisition of qualitative data, and exclusion of unwanted areas. The following describes particular cases in related studies on segmentation:

- Bai et al. reported the auto-analysis of cardiac functions with cardiovascular MRI images by using a fully convolutional network (FCN), which is a type of neural network that can predict pixel-wise image segmentation by applying a number of convolutional filters onto an input image [32]. In this study, 3975 images were used for the training, 300 for the validation, and 600 for the testing. The performance of the automated method was evaluated in two ways: (a) using commonly used metrics for segmentation accuracy assessment, including the Dice metric (Dice coefficient) [33], mean contour distance and Hausdorff distance, and (b) using clinical heart function measures derived from segmentations, including ventricular volume and mass. The results indicated that an automated method achieves a performance on par with human experts in analyzing images and deriving clinically relevant measures.
- Cui et al. presented a fully automatic segmentation method for five types of brain MRI images containing brain gliomas [34]. Their approach could not only localize the entire tumor region, but could also accurately segment the intra-tumor

structure according to classes (necrosis, edema, non-enhancing tumor, and enhancing tumor). Their proposed system was based on a cascaded deep convolutional neural network consisting of two subnetworks: a tumor localization network based on the FCN with transfer learning, and an intra-tumor classification network based on the CNN. The training in the tumor localization used 240 cases and a 10-fold cross validation was run. Training in the intra-tumor classification used 4,700,000 image patches labeled into four classes. They conducted quantitative evaluations of three different tumor regions: complete tumor region (including all four tumor subregions), core tumor region (including all tumor structures except edema), and enhancing tumor region (only including the enhanced tumor structure). As a result, the dice metrics for complete, core, and enhancing tumors using the proposed approach were 0.89, 0.77, and 0.8, respectively. These results were comparable and in general better than other methods reported in the literature.

- Shahedi et al. developed an automatic, three-dimensional (3-D) prostate segmentation algorithm based on a customized U-Net, which is a type of FCN [35]. In the training phase, abdominal CT images of 69 patients (75% of all images available) were used and applied that of 23 patients (25% of all images) in the test phase. A feature of their study was that both two doctors segmented the prostate per image. In each phase, being training, validation, and testing, they also verified the difference in methods used for annotation. In addition, the effect of the image artifact on the segmentation of the prostate was also evaluated. In particular, the latter evaluation is worthy of a special mention because the difference in the dice metric between images with and without artifacts was only 1.2%.

12.3.4 Secure Medical Images for Deep Learning

Generally, research or development on medical imaging with deep learning requires a huge quantity of images for training to optimize the network model. The medical images are different from general pictures in terms of strict ethical requirements and the difficulty of obtaining these images without any conditions. Moreover, as mentioned earlier, although tasks with supervised learning, such as classification, detection, and segmentation, require work for labeling and annotation in each data, only doctors can practically perform these tasks. Hence, research or development on medical imaging with deep learning tends to require huge costs and takes a lot of time. To overcome this hindrance, medical image databases with labels or annotations have been constructed on a worldwide scale [36–39]. This kind of database is now publicly available for research or development if certain conditions are met. The advantage of utilizing a public medical image database is not only a decrease in the various costs for obtaining a huge quantity of medical images with labels or annotations, but also that it is easy to directly compare the work with related studies that apply the same database. Hence, constructing a public database for medical

images is as important as the design and development of the deep learning neural network.

The training in deep learning has increased in learning accuracy due to data augmentation using processed images or virtual images [2, 7–9, 40, 41]. The image processing includes such techniques as image rotation, flipping horizontally, and changes in image contrast. In the case of lack of images for training, data augmentation with image processing has been utilized because this method is generally accepted. Alternatively, studies with virtual images have used the GAN that generates many similar images for training. This method also achieves the desired result [42, 43].

12.4 Artificial Intelligence and Hygiene

Recently, the Coronavirus disease 2019 (COVID-19) infection has spread worldwide. The outbreak was first identified in December 2019 in the city of Wuhan in China [44]. As of July 8, 2020, the number of COVID-19 infected patients is 11,761,578, and the number of deaths is 543,259. Since World War II, COVID-19 has been one of the gravest threats to humanity, but the spread of the disease has also been attributed to various reasons such as delay in the detection of latent carriers and those with no symptoms, poor activity restriction, and improper quarantine. To restrict the spread of COVID-19, strict rules are currently being implemented with regard to hygiene.

Major CT scan findings of COVID-19 infections are as follows bilateral and peripheral distribution, ground glass opacity, consolidation, and air bronchogram and so on [45, 46] (Fig. 12.6). These CT findings are not specific to COVID-19 infections, because they are similar to those found with virus pneumonia. Hence, it is suggested that diagnostic CT imaging alone should not be used for COVID-19

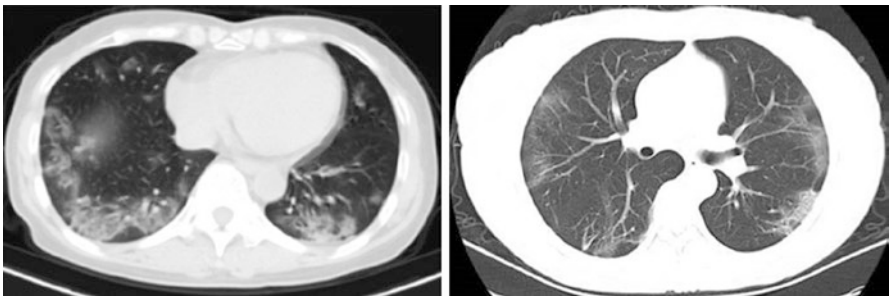

Fig. 12.6 Typical chest CT images of patients with COVID-19. Used with permission from "COVID-CT-Dataset: A CT Image Dataset about COVID-19 by X. Yang, X. He, J. Zhao, Y. Zhang, S. Zhang & P. Xie, published in June 2020"

primary diagnosis and screening. It is considered more useful to rather follow the pulmonary and recovery processes [46]. Accumulation of CT findings in COVID-19 infections following the recent increase in cases can contribute to an understanding of the details of the lesion by the creation of a large amount of data. Studies on COVID-19 using deep learning are already being conducted using this enormous amount of data. Until now, most attempts have been aimed at differentiating chest CT images with COVID-19 pneumonia or its detection [47–54]. The ultimate common goal of the studies thus conducted using deep learning is to support the medical staff with the overwhelming number of COVID-19 cases.

12.5 Conclusion

In this chapter, a technical summary and description of the application of deep learning, which is the main technology used for analyzing medical images was presented. Various related studies were reviewed. In addition, the present status of the COVID-19 disease and characteristics of its CT images were explained. Furthermore, the role of deep learning in medical imaging was discussed. Hardware and deep learning applications that are being practically used in the medical field already exist. It is only a matter of time before these systems can achieve universal prevalence. We look forward to future developments using deep learning. If additional professional and technical information is required, the reader should consult specialized books on deep learning.

References

1. Hinton GE, Salakhutdinov RR. Reducing the dimensionality of data with neural networks. Science. 2006;313:504–7. https://doi.org/10.1126/science.1127647.
2. Krizhevsky A, Sutskever I, Hinton GE. ImageNet classification with deep convolutional neural networks. In: Pereira F, Burges CJC, Bottou L, Weinberger KQ, editors. Advances in neural information processing systems 25. New York: Curran Associates; 2012. p. 1097–105.
3. Rumelhart DE, Hinton GE, Williams RJ. Learning representations by back-propagating errors. Nature. 1986;323:533–6. https://doi.org/10.1038/323533a0.
4. Hochreiter S. The vanishing gradient problem during learning recurrent neural nets and problem solutions. Int J Uncertain Fuzziness Knowledge-Based Syst. 1998;6:107–16. https://doi.org/10.1142/S0218488598000094.
5. Lecun Y, Bottou L, Bengio Y, Haffner P. Gradient-based learning applied to document recognition. Proc IEEE. 1998;2278–324. https://doi.org/10.1109/5.726791.
6. Le Cun Y, Denker JS, Henderson D, Howard RE, Hubbard W, Jackel LD. Handwritten digit recognition with a back-propagation network. Adv Neural Inf Process Syst. 1989;2:396–404.
7. Simonyan K, Zisserman A. Very deep convolutional networks for large-scale image recognition. 2015. arXiv preprint arXiv:1409.1556.
8. Szegedy C, Wei L, Yangqing J, Sermanet P, Reed S, Anguelov D, et al. Going deeper with convolutions. 2015 IEEE conference on computer vision pattern recognition. 2015. p. 1–9. https://doi.org/10.1109/CVPR.2015.7298594.

9. He K, Zhang X, Ren S, Sun J. Deep residual learning for image recognition. In: 2016 IEEE conference on computer vision pattern recognition. 2016. p. 770–8. https://doi.org/10.1109/CVPR.2016.90.
10. Girshick R, Donahue J, Darrell T, Malik J. Rich feature hierarchies for accurate object detection and semantic segmentation. In: 2014 IEEE conference on computer vision pattern recognition. 2014. p. 580–7. https://doi.org/10.1109/CVPR.2014.81.
11. Girshick R. Fast R-CNN. In: 2015 IEEE International conference on computer vision. 2015. p. 1440–8. https://doi.org/10.1109/ICCV.2015.169.
12. Ren S, He K, Girshick R, Sun J. Faster R-CNN: towards real-time object detection with region proposal networks. IEEE Trans Pattern Anal Mach Intell. 2017;39:1137–49. https://doi.org/10.1109/TPAMI.2016.2577031.
13. Liu W, Anguelov D, Erhan D, Szegedy C, Reed S, Fu C-Y, et al. SSD: single shot MultiBox detector. Lecture notes on computer science (including subseries Lecture Notes in Artificial Intelligence and Lecture Notes in Bioinformatics). 2016. p. 21–37. https://doi.org/10.1007/978-3-319-46448-0_2.
14. Shelhamer E, Long J, Darrell T. Fully convolutional networks for semantic segmentation. IEEE Trans Pattern Anal Mach Intell. 2017;39:640–51. https://doi.org/10.1109/TPAMI.2016.2572683.
15. Badrinarayanan V, Kendall A, Cipolla R. SegNet: a deep convolutional encoder-decoder architecture for image segmentation. IEEE Trans Pattern Anal Mach Intell. 2017;39:2481–95. https://doi.org/10.1109/TPAMI.2016.2644615.
16. Ronneberger O, Fischer P, Brox T. U-Net: convolutional networks for biomedical image segmentation. Lectures Notes on Computer Science (including subseries Lecture Notes in Artificial Intelligence and Lecture Notes in Bioinformatics). 2015. p. 234–41. https://doi.org/10.1007/978-3-319-24574-4_28.
17. Milletari F, Navab N, Ahmadi S-A. V-Net: fully convolutional neural networks for volumetric medical image segmentation. In: 2016 fourth international conference on 3D vision. 2016. p. 565–71. https://doi.org/10.1109/3DV.2016.79.
18. Goodfellow IJ, Pouget-Abadie J, Mirza M, Xu B, Warde-Farley D, Ozair S, et al. Generative adversarial networks. 2014. arXiv preprint arXiv:1406.2661.
19. Radford A, Metz L, Chintala S. Unsupervised representation learning with deep convolutional generative adversarial networks. 2016. arXiv preprint arXiv:1511.06434.
20. Yasaka K, Akai H, Abe O, Kiryu S. Deep learning with convolutional neural network for differentiation of liver masses at dynamic contrast-enhanced CT: a preliminary study. Radiology. 2018;286:887–96. https://doi.org/10.1148/radiol.2017170706.
21. Fawcett T. An introduction to ROC analysis. Pattern Recogn Lett. 2006;27:861–74. https://doi.org/10.1016/j.patrec.2005.10.010.
22. Abiyev RH, Ma'aitah MKS. Deep convolutional neural networks for chest diseases detection. J Healthc Eng. 2018;2018:4168538. https://doi.org/10.1155/2018/4168538.
23. Gorji HT, Kaabouch N. A deep learning approach for diagnosis of mild cognitive impairment based on MRI images. Brain Sci. 2019;9:217–30. https://doi.org/10.3390/brainsci9090217.
24. Liu K, Kang G. Multiview convolutional neural networks for lung nodule classification. Int J Imaging Syst Technol. 2017;27:12–22. https://doi.org/10.1002/ima.22206.
25. Esteva A, Kuprel B, Novoa RA, Ko J, Swetter SM, Blau HM, et al. Dermatologist-level classification of skin cancer with deep neural networks. Nature. 2017;542:115–8. https://doi.org/10.1038/nature21056.
26. Szegedy C, Vanhoucke V, Ioffe S, Shlens J, Wojna Z. Rethinking the inception architecture for computer vision. 2016 IEEE conference on computer vision pattern recognition. 2016. p. 2818–26. https://doi.org/10.1109/CVPR.2016.308.
27. Zhang R, Cheng C, Zhao X, Li X. Multiscale mask R-CNN-based lung tumor detection using PET imaging. Mol Imaging. 2019;18:1–8. https://doi.org/10.1177/1536012119863531.
28. He K, Gkioxari G, Dollar P, Girshick R. Mask R-CNN. 2017 IEEE international conference on computer vision 2017. p. 2980–8. https://doi.org/10.1109/ICCV.2017.322.

29. Chiao JY, Chen KY, Liao KYK, Hsieh PH, Zhang G, Huang TC. Detection and classification the breast tumors using mask R-CNN on sonograms. Medicine. 2019;98:e15200. https://doi.org/10.1097/MD.0000000000015200.
30. Ribli D, Horváth A, Unger Z, Pollner P, Csabai I. Detecting and classifying lesions in mammograms with deep learning. Sci Rep. 2018;8:4165. https://doi.org/10.1038/s41598-018-22437-z.
31. Couteaux V, Si-Mohamed S, Nempont O, Lefevre T, Popoff A, Pizaine G, et al. Automatic knee meniscus tear detection and orientation classification with mask-RCNN. Diagn Interv Imaging. 2019;100:235–42. https://doi.org/10.1016/j.diii.2019.03.002.
32. Bai W, Sinclair M, Tarroni G, Oktay O, Rajchl M, Vaillant G, et al. Automated cardiovascular magnetic resonance image analysis with fully convolutional networks. J Cardiovasc Magn Reson. 2018;20:65–76. https://doi.org/10.1186/s12968-018-0471-x.
33. Dice LR. Measures of the amount of ecologic association between species. Ecology. 1945;26:297–302. https://doi.org/10.2307/1932409.
34. Cui S, Mao L, Jiang J, Liu C, Xiong S. Automatic semantic segmentation of brain gliomas from MRI images using a deep cascaded neural network. J Healthc Eng. 2018;2018:4940593. https://doi.org/10.1155/2018/4940593.
35. Shahedi M, Halicek M, Dormer JD, Schuster DM, Fei B. Deep learning-based three-dimensional segmentation of the prostate on computed tomography images. J Med Imaging. 2019;6:025003. https://doi.org/10.1117/1.JMI.6.2.025003.
36. Armato SG, McLennan G, Bidaut L, McNitt-Gray MF, Meyer CR, Reeves AP, et al. The lung image database consortium (LIDC) and image database resource initiative (IDRI): a completed reference database of lung nodules on CT scans. Med Phys. 2011;38:915–31. https://doi.org/10.1118/1.3528204.
37. Shiraishi J, Katsuragawa S, Ikezoe J, Matsumoto T, Kobayashi T, Komatsu K, et al. Development of a digital image database for chest radiographs with and without a lung nodule: receiver operating characteristic analysis of radiologists' detection of pulmonary nodules. AJR Am J Roentgenol. 2000;174:71–4. https://doi.org/10.2214/ajr.174.1.1740071.
38. Moreira IC, Amaral I, Domingues I, Cardoso A, Cardoso MJ, Cardoso JS. INbreast: toward a full-field digital mammographic database. Acad Radiol. 2012;19:236–48. https://doi.org/10.2214/ajr.174.1.1740071.
39. Menze BH, Jakab A, Bauer S, Kalpathy-Cramer J, Farahani K, Kirby J, et al. The multimodal brain tumor image segmentation benchmark (BRATS). IEEE Trans Med Imaging. 2015;34:1993–2024. https://doi.org/10.1109/TMI.2014.2377694.
40. Huang G, Liu Z, Van Der Maaten L, Weinberger KQ. Densely connected convolutional networks. In: 2017 IEEE conference computer vision pattern recognition; 2017. p. 2261–9. https://doi.org/10.1109/CVPR.2017.243.
41. Sorin V, Barash Y, Konen E, Klang E. Creating artificial images for radiology applications using generative adversarial networks (GANs) – a systematic review. Acad Radiol. 2020;27:1175–85. https://doi.org/10.1016/j.acra.2019.12.024.
42. Frid-Adar M, Diamant I, Klang E, Amitai M, Goldberger J, Greenspan H. GAN-based synthetic medical image augmentation for increased CNN performance in liver lesion classification. Neurocomputing. 2018;321:321–31. https://doi.org/10.1016/j.neucom.2018.09.013.
43. Onishi Y, Teramoto A, Tsujimoto M, Tsukamoto T, Saito K, Toyama H, et al. Automated pulmonary nodule classification in computed tomography images using a deep convolutional neural network trained by generative adversarial networks. Biomed Res Int. 2019;2019:6051939. https://doi.org/10.1155/2019/6051939.
44. Hui DS, Azhar E, Madani TA, Ntoumi F, Kock R, Dar O, et al. The continuing 2019-nCoV epidemic threat of novel coronaviruses to global health – the latest 2019 novel coronavirus outbreak in Wuhan. China Int J Infect Dis. 2020;91:264–6. https://doi.org/10.1016/j.ijid.2020.01.009.
45. Zu ZY, Di Jiang M, Xu PP, Chen W, Ni QQ, Lu GM, et al. Coronavirus disease 2019 (COVID-19): a perspective from China. Radiology. 2020;296:E15–25. https://doi.org/10.1148/radiol.2020200490.
46. Sun Z, Zhang N, Li Y, Xu X. A systematic review of chest imaging findings in COVID-19. Quant Imaging Med Surg. 2020;10:1058–79. https://doi.org/10.21037/qims-20-564.

47. Jaiswal A, Gianchandani N, Singh D, Kumar V, Kaur M. Classification of the COVID-19 infected patients using DenseNet201 based deep transfer learning. J Biomol Struct Dyn. 2020;1–8. https://doi.org/10.1080/07391102.2020.1788642.
48. Ko H, Chung H, Kang WS, Kim KW, Shin Y, Kang SJ, et al. COVID-19 pneumonia diagnosis using a simple 2D deep learning framework with a single chest CT image: model development and validation. J Med Internet Res. 2020;22:e19569. https://doi.org/10.2196/19569.
49. Ardakani AA, Kanafi AR, Acharya UR, Khadem N, Mohammadi A, Abbasian A, et al. Application of deep learning technique to manage COVID-19 in routine clinical practice using CT images: results of 10 convolutional neural networks. Comput Biol Med. 2020;121:103795. https://doi.org/10.1016/j.compbiomed.2020.103795.
50. Singh D, Kumar V, Vaishali KM. Classification of COVID-19 patients from chest CT images using multi-objective differential evolution–based convolutional neural networks. Eur J Clin Microbiol Infect Dis. 2020;39:1379–89. https://doi.org/10.1007/s10096-020-03901-z.
51. Sharma S. Drawing insights from COVID-19-infected patients using CT scan images and machine learning techniques: a study on 200 patients. Environ Sci Pollut Res Int. 2020. https://doi.org/10.1007/s11356-020-10133-3.
52. Sedik A, Iliyasu AM, Abd El-Rahiem B, Abdel Samea ME, Abdel-Raheem A, Hammad M, et al. Deploying machine and deep learning models for efficient data-augmented detection of COVID-19 infections. Viruses. 2020;12:E769. https://doi.org/10.3390/v12070769.
53. Yang S, Jiang L, Cao Z, Wang L, Cao J, Feng R, et al. Deep learning for detecting corona virus disease 2019 (COVID-19) on high-resolution computed tomography: a pilot study. Ann Transl Med. 2020;8:450 https://doi.org/10.21037/atm.2020.03.132.
54. Huang L, Han R, Ai T, Yu P, Kang H, Tao Q, et al. Serial quantitative chest CT assessment of COVID-19: deep-learning approach. Radiol Cardiothorac Imaging. 2020;2:e200075. https://doi.org/10.1148/ryct.2020200075.

Chapter 13
Meditation

Koshin Mihashi, Hiroyuki Sakamoto, and Hiroki Takada

Abstract It is important for us to cope with stress in modern society. Research over the past two decades broadly supports the claim that mindfulness meditation practiced widely for the reduction of stress and health promotion exerts beneficial effects on physical/mental health and cognitive performance. In this chapter, we introduce the novel principle of "Anjodaza-Ho" which was originally proposed as a method for meditation to sustain stable sitting by Tempu Nakamura in 1919 in Japan. In fact, this method of meditation is owed to ancient Yoga training in India. Physical activity has been observed during this meditation. It has been shown that there are remarkable changes in the brain activity and the autonomic nervous system compared to the control group. We also discuss the perspective of the new meditation method using auditory stimulus.

Keywords Meditation with Anjo-daza Ho · Reduction of stress and promotion of health · Autonomic nervous system · Heart rate variability (HRV) · Brain activity Cerebral blood flow (CBF) · Conscious attention

K. Mihashi (✉)
Graduate School of Mathematics, Nagoya University, Nagoya, Japan
e-mail: k-mihashi@ic-net.or.jp

H. Sakamoto
Computer Dynamics Corporation, Tokyo, Japan

H. Takada
Graduate School of Engineering, University of Fukui, Fukui, Japan
e-mail: takada@u-fukui.ac.jp

H. Takada, K. Yokoyama (eds.), *Bio-information for Hygiene*, Current Topics in Environmental Health and Preventive Medicine,
https://doi.org/10.1007/978-981-15-2160-7_13

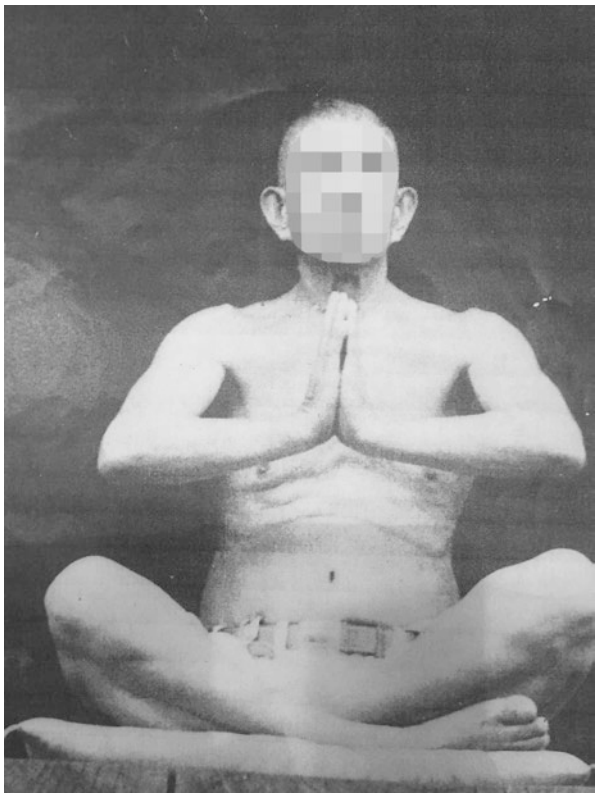

Fig. 13.1 Stable sitting sustained in conformity with the Anjo-Daza-Ho

13.1 Introduction

In this decade, mindfulness in the Western country is also learned during the meditation of daily life. Consciousness is a function of the mind, which might be measured as a brain activity, especially on our cerebral cortex. Because the cerebral cortex has been acquired in the process of evolution on the earth. Human beings can only conduct the mindful attention which makes us be able to look at our mind both from the inside and the outside.

Anjo-daza Ho [1] has been found and originated by Dr. Tempu NAKAMURA 1919 in JAPAN [2], which is often described as Anjo-daza way in this chapter. Stable sitting can be sustained in conformity with the Anjo-daza way (Fig. 13.1). One of the basic forms of meditation is "concentration meditation," in which sustained attention is focused on the sound of a Buzzer. Two techniques as follows are required to conduct this meditation; (1) the first technique is called "TOTAL-BREATH," which is known as a special way to control our respirations. Also, this technique has been derived from Kendo which is one of the traditional Japanese cultures of martial arts. (2) The second technique is called "KHUMVACCA" [3], which is a method to control the constant activity of rectus abdominis and/or external anal sphincter muscles and incorporates yoga technique. Skilled persons have

been instructed to strain the abdomen by relaxing their shoulders. It is said that this technique also affects the activities of lumbar muscles and the diaphragm. In this connection, biofeedback training has been focused on the constipation and the fecal incontinence [4]. Two-channel EMG provides a visual display of electrical activity of rectus abdominis and external anal sphincter muscles simultaneously [5]. This Anjo-daza-Way in the present study is composed of the following procedure:

Procedure of "ANJO-DAZA" Ho

1. Straighten your back and close your eyes.
2. You wait listening.
3. <Buzzer : ON> You listen to the sound carefully, for a while.
4. <Buzzer : OFF> You listen "Soundless-Sound with your mental-ear."
5. Put your mind out of the Space. And do not mind your senses.
6. Keep your mind still and clearer in the Soundless world.
7. <at intervals, Buzzer. ON> Keep your mind still and clearer in the soundless world.
8. === repeat several times ===

At the end, Clap your Hands and Awake!

In the beginning, sounds are accompanied by time fluctuation. Instead of focusing on the space with their eyes open, they are made devote themselves to hearing sounds, that is, finding the flow of time, which is corresponding to their following experience; Many skilled people said that they would feel the passage of time seems to be short only if their meditation were deepened in accordance with the Anjo-daza-ho. The space as visual information distracts their attention because the visual information occupies most of the processing in the brain.

The interval at which the buzzer sounds have been set randomly because it is necessary to attain a perfect serenity of mind in order to concentrate relentlessly during the meditation. However, the buzzer was set to sound at a certain interval (see Table 13.1) due to the analysis of the time series data (arithmetic mean). Also, a skilled person in the Anjo-daza way is able to focus his attention and deepen his meditation in accordance with this experimental protocol. Targets of bio-measurement in this chapter are for activities in the autonomic nerve system [6, 7]

Table 13.1 Experimental protocol

With eyes closed	Sound load	Rest (Remarks)	Accumulate time
	–	90 s (Pre, Term 1)	90 s
0 Beep	30 s	60 s (Term 2)	180 s
1 Beep	15 s	75 s (Term 3)	270 s
2 Beep	15 s	75 s (Term 4)	360 s
3 Beep	15 s	75 s (Term 5)	450 s
4 Beep	15 s	75 s (Term 6)	540 s
5 Gong	15 s	75 s (Term 7)	630 s
6 Beep	15 s	75 s (Term 8)	720 s
7 Hand clap	15 s	75 s (Term 9)	810 s

and the cerebral blood flow (CBF), especially on the frontal lobe [8]. According to the psychological experiments, there were evidences that self-control works on the prefrontal cortex [9, 10]. Construction of the prefrontal cortex is also argued, which is not one unified blob of gray matter, i.e., it has three key regions that divvy up of I will, I will not, and I want. One region, near the upper left side of the prefrontal cortex, specializes in "I will" power [11]. There were several case studies involved in the medical fields as in [12].

It is obvious that the system of the self-control in the prefrontal cortex relates to the autonomic nervous system, which is enhanced by the exercise [13] and the meditation in the Western style [14]. It has been reported that regular meditators have more gray matter in the prefrontal cortex, as well as region of the brain support self-awareness [9, 14].

Science is discovering that self-control is a matter of physiology, not just psychology. It is a temporary state of both mind and body that gives us the strength and calm to override our impulses. In particular, meditation enhances the parasympathetic nerve activity because of the respiration control. It has been shown that the meditation increases the heart rate variability (HRV) [15]. Studies also show that people with higher HRV are better at ignoring distraction, delaying gratification, and dealing with stressful situations [7]. These findings have led psychologists to call HRV the body's "reserve" of willpower [9], a physiological measure of our capacity for self-control. Methods including recording and the analysis are stated in the following section.

13.2 Autonomic Nervous System during Meditation

In this section, we focus on the activity in the autonomic nervous system, which is composed of sympathetic nerve and parasympathetic nerve. The activity of the later is known to be affected by the respiration.

Based on the biological rhythm, analysis of the neural function to control cardiovascular system has recently attracted attention as a new approach to the pathophysiology of cardiovascular diseases such as coronary artery disease, cardiac insufficiency, arrhythmia, and hypertension [16, 17]. A time-series analysis of the HRV is a typical example. According to the noninvasive evaluation of cardiac parasympathetic nerve function, it has been shown that parasympathetic dysfunction is a remarkable risk factor for coronary artery disease and sudden death [18–20]. The principle of the evaluation method for the autonomic nervous function is based on the fact that the sympathetic and the parasympathetic functions are reflected in the HRV in the following specific frequency bands, respectively [21–23]. There are peaks in the low-frequency band (0.04–0.14 Hz) and high-frequency band (0.15–0.40 Hz) in the power spectrum of the HRV, which are the LF component and the HF component, respectively. The latter is corresponding to the respiratory band. Now, this kind of time-frequency analysis and the advanced analytical algorithms are used as the demand for applying the analysis of the HRV to the study of

activities on the autonomic nervous system under various mental stresses or relaxes [23–25]. In this connection, both the sympathetic nerve and the parasympathetic nerve activity are reflected in the LF component, however, the ratio of the amplitude of the LF component to the HF component (LF/HF) has been proposed as a level of sympathetic nerve activity [21].

Four healthy volunteers participated in this study, who are composed of three skilled persons (40,55,60 years) and one non-skilled person (27 years). Before the measurement in this section, the aim of this study and the experimental protocol (see Table 13.1) were explained to all the subjects. The subject consented to participate in this experiment which can be stopped at any time in accordance with the subjects' will.

Electrocardiograms (ECGs) were recorded during the following experimental protocol (Table 13.1). The time required for this experiment is 900 s (15 min). Using WEB 10000 (Nihon Koden, Tokyo), the ECGs were measured with sampling frequency 1 kHz. R-R intervals were extracted from the ECGs during the meditation in order to analyze their HRV. Figure 13.2 shows time course of the R-R intervals for each subject. Findings in the ECGs were included as follows:

1. Periodic HRV could be seen in the ECGs of the skilled person (55 M) at regular intervals (Fig. 13.2a) while they were in the meditation called Anjo-Daza. We could not see this kind of anomalous ECGs during sleep/waking state. This HRV might be generated by the particular cardiovascular system during the meditation.
2. Stable HRV could be seen in the ECGs of the skilled person (60F) at almost constant intervals (Fig. 13.2b). In that case, the parasympathetic nervous activity might be dominant, and/or the HRV seemed as mild as during sleep.
3. Irregular variations in Fig. 13.2c constructs 1/*f*-distribution in the power spectrum, which is often found in the ECG of a healthy person during awakening.

13.3 Brain Activity During Meditation

Functional near-infrared spectroscopy (fNIRS) is a noninvasive optical imaging technique that measures changes in hemoglobin (Hb) concentrations within the brain by means of the characteristic absorption spectra of Hb in the near-infrared range [26–28]. This technique has been applied to various scientific fields [29–31]. We have herein measured the brain activity during the mindfulness meditation and succeeded in findings of the changes in the brain activity during the mindfulness meditation.

The brain activity, especially on the cerebral cortex, is taken attention in this section because the cerebral cortex was acquired by human beings as primates during the process of evolution, and is most likely to be related to consciousness [9, 11] and its function, the mind. Variations of the concentrations in oxyhemoglobin (oxyHb), deoxyhemoglobin (deoxyHb), and these summations, total Hb, on the frontal, the left temporal, the right temporal, and the occipital lobe (Fig. 13.3a) were measured

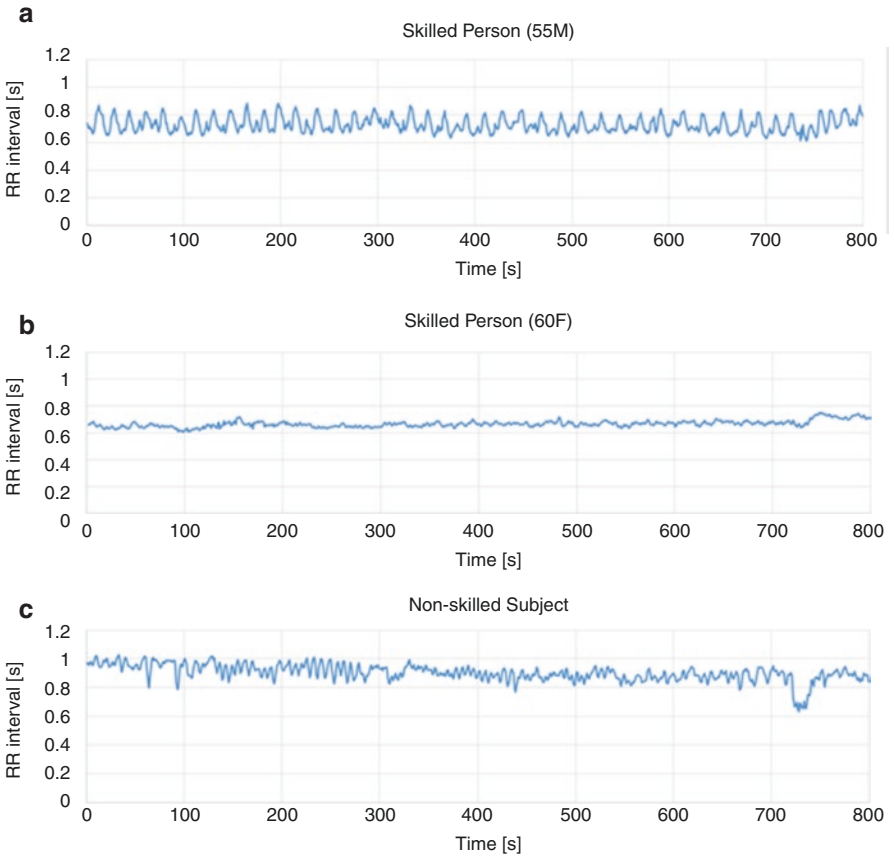

Fig. 13.2 Time series data of the R-R intervals. R-R intervals were extracted from the ECGs of a skilled man (55 years old) (**a**), a skilled woman (60 years old) (**b**), and a non-skilled man (27 years old) (**c**)

by using fNIRS LABNIRS (Shimazu, Kyoto). The measured data was standardized for each term based on Term 1. Using the standardized data, the integrated values of the CBF were calculated for each component, oxyHb, deoxyHB, and total HB in each term. Especially on the frontal lobe, a significant increase of the oxyHB was observed in red boxes (Fig. 13.3b) of the skilled persons ($p < 0.05$) whereas no remarkable changes were obtained from the non-skilled persons (Fig. 13.3c).

Neurovascular coupling (NVC) refers to the relationship between local neural activity and subsequent changes in the CBF [32]. Tight temporal and amplitudinal linkage between neuronal activity and CBF delivery has been observed for over 120 years [33–35]. The magnitude and spatial location of blood flow changes are tightly linked to changes in neural activity through a complex sequence of coordinated events involving neurons, glia, and vascular cells. According to the previous studies [36–38], the regional blood flow is likely controlled by multiple

mechanisms such as the feedforward involving neural signaling via neurotransmitters, and the function to mediate neurovascular coupling, in addition to the feedback mechanisms that are sensitive to variations in the concentration of ionic and molecular metabolic by-products. The last one is known to be as a classical description that energy supply is controlled by the energy demand. Many vascular-based functional brain imaging techniques, such as fNIRS and fMRI, rely on this coupling to infer changes in neural activity.

In this section, a remarkable increase of the CBF was observed in the skilled person. Especially on the frontal lobe, this is a clear phenomenon from the early term compared to the Pre-rest (Term 1). As shown in Fig. 13.4, the number of the probe-channel at which remarkable increase was also obtained in the CBF on the cerebral cortex for the skilled person (in blue) and the non-skilled person (in red). The channel at which remarkable increase was distributed around the frontal lobe. If we assumed the NVC, the brain activity in the frontal lobe would be enhanced during the meditation. It is suggested that neurons in the consciousness are distributed mainly on the cerebral cortex of the frontal lobe, which is a hot topic in this field [9, 39, 40]. Perhaps the form of consciousness is beginning to appear. It does not mean that there is no appearance in the no skilled person, but it also appears in the no skilled person along with the passing of the time.

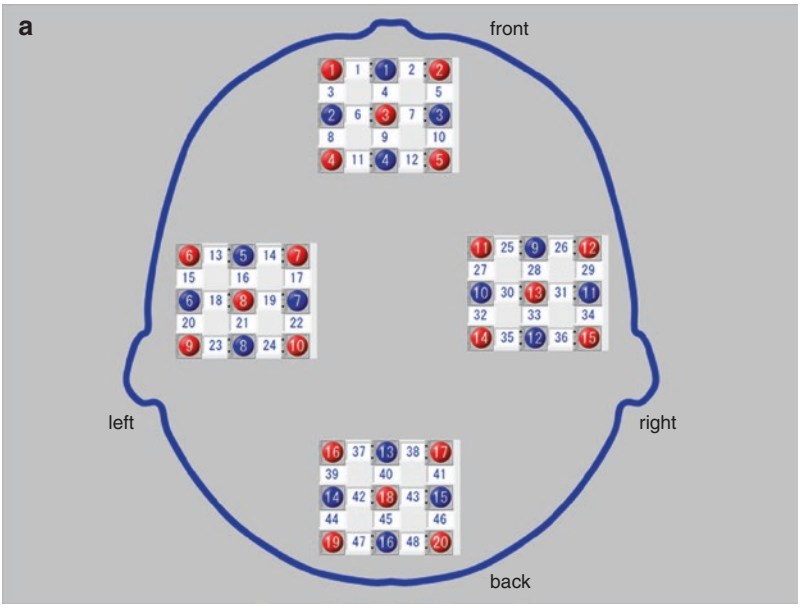

Fig. 13.3 Probe-arrangement and a typical result for the fNIRS measurement. Probe-arrangement for the measurement in the Sect. 13.3 (**a**) the probe-arrangement at which remarkable increase was obtained in the brain blood flow on cerebral cortex for the skilled person (**b**) and the non-Skilled person (**c**) in Term 3

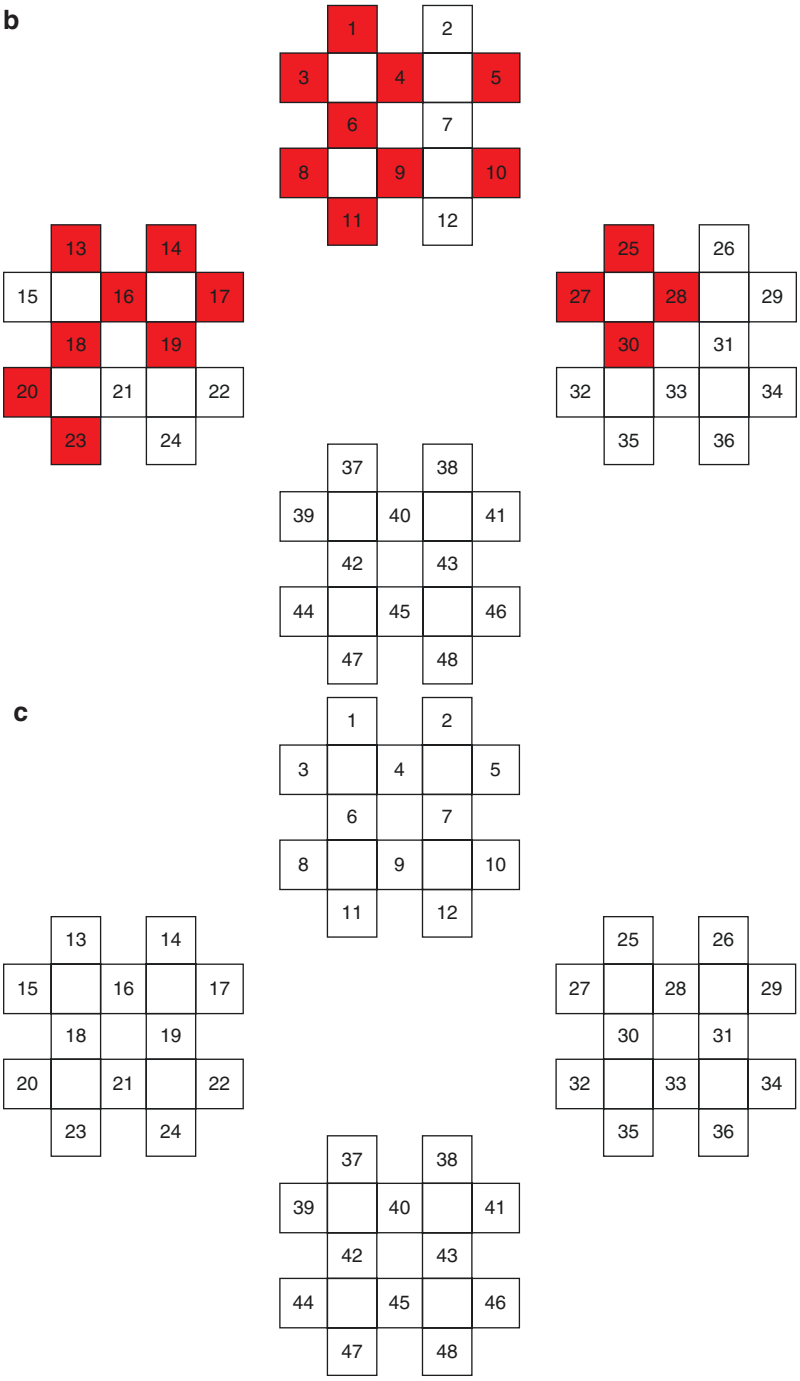

Fig. 13.3 (continued)

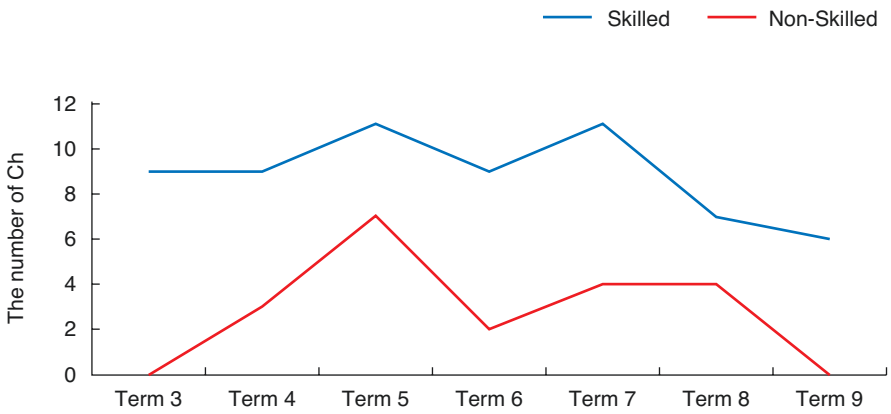

Fig. 13.4 The number of the probe-channel at which remarkable increase was obtained in the brain blood flow on cerebral cortex for the skilled person (in blue) and the non-Skilled person (in red) in the darkroom

13.4 Perspective of New Meditation Method Using Auditory Stimulous

Figures 13.2 shows R-R intervals in minute plotted. We can find that the skilled person has stable of his heart rate variability at regular intervals (Fig. 13.2a). In addition, the second case of a skilled person shows she looks like sleeping during the meditation (Fig. 13.2b). On the other hand, typical HRV during the arousal can be seen in Fig. 13.2c, which was obtained from the non-skilled person. Amplitude of the variations in the R-R intervals were tended to be larger than those of the skilled person (Fig. 13.2). Moreover, spectral analysis of these R-R intervals has been also conducted. As a result, peaks in both frequency bands, i.e., LF (0.04–0.15 Hz) and HF (0.15–0.40 Hz) were simultaneously observed in the skilled persons, which was seldom seen in the non-skilled persons during the arousal/sleep.

Regarding the result of fNIRS, in terms of the CBF, the increase of the oxyHb was observed in the skilled person, especially on the frontal lobe (Fig. 13.3b), which might be caused by the particular breathing method, TOTAL-BREATH. This is a clear phenomenon from the early term. Assuming the NVC, we could observe the increase of the CBF on the frontal lobe during the meditation introduced in this chapter. The brain activity on the frontal lobe is enhanced by the conscious attention, which is induced by the "SINSINTOITSU-Do," new autoregressive model of the meditation (Fig. 13.5); what makes oneself is oneself. Oneself is composed of three elements: brain, mind, and body in particular. In adolescents, problem behaviors are occasionally found because the mind and the body usually develop separately. Coherence between the mind and the body is required to evolve the brain promoting conscious attention. The coherence between the body and the mind does not combine plasticity. Beginners cannot perform the

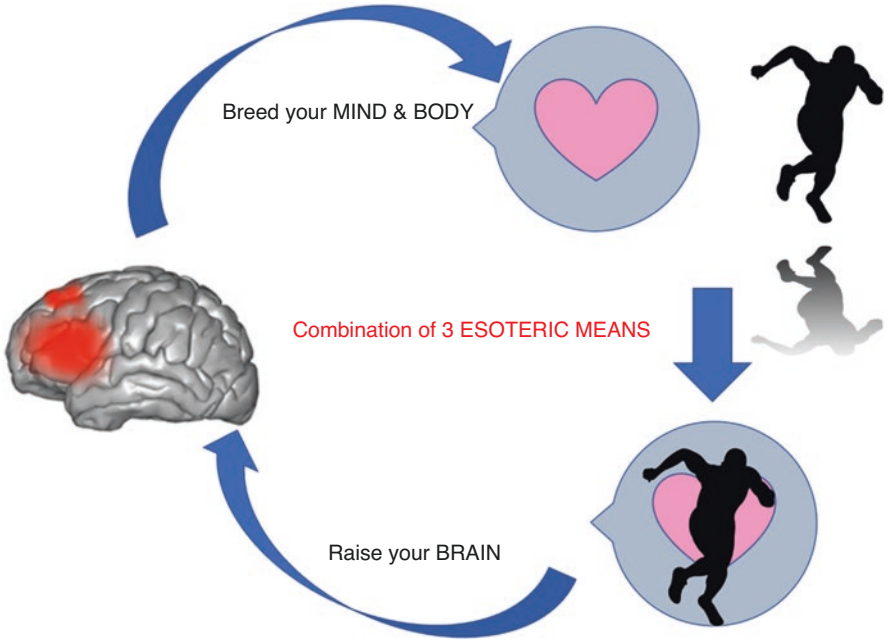

Fig. 13.5 Composition of new mindfulness meditation: SIN-SIN-TOHITSU-DO. The recurrence system is composed of three esoteric means: ANJO-DAZA-HO, TOTAL-BREATH, and KHUMVACCA

coherence. Dr. Tempu suggested that at first, you should concentrate on the auditory system to listen the sound without noticing your environment. Secondly, you listen "Soundless-Sound with your mental-ear. Lastly, put your mind out of the space and do not mind your senses (Appendix). Gratitude constitutes belief, which supports oneself. The meditation directly contributes to what the mind and the body cohere.

<Motto>.

- *-Be not in anger, nor in fear nor in grief.*
- *-Live preciously your life of the very present moment,*

In honest and kindness and with cheerfulness.

Brain Scientists often discuss about the physicality to understand the intelligence. There is no strategy without some exception as in this case to understand the mind. In this chapter, bioinformation during the meditation was obtained from the point of view, which was based on two axes: degree of voluntary/involuntary and that of arousal. Based on this frame, we can pursuit what is consciousness and mind, which is regarded as a function of the consciousness. For instance, both degrees are considered to be high during the meditation. Therefore, our state during the meditation is completely different from that during the sleep. However, suggesting oneself before the sleep, it is easy to interact with our involuntary attention.

"SINSINTOITSU-Do" to perform the coherence has been proposed, which is composed of the following three; "TOTAL-BREATH," "KHUMVACCA," and "ANJODAZA-Ho." These are interrelated with each other.

13.5 Conclusion

Dr. Tempu described in his TEXT "MAXIM" as follows:

1. As the ANJODAZA-Ho is the absolute and esoteric means to draw a right consideration, you must make efforts to practice it for such a purpose, on every occasion.
2. To be a "Real Man," it is necessary to practice good cleansing of his mind incessantly. It is because the mind is the basis for the actual realization of his whole life.

Appendix Foreword To: Dr. Tempu's Book

Everyone living today in the turmoil, strife, and worldwide tension requires an anchor to one's thoughts.

If for no other reason but that we hold to spiritual and lasting values as an avenue by which to explore the future and forget the past, and with full confidence that if we adhere to these basic values, rewards will come to us commensurate with our effort.

Dr. Tempu has outlined to us this Pathway. It is one of spirituality, truth, honesty, and integrity.

If, we but follow this philosophy of living, one cannot help but go forward to the rewards of achievement, success, and contentment.

David E, Beatty

References

1. Tempu Society. ANJO-DAZA. 2002; The registered trademark symbol 4497028.
2. Mihashi K. Discussion on brain activity during meditation. In: Proceedings of IEEE ICCSE 2016 (Satellite lecture in University of Fukui). 2016; p. 31.
3. Tempu Society. KHUMVACCA. 2002; The registered trademark symbol 4621260.
4. Lee HJ, Jung KW, Myung SJ. Technique of functional and motility test: how to perform biofeedback for constipation and fecal incontinence. J Neurogastroenterol Motil. 2013;19(4):532–7. https://doi.org/10.5056/jnm.2013.19.4.532.
5. Heymen S, Scarlett Y, Jones K, Ringel Y, Drossman D, Whitehead WE. Randomized, controlled trial shows biofeedback to be superior to alternative treatments for patients with pelvic floor dyssynergia-type constipation. Dis Colon Rectum. 2007;50:428–41.

6. Tang YY, Ma Y, Fan Y, Feng H, Wang J, Feng S, Lu Q, Hu B, Lin Y, Li J, Zhang Y, Wang Y, Zhou L, Fan M. Central and autonomic nervous system interaction is altered by short-term meditation. Proc Natl Acad Sci. 2009;106:8865–70. https://doi.org/10.1073/pnas.0904031106.
7. Peressutti C, Gonzalez JMM, Manso JMG, Mesa D. Heart rate dynamics in different levels of Zen meditation. Int J Cardio. 2010;145:142–6.
8. Barbara T, Campanella F, Fabbro F. Medial orbital gyrus modulation during spatial perspective changes: pre-vs. post-8weeks mindful-ness meditation. Cons Cog. 2016;40:147–58.
9. McGonigal K. The willpower instinct. New York: Penguin Group; 2012. p. 12–8.
10. Sapolsky RM. The frontal cortex and the criminal justice system. Philos Trans R Soc Ser B 2004;359:1787–96.
11. Suchy Y. Executive functioning: overview, assessment, and research issues for non-neuropsychologists. Ann Behav Med. 2009;37:106–16.
12. Anson JA, Kuhlman DT. Post-ictal Klüver-Bucy syndrome after temporal lobectomy. J Neurol Neurosurg Psychiatry. 1993;56(3):311–3.
13. Oaten M, Cheng K. Longitudinal gains in self-regulation from regular physical exercise. Br J Health Psychol. 2006;11:717–33.
14. Pagnoni G, Cekic M. Age effects on gray matter volume and attentional performance in Zen meditation. Neurobiol Aging. 2007;28:1623–7.
15. Thayer JF, Hansen AL, Rose ES, Johnsen BH. Heart rate variability, prefrontal neural function, and cognitive performance: the neurovascular integration perspective on self-regulation, adaptation, and health. Ann Behav Med. 2009;37:141–53.
16. Malliani A, Pagani M, Lombardi F, Cerutti S. Cardiovascular neural regulation explored in the frequency domain. Circulation. 1991;84:482492.
17. Appel ML, Berger RD, Saul JP, Smith JM, Cohen RJ. Beat to beat variability in cardiovascular variables:noise or music? J Am Coil Cardiol. 1989;14:1139–48.
18. Martin GJ, Magid NM, Myers G, Barnett PS, Schaad JW, Weiss JS, Lesch M, Singer DH. Heart rate variability and sudden death secondary to coronary artery disease during ambulatory electrocardiographic monitoring. Am J Cardiol. 1987;60:86–9.
19. Myers GA, Martin GJ, Magid NM, Barnett PS, Schaad JW, Weiss JS, Lesch M, Singer DH. Power spectral analysis of heart rate variability in sudden cardiac death: comparison to other methods. IEEE Trans Biomed Eng. 1986;33:1149–56.
20. Kleiger RE, Miller JP, Bigger JT Jr, Moss AJ. Decreased heart rate variability and its association with increased mortality after acute myocardial infarction. Am J Cardiol. 1987;59:256–62.
21. Pagani M, Lombardi F, Guzzetti S, Rimoldi O, Furlan R, Pizzinelli P, Sandrone G, Malfatto G, Dell'Orto S, Piccaluga E, Turiel M, Baselli G, Cerutti S, Malliani A. Power spectral analysis of heart rate and arterial pressure variabilities as a marker of sympatho-vagal interaction in man and conscious dog. Circ Res. 1986;59:178–93.
22. Pomeranz B, Macaulay RJB, Caudill MA, Kutz I, Adam D, Gordon D, Kilborn KM, Barger AC, Shannon DC, Cohen RJ, Benson H. Assessment of autonomic function in humans by heart rate spectral analysis. Am J Phys. 1985;248:H151–3.
23. Hayano J, Sakakibara Y, Yamada A, Yamada M, Mukai S, Fujinami T, Yokoyama K, Watanabe Y, Takata K. Accuracy of assessment of cardiac vagal tone by heart rate variability in normal subjects. Am J Cardiol. 1991;67:199–204.
24. Hayano J, Taylor JA, Yamada A, Mukai S, Honi R, Asakawa T, Yokoyama K, Watanabe Y, Takata K, Fujinami T: Continuous assessment of hemodynamic control by complex demodulation of cardiovascular variability. Am J Physiol. 1993 (in press).
25. Bloomfield P. Complex demodulation, Fourier analysis of time series: an introduction. New York: Wiley; 1976. p. 118–50.
26. Cooper RJ, Boas DA. Functional near-infrared spectroscopy. Brain Map. 2015;1:143–8.
27. Domenico SID, Rodrigo AH, Dong M, Fournier MA, Ayaz H, Ryan RM, Ruocco AC. Functional near-infrared spectroscopy: proof of concept for its Application in social neuroscience. In: Neuroergonomics. 2019; p. 167–73.

28. HasanAyaz H, Izzetoglu M, Izzetoglu K, Onaral B. The use of functional near-infrared spectroscopy in neuroergonomics. In: Neuroergonomics. 2019; p. 17–25.
29. Dehais F, Ayaz H, Gateau T. Assessing working memory load in real flight condition with wireless fNIRS. In: Neuroergonomics. 2018; p. 213–4.
30. Sangan S, Lamontagne A, Fung J. Cortical mechanisms underlying sensorimotor enhancement promoted by walking with haptic inputs in a virtual environment. Prog Brain Res. 2015;218:313–30. https://doi.org/10.1016/bs.pbr.2014.12.003.
31. Gursky ZH, Klintsova AY. Frontal lobe dysfunction after developmental alcohol exposure. In: Addictive substances and neurological disease. 2017; p. 139–47.
32. Phillips AA, Chan FHN, Zheng MMZ, Krassioukov AV, Ainslie PN. Neurovascular coupling in humans: physiology, methodological advances and clinical implications. J Cerebral Blood Flow Metabol. 2016;36(4):647–64.
33. Donders FC. Die Bewegungen des Gehirns und die Vera¨ Nderungen der Gefa¨ ssfu¨ llung der Pia mater. Schmid's Fahrbucher. 1851;69:16–20.
34. Mosso A. Sulla circolazione del cervello dell'uomo. Atti R Accad Lincei. 1880;5:237–358.
35. Roy CS, Sherrington CS. On the regulation of the blood-supply of the brain. J Physiol. 1890;11:85–158.
36. Attwell D, Iadecola C. The neural basis of functional brain imaging signals. Trends Neurosci. 2002;25:621–5.
37. Lauritzen M. Reading vascular changes in brain imaging: is dendritic calcium the key? Nat Rev. 2005;6:77–85.
38. Uludag K, Dubowitz DJ, Yoder EJ, Restom K, Liu TT, Buxton RB. Coupling of cerebral blood flow and oxygen consumption during physiological activation and deactivation measured with fMRI. Neuroimaging. 2004;23:148–55.
39. Crick F, Koch C. A framework for consciousness. Nat Neurosci. 2003;6:119–26.
40. Andrea R. The mind at night. New York: Basic Books; 2005.